A calorimetric study of hydrogen storage on graphene functionalized with Titanium

Tesi di laurea magistrale

Luca Basta

Università di Pisa

Giugno 2017

Contents

Introduction

This thesis reports the research work on the calorimetric detection and analysis of hydrogen adsorption on titanium-decorated graphene. The entire investigation has been realized at the facilities of Laboratorio NEST. The sample preparation has been done in clean and controlled conditions (cleanroom), and the measurements have been performed in an Ultra-High Vacuum environment (UHV chamber of a RHK Technology Scanning Tunneling Microscope).

This study is inserted in a wider research context on hydrogen storage systems. In fact, because of the variety of environmental problems in burning fossil fuels (coal, oil, and gas) as the massive release of carbon dioxide or the contribution in acid rain and air pollution [1], the research of new sustainable alternative energies has been very active recently. However, while solar and wind energy production are mature technologies already developed, the problem of energy storage is still unsolved.

In this direction one of the most promising energy carriers is hydrogen, which, once produced, can be stored for a long period. When energy is requested, the same amount of energy that has been provided for its production will be released during its use in fuel cells. Actually, the major drawback in the use of hydrogen as energy carrier is the lack of efficient storage systems.

For that reason, solid-state graphene-based devices are extensively investigated for their application in the hydrogen storage field. In particular, functionalized mono-layer graphene has shown interesting properties such as stable hydrogen storage, fast adsorption and desorption, desorption energies in a range useful for practical application, and in perspective high storage density.

In this thesis work an original thermometric technique to monitor hydrogen storage has been utilized. We focus on the functionalization of mono-layer graphene with titanium, which is a widely investigated system and can be used as a reference material. The first direct detection of the exothermic adsorption of molecular

hydrogen on Ti-decorated graphene at room temperature is presented. Then, the calorimetric analysis and the enthalpy release calculation are discussed, and future improvements and applications are presented.

A summary description of the thesis chapters is briefly listed below:

- in Chapter 1 we present the state of the art of the current research. The motivation of this research and the results on hydrogen storage systems from literature, with focus on solid-state and graphene-based systems, are presented;
- in Chapter 2 we discuss the idea of the experiment. The sample used in the measurement and the procedure for the calorimetric detection are described;
- in Chapter 3 we describe the experimental setup and the measuring principles utilized for the measurements;
- in Chapter 4 we present the sample preparation and calibration. These procedures are fundamental in order to be able to operate with the prepared sample and subsequently derive a quantitative analysis;
- in Chapter 5 we list the experimental results obtained in the measurements. The initial blank measurement is performed as control measurement and subsequently the calorimetric detection is presented;
- in Chapter 6 we present the signal analysis and the calculation of the heat release. Finally an outlook of future improvements is discussed.

State Of The Art 1

1.1 Hydrogen storage systems

Hydrogen is currently considered one of the most promising clean fuels, because of the fact that the product of its combustion is only water. Furthermore, it can store a large amount of energy: on a mass basis, hydrogen has nearly three times the energy content of gasoline (120 MJ/kg for hydrogen versus 44 MJ/kg for gasoline).

Hydrogen is the most common element in universe and the third one on earth. It should be borne in mind, however, that molecular hydrogen is not directly available on earth (it is commonly bound to oxygen or other elements) and, hence, it cannot be used as a primary energy source. Referring to hydrogen as a fuel in the same sense as we refer to petrol or natural gas is misleading. In fact hydrogen must be produced (e.g. from the electrolysis of water), and the same amount of energy used for its production is subsequently obtained during its use in fuel cells. The noteworthy advantage in the perspective of the use of hydrogen instead of other energy carriers, such as electricity, is that once the energy is chemically stored, for example in hydrogen, then it can be infinitely retained and easily transported, thus solving the problem of energy dispersion.

In order to briefly present the several means of hydrogen storage considered in the last years it is important to recall that to measure the efficiency of storage, two parameters are fundamental: the *gravimetric density* (GD), that is the weight percentage of stored hydrogen to the total weight of the system (hydrogen + container), and the *volumetric density* (VD), the stored hydrogen mass per unit volume of the system. The goal is to pack hydrogen as close as possible, in other words to reach the highest volumetric density by using as little additional material as possible. Specific targets from the US Department of Energy (DOE, by 2020) [2] for on-board hydrogen storage systems for light-duty vehicles include the following:

- 1.8 kWh/kg system (5.5 wt.% of hydrogen)

- 1.3 kWh/L system (40 kg of hydrogen per m^3)
- \$10/kWh (\$333 per kg of stored hydrogen)

The problem of finding an efficient and safe hydrogen storage system is still unsolved. The most common storage system is high pressure gas cylinders, which operate at pressures from 30 to 70 MPa, so that hydrogen can reach a VD of 36 kg/m^3 and a GD of 6wt% [3, 4]. The main concern about this means of storage is the safety of pressurized cylinders, especially in highly populated regions. Moreover, according to the *Joule-Thomson effect* [5], hydrogen increases its kinetics energy when expanded to atmospheric pressure, introducing thermal gradients which could be dangerous in the presence of leaks. The relatively low hydrogen density together with the high gas pressure in the system are important drawbacks of this technically simple and mature storage method.

Another storage possibility are cryogenic tanks at 21.2 K at ambient pressure, leading to a VD of 70 kg/m^3 and a GD dependent on the size of the container (between 3 and 10 wt%) [3, 6]. The major disadvantage of this system is the boil-off rate of hydrogen from a liquid storage vessel because of heat leaks, which is a function of its size, shape, and thermal insulation. Boil-off losses are typically around 0.2% per day. The large amount of energy necessary for liquefaction and the continuous boil-off of hydrogen limit the possible use of liquid hydrogen storage system to applications where the cost of hydrogen is not an issue and the gas is consumed in a short time.

1.2 Hydrogen storage in solid-state systems

Alternatively, hydrogen can be stored in solid absorbers by two different ways: incorporation into the crystal structure of the storage materials via chemical absorption of atomic hydrogen, as it is the case for complex metal hydrides, or by the chemisorption and the physisorption of (atomic or molecular) hydrogen on high surface area materials, such as metal-organic frameworks (MOFs) or carbon based materials. Notwithstanding the use of these solids is intrinsically safe and allows high volumetric capacity, the gravimetric capacity is limited by the weight of the retaining material, and the most interesting results, at present, are usually obtained under high pressure ($\sim$ MPa) or low temperature ($\sim$ 77 K) conditions [7, 8]. In order to work close to room temperature, the ideal range of binding energies for hydrogen on solid state materials is 0.20-0.60 eV. In this energy range the adsorption is stable enough to guarantee the safety and the stability of the hydrogen storage, and the temperature required for the desorption of the stored hydrogen is still close to room temperature.

1.2.1 Graphene as storage system

Recently, graphene attracted a lot of attention as a hydrogen storage material owing to its chemical stability, low weight, and favorable physical-chemical properties for adsorption. Graphene is a two-dimensional structure of carbon atoms arranged in a honeycomb geometry only one atom thick (see Fig.1.1(a)). The chemical properties of carbon allow the sp^2 hybridization of the atomic orbitals (see Fig.1.1(b)) that presents three strong in-plane (σ) bonds per atom, forming the hexagonal structure of graphene, found to be the strongest material in nature [9].

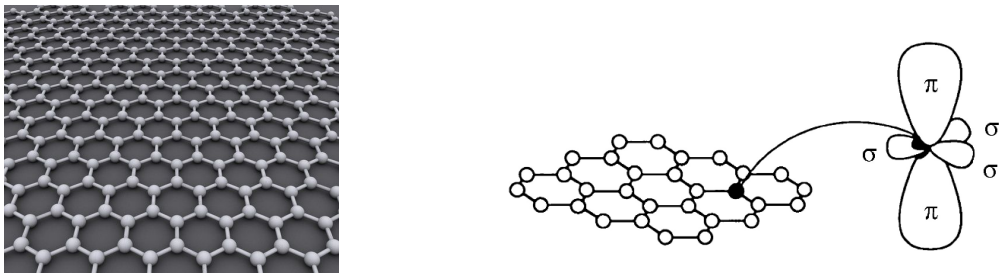

(a) (b)

Figure 1.1: (a) Honeycomb structure of graphene. (b) Carbon atomic orbitals σ and π in the sp^2 hybridization.

Moreover, the presence of the p_z orbitals (π orbitals), not completely filled and perpendicular to the hexagon plane, and the linear k dependence of the π and π^* bands close to the K and K' points (see Fig. 1.2) are responsible for the excellent electron conduction of graphene [10].

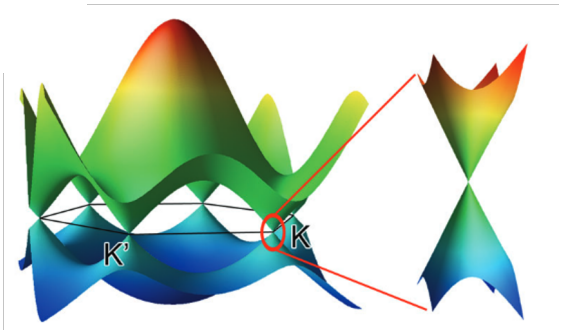

Figure 1.2: Band structure of graphene, showing the linear dispersion around the K and K' points in reciprocal space [10].

Particularly relevant for hydrogen storage applications is the fact that graphene can be produced on a large scale by several techniques, either by "top-down" or

"bottom-up" procedures. The former approaches generally involve the exfoliation of graphite through chemical (solution-based exfoliation, graphite oxide exfoliation and reduction), electrochemical (oxidation/reduction or exfoliation) or simply mechanical (scotch tape) processes which weaken the van der Waals forces between the graphene layers in order to separate them. On the other hand, the bottom-up approaches generate graphene by assembling small molecular building blocks into single or few layer graphene structures by catalytic (chemical vapor deposition, CVD), thermal (SiC decomposition), or chemical (organic synthesis) processes [11].

Basically hydrogen can be adsorbed on graphene in two different ways: by *physisorption* or by *chemisorption*. Fluctuations in the charge distribution, which are called dispersive or van der Waals interactions, allow to a gas molecule to interact with several atoms at the surface of a solid and to be physisorbed onto the surface. Because of the nature of the process, physisorption usually occurs with hydrogen in molecular form, and the H_2 binding energy was theoretically evaluated in the range of $(0.01 - 0.1)$ eV [12, 13]. This spread of values can be explained by the fact that van der Waals dispersion forces are very difficult to represent. However it is clear that the bond between molecular hydrogen and graphene is weak and thus requires low temperatures or high pressure to ensure reasonable storage stability. It was shown that under the most favorable conditions, H_2 can form a compact monolayer on the graphene sheet, equivalent to a GD of 3.3 wt% [3], whereas the VD depends on the possibility of creating complex structures of graphene sheets.

On the other hand, in order to chemically bind hydrogen on graphene the dissociation of the H_2 molecule is required, and therefore chemisorption presents a high barrier, which is estimated around 1.5 eV [14]. Conversely atomic hydrogen tends to chemisorb at the graphene surface, with a binding energy of $\sim$0.8 eV, and an energy barrier of $\sim$0.3 eV, which can be lowered by modifying the curvature of the graphene sheet [15]. From theoretical studies it was shown in particular that the adsorption of the first H atom locally modifies the graphene structure facilitating further H binding, leading to a collective stabilization effect [16, 17]. The formation of dimers of H on the surface of graphene leads to a gain of almost 1.0 eV in energy compare to the isolated H bond [18]. As a result of this advantageous process, the maximum GD theoretically reachable in graphene by chemisorption would be 8.3 wt% (even higher than the DOE target). To reach this value, the formation of a completely saturated graphene sheet, called *graphane*, is required. This structure consists in the complete sp^3 hybridization of carbon bonds, with one H atom for each C atom, and its stability was investigated experimentally, and was found as the most stable of all the possible hydrogenations ratios of graphene [19]. Similarly to the physisorption, the VD depends on the possibility to building

compact structures with graphene (or graphane) sheets.

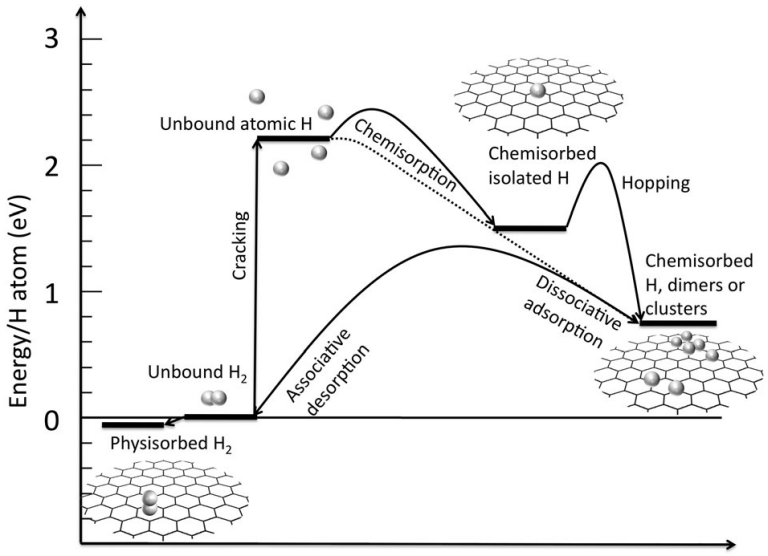

Figure 1.3: Diagram of the energy levels for the graphene-hydrogen system [8].

Fig.1.3 summarizes the energy profiles for the physisorption and the chemisorption processes. The reference level is *pristine* graphene (ideal flat graphene without any defects) plus unbound molecular hydrogen. The energy is in eV per H atom, so to obtain the values per H_2, each energy level and barrier value must be doubled [8].

Experimentally it was shown that a layered structure of graphene can be realized by using a sequence of graphene oxide layers connected by benzenediboronic acid pillars with an interlayer separation of 10 Å. This leads to a predicted GD of around 6 wt% at 77 K and a pressure of 1 bar [20]. The storage capacity at room temperature is far lower. In fact the best result using carbon nanotubes provide a GD of around 1 wt% at a pressure of 120 bar and at room temperature [21]. A similar value is achieved for hydrogen adsorption on graphene-like nano-sheets (highly agglomerated and disordered exfoliated graphene sheets) with a storage capacity of 1.2 wt% at 77 K and a pressure of 10 bar or 0.68 wt% at 77 K and ambient pressure [22].

1.2.2 Surface functionalization to enhance storage capacity

Even though it is possible to store hydrogen in graphene through either physisorption or chemisorption, in order to achieve large storage capacity that meets the DOE targets it is necessary to work under unpractical environmental conditions (high pressure or low temperature). An effective storage system on the contrary should work at room temperature. Therefore various approaches to improve hydrogen adsorption were theoretically proposed.

One possibility is to chemically decorate the graphene with alkali metal atoms such as Lithium, Sodium, or Potassium. For example, in the case of Li the process is achieved in two steps: initially, graphene is metalized through charge donation by adsorbed Li atoms to its π-bands (as shown in Fig.1.4(a)). Then the first adsorbed H_2 is bound to Li by weak van der Waals interactions, so its binding energy is generally small. Subsequently, a small amount of charge (~ 0.1 electrons) is transferred from the system Li+graphene to the nearest H atom of the adsorbed H_2 molecules. As a result, H atoms that receive charge from Li become negatively charged, and the covalent H_2 bond become polarized, so that further H_2 adsorption is possible. Therefore each positively charged Li ion can absorb up to four H_2 molecules (as shown in Fig.1.4(b)) equivalent to a GD around 10 wt% [23].

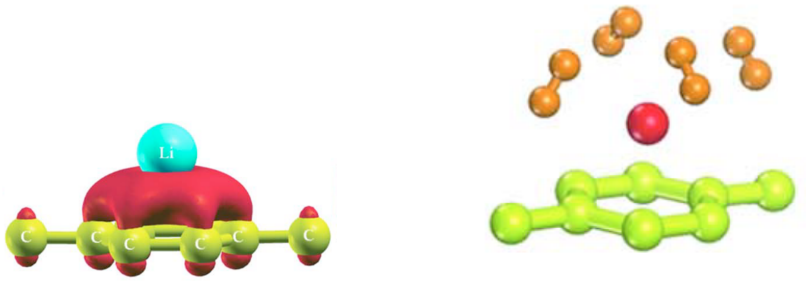

(a) (b)

Figure 1.4: (a) Positive charge accumulation for one Li atom adsorbed. (b) Adsorption of H_2 molecules by Li atoms [23].

Alternatively a different approach is based on the *Kubas* interaction [24] that permits the binding of hydrogen to the active metal sites adsorbed at the graphene surface. The *Kubas* interaction occurs between graphene decorated with transition metal atoms and hydrogen molecules, and results in an elongation of the $H-H$ bond without breaking. Electronically it requires the σ-donation from the filled $H-H$ σ-bonding orbital into a vacant d orbital of a metal and simultaneously the π-back-donation from a filled metal d orbital into the empty σ^* anti-bonding orbital of the H_2 molecule (as schematically shown in Fig.1.5).

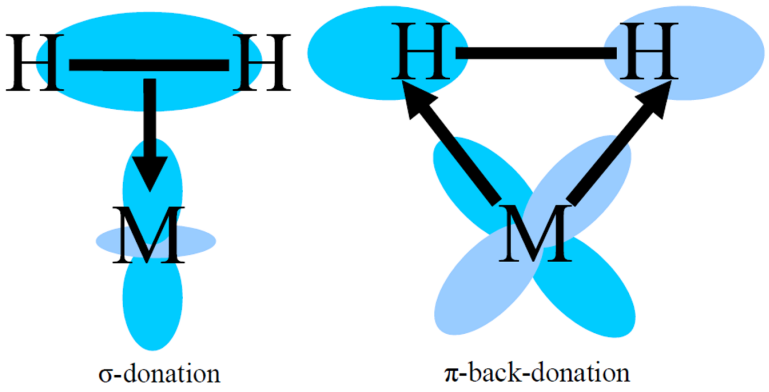

Figure 1.5: Diagram of the two synergic terms of the Kubas interaction.

The $H - H$ bond, ~ 0.89 Å in the Kubas interaction, is stretched by approximately 20% with respect to that in free H_2 (0.74 Å), confirming that hydrogen in neither physisorbed nor chemisorbed. The most studied are the early transition metals of the first row, in particular Scandium, Titanium, and Vanadium, due to the fewer d electrons and the lower weight (in order to minimize the GD of the storage system). The main advantage of storing hydrogen exploiting this interaction is that the binding energy is in the middle between the physisorption and the chemisorption ranges, obtaining optimal condition for room-temperature application.

Finally, it is possible to exploit the mechanism of hydrogen *spillover*, in which a metal atom adsorbed on the graphene surface catalyses the dissociation of the molecular hydrogen, and the H atoms then migrate, usually through diffusion, to bind with the graphene nearby. Experimentally it has been seen that decorating graphene with Palladium atoms provides an increase in the GD from 0.6 wt% to 2.5 wt% [25], at a pressure of 30 bar and room temperature. Fig. 1.6 shows the scheme of the dissociative mechanism trough Pd atoms and the subsequent diffusion of H atoms.

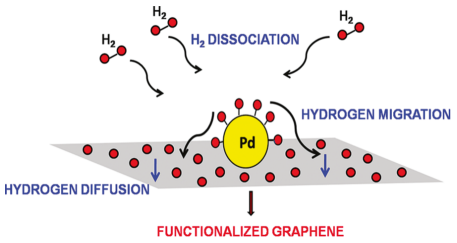

Figure 1.6: Spillover mechanism [25].

An important drawback is the clustering of transition metal atoms. In fact, because of the higher binding energy of the bonding $metal-metal$ with respect to the bonding $metal-graphene$, atoms tend to form small islands (*clusters*) that grow and become more dense as the coverage is increased [26]. The presence of these clusters results in a decrease in the GD owing to the reduction of the total metal surface that is available for binding hydrogen. Also in case of functionalization with alkali metals this problem remains, even if in a minor way [27, 28].

1.2.3 Ti-decorated graphene

In this thesis work we used Ti to functionalize the graphene surface, therefore in this section we summarize the theoretical and experimental state of the art on Ti-functionalized graphene.

To investigate hydrogen adsorption through the presence of Ti atoms, first-principles calculations within Density Functional Theory were performed [29, 30]. First of all, Ti atoms are firmly bonded on graphene as a result of the donation of part of Ti $4s$ and $3d_{z^2}$ electrons to the π band of graphene and the simultaneous back-donation of graphene π^* electrons to the Ti $3d_{xz}$ and $3d_{yz}$ orbitals. A binding energy of 1.27 eV [29] per single Ti atom was calculated (quite strong with respect to the thermal energy available at room temperature, 0.025 eV). Subsequently hydrogen molecules are adsorbed via Kubas interaction, that involves a σ electron transfer from H_2 to the d orbitals of Ti, and a Ti electron back-donation to the σ^* orbitals of hydrogen. Furthermore, the charge transfer from Ti to graphene generates a surface dipole that induces the polarization of the hydrogen molecule. The attractive interaction between the surface and the molecular hydrogen induced dipoles strengthens the hydrogen binding and allows the Ti atom to bind up to four H_2, with an average binding energy of 0.51 eV (as shown in Fig. 1.7 [30]) and a final GD of 7.8 wt% in case of two-side coverage. This value falls in the ideal range of energies, 0.20-0.60 eV.

In order to experimentally inquire into the properties of Ti-decorated graphene as hydrogen storage system, epitaxial, high-quality monolayer graphene (as shown in Fig. 1.8(a)) was grown on $4H-SiC(0001)$ at the *NEST* (National Enterprise for nanoScience and nanoTechnologies) Laboratory [26]. Using an electron-beam evaporator, Ti was deposited on graphene at room temperature in an *Ultra High Vacuum* (UHV) chamber. Then deuterium ($mass = 4$) was used instead of hydrogen ($mass = 2$) for a better signal-to-noise ratio during the *Thermal Desorption Spectroscopy* (TDS) measurements. Through a careful analysis of *Scanning Tunneling Microscopy* (STM) images it was confirmed that Ti atoms tend to cluster forming islands on the surface. In fact, as shown in Figs. 1.8(b) and 1.8(c), titanium atoms form small islands on graphene and these islands grow and become more dense at higher coverages. Fig. 1.8(b) shows data taken with a surface cover-

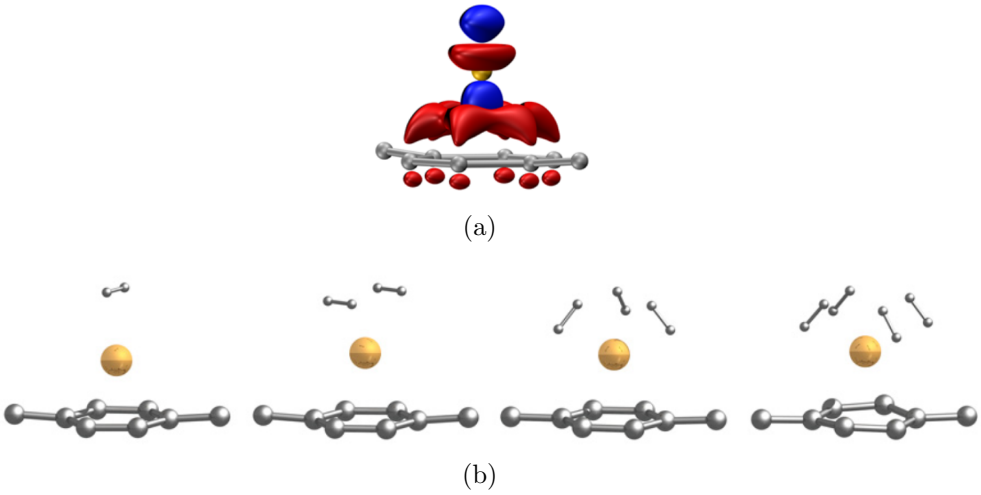

(a)

(b)

Figure 1.7: (a) Electron accumulation (red) and depletion (blue) regions for Ti-decorated graphene. Ti (gold), graphene (silver). (b) Optimized atomic geometries of Ti-decorated graphene with one, two, three, and four H_2 molecules adsorbed on it [30].

age of 16%, (16% of the surface is covered by Ti islands, while the remaining 84% of the surface is bare graphene), whereas the histogram in Fig. 1.8(d) shows the distribution of the island diameters for a surface with 16% coverage. Fig. 1.8(c) refers to a sample with a higher Ti coverage (79%). The analysis shows that for a small amount of deposited Ti the percentage of the covered surface is proportional to the total amount of deposited Ti, whereas for higher coverages the clusters' height increases, so the surface coverage grows more slowly with respect to the total volume of Ti. As a consequence, 100% coverage is achieved only after the deposition of an amount of Ti that corresponds to around 6.5 ML (1 monolayer, ML, is the number of atoms needed in order to form a single layer of material on the surface, only one atom thick, and therefore is related to the total volume of deposited material).

In a successive experiment it was shown how the presence of defects on the graphene surface produces interesting results concerning the clustering issue. In particular, Ti-island formation on graphene as a function of defect density was investigated [31]. Defects in the graphene film were produces by molecular nitrogen sputtering, and the size and distribution of the resulting defects were analyzed by high-resolution STM imaging. Both vacancies (missing lattice atoms) and carbon-atom substitutions (replacement of carbon atoms by nitrogen atoms [32]) were observed, and the defect density was shown to increase linearly with sputter time (from 30 s to 8 min) and sputter energy (between 50 eV and 300 eV). In Fig. 1.9(a) is shown a 100x100 nm^2 STM image of Ti-islands after deposition of 0.55 ML of titanium on a pristine graphene surface. Relatively few islands are present,

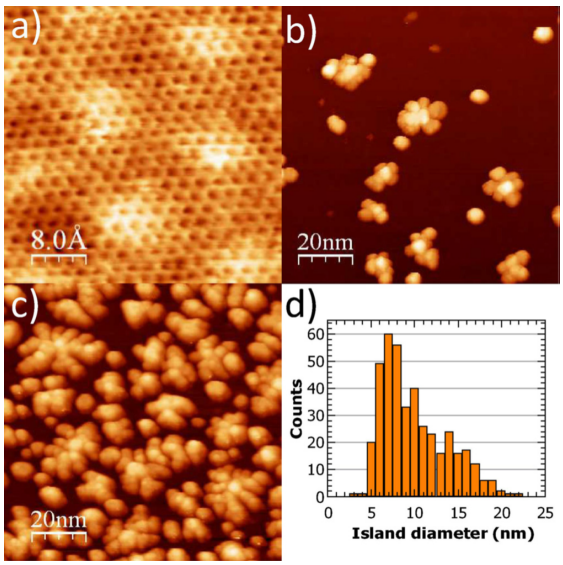

Figure 1.8: (a) Hexagonal graphene lattice before Ti deposition. (b) STM image of a 100×100 nm^2 graphene area with a Ti coverage of 16% that corresponds to 0.56 ML. (c) Ti coverage of 79% that corresponds to 3.3 ML. (d) Size distribution of the clusters in the case of 16% Ti coverage. From ref. [26].

their average diameter exceeds 10 nm and their height is few (2-3) atomic layers. Sputtering the graphene sample for 150 s at an ion energy of 300 eV before titanium deposition leads to a much higher density of islands as shown in Fig. 1.9(b). Here, island diameters are around 5 nm and heights are of one atomic layer only (from ref. [31]).

This reduction of the clustering is due to the lower mobility of Ti atoms after nitrogen sputtering, because Ti tends to form islands on top of defects. Therefore it no longer moves large distances and it does not agglomerate with other titanium into large islands. This results in a larger surface available for hydrogen binding per unit graphene area by a factor ∼4, and thus, an increase in the GD of the system by the same factor [31].

Moreover, the TDS measurement performed on Ti decorated graphene previuosly exposed to molecular hydrogen reveals that the increase of the Ti coverage produce an increase in the signal from the mass spectrometer during the desorption, with the maximum signal for 100% coverage. In addition, when no Ti is deposited on the graphene surface, no D_2 signal could be detected (as can be seen in Fig. 1.10). This result confirms the fact that graphene does not stably bind molecular hydrogen at room temperature.

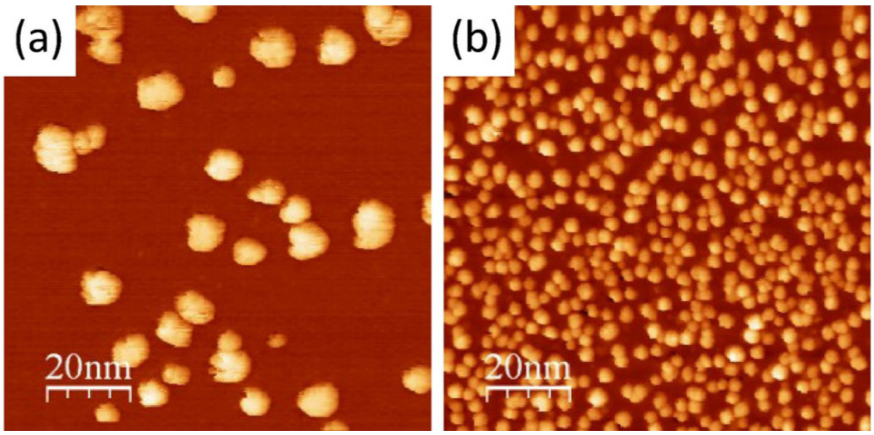

Figure 1.9: (a) 100x100 nm^2 STM image of the distribution of 0.55 ML of Ti on a pristine graphene surface. (b) Similar STM image for Ti-deposition after sputtering the sample at 300 eV for 150 s. [31].

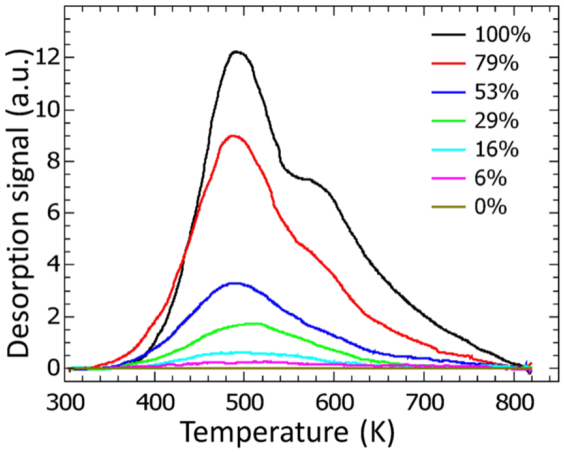

Figure 1.10: TDS signal for several Ti coverages [26].

More recently the interactions between hydrogen and graphene-supported Ti clusters have been further theoretically and experimentally explored [33]. Once again it was confirmed that Ti is not distributed as individual atoms on the graphene surface, but due to the high cohesive energy, it forms clusters. On the basis of the size of the Ti clusters shown in Fig. 1.11(a) (transmission electron microscopy image of Ti clusters on single layer graphene on copper substrate), atomic models of Ti_n (n=1-5) clusters on graphene have been constructed and optimized. The calculations suggest that Ti clusters grow with a trapezoidal shape that was found to have the lowest energy, as depicted in 1.11(b). The size of a Ti_5 cluster is calculated to be 0.53 nm.

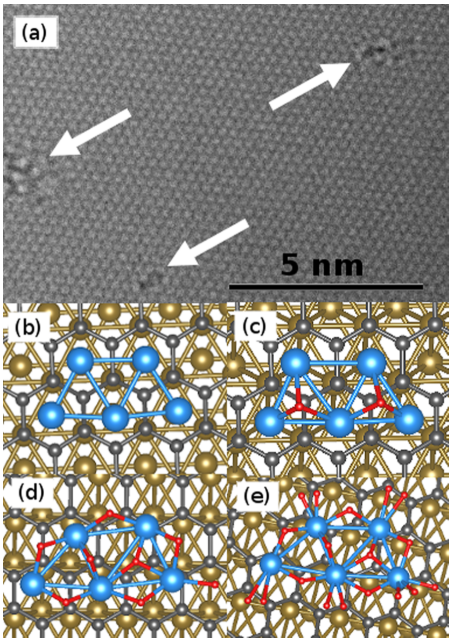

Figure 1.11: (a) TEM image of Ti clusters on single layer graphene. Ti clusters are indicated by white arrows. (b-e) Selected structure models of Ti clusters on graphene: (b) Ti_5, (c) $Ti_5 : 1H_2$, (d) $Ti_5 : 4H_2$, (e) $Ti_5 : 9H_2$. Color code: C (black), Cu (brown), H (red), Ti (blue) [33].

A further investigation on the temperature role in hydrogen adsorption on Ti-functionalized graphene mono-layer [33] allowed to distinguish the contribution of physisorption and chemisorption. Hydrogen desorption analysis of hydrogenated Ti clusters supported on graphene, using TDS, is shown in Fig. 1.12. The TDS spectrum presents three hydrogen desorption peaks: a major hydrogen release occurs at 420 K, while there are two more hydrogen desorption peaks at 150 and 580 K.

The approximate desorption energy barriers E_d is then estimated from the measured desorption temperatures T_d, suggesting that the first peak can be classified

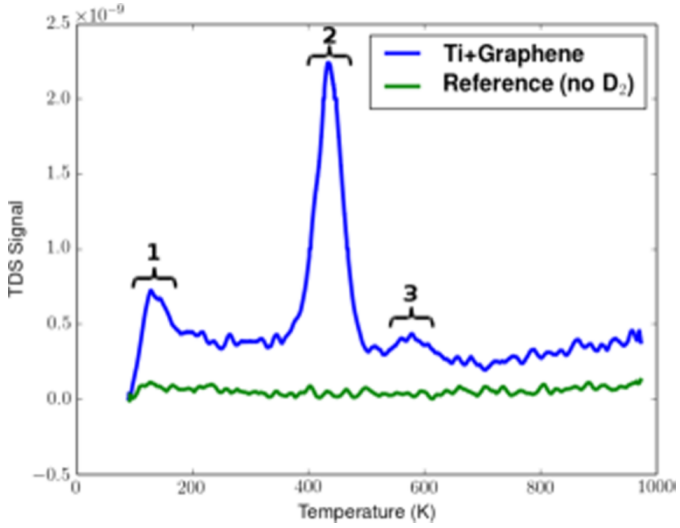

Figure 1.12: TDS spectrum of hydrogen desorption from Ti-decorated graphene. The reference curve (green) was obtained from a sample that was not exposed to molecular deuterium [33].

as related to physisorption (E_d = 0.37 eV/molecule), whereas the other two are related to chemisorption (E_d = 1.1 eV/molecule and E_d = 1.5 eV/molecule).

This results confirm that physisorption of molecular hydrogen occurs at temperatures lower than room temperature, whereas chemisorption takes place in a temperature range interesting for practical application ($\sim$ 150 °C).

In order to reveal the details of the interaction between hydrogen and Ti clusters on graphene, hydrogen adsorption over Ti_n (n=1-5) clusters on graphene was simulated. Hydrogen adsorption at various adsorption sites was considered: on clean graphene, on graphene with a defect site, on graphene with a defect site which is filled by a Ti_1 cluster, and on Ti_n (n=1-5) clusters on graphene. Hydrogen adsorption was performed by adding H_2 in a stepwise manner until the Ti_n clusters are fully hydrogenated.

According to the first-principles calculations, the hydrogen desorption energy on clean graphene is 27 kJ/mol (0.28 eV/H_2), which indicates that hydrogen is adsorbed on graphene by physisorption. Similarly, hydrogen adsorption on Ti_1 clusters on graphene is governed by physisorption as no charge transfer is involved between hydrogen molecules and Ti. However larger clusters behave differently: Ti_2 induces dissociative adsorption of the first hydrogen molecule, with 0.5 electrons transferred from Ti_2 to each H atom. This behavior can be described as a polarized covalent bond with partial ionic character. The second and third H_2 are weakly adsorbed in molecular form, where electron transfer between Ti and H_2 does not occur. A similar behavior is also observed for hydrogen adsorption on

Ti_n (n=3-5).

First-principles calculations reveal that positively charged Ti clusters are not able to dissociate H_2, leading to a weak H_2 adsorption through physisorption, while neutral Ti clusters tend to transfer their electrons toward H_2, resulting in H_2 dissociation and chemical bonding of H. We can conclude that the bond type between H_2 and Ti clusters is strongly dependent on the charge state of the Ti clusters. In particular, initially introduced H_2 tends to dissociate and be adsorbed through chemical bonding due to the large charge transfer from the Ti clusters. As the number of adsorbed H_2 on the Ti cluster increases, the strength and the ionic character of the bonds between H_2 and the Ti cluster weakens. Once Ti clusters are fully positively charged, H_2 is then adsorbed in molecular form via physisorption. Therefore, the detection of three different peaks in the experimental hydrogen desorption (see Fig. 1.12) is explained by the three different types of bonding between hydrogen and titanium clusters based on first-principles calculation (summarized in Fig. 1.13).

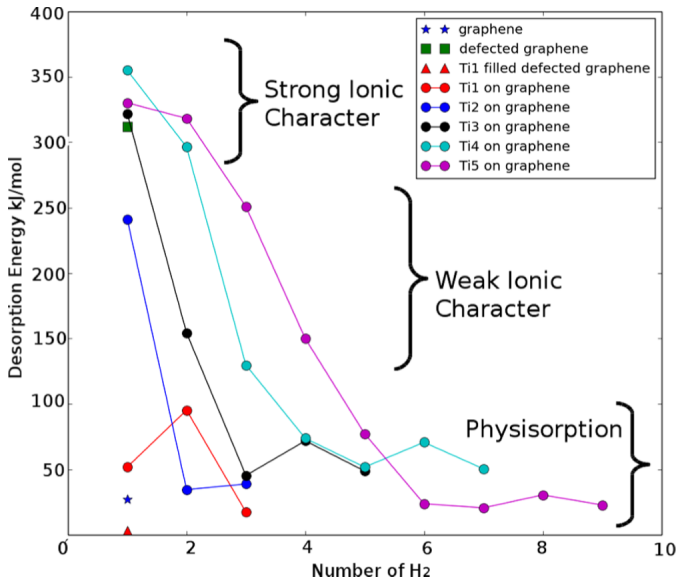

Figure 1.13: Calculated desorption energies for hydrogen adsorbed on clean graphene, defect site of graphene, defect site of graphene filled with Ti_1 cluster, and Ti_n (n=1-5) clusters on graphene. Strong ionic character and weak ionic character represent chemisorption, while physisorption is mediated by van der Waals force. [31].

Our experiments have been performed starting from room temperature, therefore we will only investigate the chemisorption contribution, whereas the physisorption one can be seen solely at much lower temperature (<150 K).

Idea Of The Measurement

2

Every time a chemical reaction occurs, its energy balance can be positive or negative. In the former case, energy from the environment is needed and the reaction is called *endothermic*, because heat (usually) is dragged from the surrounding. On the contrary, when heat is released in the surroundings, an *exothermic* reaction occurs [34]. Therefore, the analysis of the energy change in the system of interest gives useful information about its physical-chemical properties.

While the absolute amount ot energy in a chemical system is difficult to measure or calculate, the *enthalpy* variation ΔH is much easier to work with. The enthalpy variation consists in the change in internal energy of the system plus the work needed to change the system's volume:

$$\Delta H = \Delta U + L = C_p \cdot \Delta T + V \cdot \Delta P \tag{2.1}$$

where C_p is the heat capacity at constant pressure. For processes under constant pressure, ΔH is the thermodynamic quantity equivalent to the total heat exchanged by the system in endothermic or exothermic reactions:

$$\Delta H = \delta Q \tag{2.2}$$

The enthalpy variation is a useful quantity for studying energy exchanges in calorimetric measurements, as in our investigation. In this thesis, in fact, we detect and analyze the exothermic reaction that binds molecular hydrogen to titanium atoms, via two processes: adsorption and desorption. Hydrogen adsorption is measured by calorimetric measurements, from which the total heat released H_r (which corresponds to the ΔH in eq. (2.1)) is extracted. The subsequent hydrogen desorption is investigated by thermal desorption spectroscopy, that allows the estimation of the average binding energy and the amount of hydrogen adsorbed.

The heat released estimated with the calorimetric technique will be compared to the one obtained from the desorption analysis. The good agreement between the results of these two methods verifies the reliability of the calorimetric technique in similar system of microscopic scale.

2.1 Calorimetric technique

Calorimetry is defined as the *measurement of heat*. It has been widely utilized to investigate the microscopic properties of matter, particularly in the presence of processes affecting the sample structure or inducing changes in the sample's thermodynamics condition (chemical reactions, phase transitions, etc.). In fact, whenever a temperature gradient exists within a system, or whenever two systems at different temperatures are brought into contact, energy is transferred via *heat transfer*. The analysis of the energy exchange, performed with several calorimetric techniques, has played an important role in the study of liquid and solid state.

Any calorimeter (an object which allows the measuring of the heat transfer) is basically made by a thermal bath and a measuring chamber which accommodates the sample. While the sample's temperature varies during the process under investigation, the thermal bath act as a controlled region with a fixed temperature, and allow to measure ΔT as a functions of time. Calorimeters can be classified by their measuring principle [35, 36]:

- *heat conduction calorimeters* operate at constant temperature. Heat liberated from a reaction is, to a good approximation, entirely diluted within a heat sink across a path of known thermal conductivity. The instantaneous thermal power ($P = dQ/dt$) generated within the sample is measured by means of a heat-flow sensor located between the sample and the heat sink. The time integration of the thermal power signal gives the total heat associated within the chemical process;

- *heat accumulation calorimeters* allow a rise (or decrease) in temperature of the reaction system for exothermic (or endothermic) reactions. The temperature variation is measured by using a vessel of known heat capacity;

- *heat compensation calorimeters* actively compensate for the heat effects via electrical heating. The calorimetric signal is derived from the energy supplied to the heater in order to maintain the vessel at a constant temperature.

Heat accumulation and heat compensation calorimeters are usually constructed with single vessels, whereas the twin arrangement, first introduced by Joule in 1845, is often used with heat conduction calorimeters. In the last case, the vessels are arranged as perfect twins with the detection units being in opposition to give a differential signal. Thus, extraneous disturbances are canceled, giving long-term stability and high precision for determination of slow processes. It is also possible to allow a reaction to proceed in one vessel while running a control (or *blank*) measurement in the second vessel [37].

However, because these instruments are used for general process as well as for specific thermodynamic events, a careful calibration (supplying a known thermal power or using a chemical reaction of known heat exchange) is fundamental, in order to extract the correct information from the subsequent calorimetric measurements.

Typical examples are *solution* calorimeters and *combustion* calorimeters. The former are usually used for the study of rapid reaction, as heats of solution, heat capacity of liquids, or the enthalpy change of rapid reactions in solution. A schematic diagram is shown in Fig. 2.1. The temperature sensor, plus a device for calibration, and an instrument for mixing reactants are all enclosed within a Dewar flask.

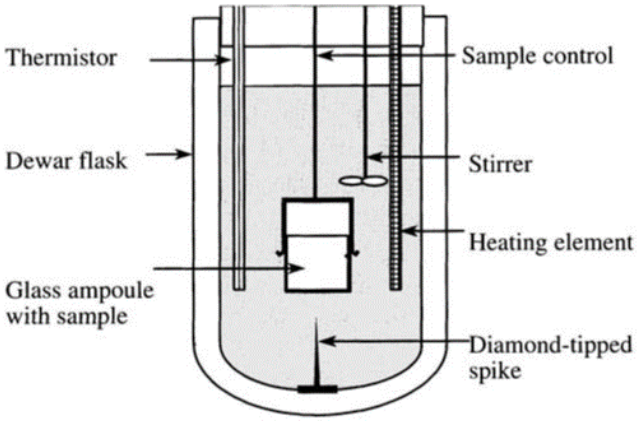

Figure 2.1: Schematic of a solution calorimeter. The assembly may be kept in a thermostated bath. Activation is done by impaling the glass ampule onto the spike, releasing the sample into the content of the Dewar flask. From ref. [36]

Combustion calorimeters allow to obtain thermochemical information (as the stability of materials or the energy content of foods and fuels) from the enthalpy change that occurs on the combustion of a material in a reactive atmosphere, usually oxygen under pressure. In an *adiabatic* (no thermal losses through the surroundings) flame calorimeter, for example, a fuel is completely burnt in oxygen atmosphere (pressure = 1 atm), and the heat is transferred into a known mass of liquid (usually water), whose temperature rise ΔT is measured. The enthalpy change per mole of fuel is given by the following equation:

$$\Delta H = -C_s \frac{\Delta T}{n} \tag{2.3}$$

where C_s is the heat capacity of the system, obtained by calibration, and n is the moles of fuel consumed during the experiment. A scheme of a flame calorimeter for combustion is shown in Fig. 2.2.

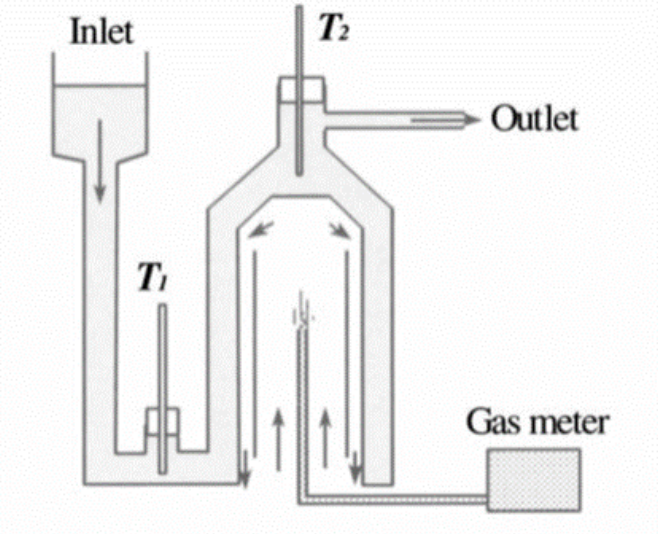

Figure 2.2: Schematic of a flame calorimeter for gases. The combustion of the regulated gas flow raises the temperature of the water from T_1 at the inlet to T_2 at the outlet. From ref. [36]

Calorimetry is generally based on the following equation [38]:

$$\delta Q = C\ \Delta T = c\ m\ \Delta T \tag{2.4}$$

where δQ is the heat exchanged, ΔT is the consequent temperature change, C is the heat capacity, $c = C/m$ is the specific heat capacity, m is the mass of the sample. Assuming time-independent sample mass and specific heat capacity, in case of exothermic heat release H_r, we can write eq. (2.4) in differential form:

$$\frac{\delta H_r}{\delta t} = C\ \frac{\delta \Delta T}{\delta t} \tag{2.5}$$

So, knowing (from calibration) the heat capacity of the system, from the recording of the temperature variation it is possible to extract the heat release.

Finally, in the case of thermal losses, we introduce the heat transfer coefficient λ in order to describe the losses through the sample of interest and its substrate:

$$\frac{\delta H_r}{\delta t} = C\ \frac{\delta \Delta T}{\delta t} - \lambda\ \Delta T \tag{2.6}$$

In general, calorimetric methods involve the use of macroscopic amount of material, of the order of *grams* or *moles* of substances, in order to evaluate the thermochemical properties of materials. Recently, these techniques have been adapted for the use in the microscopic scale, but have focused on the thermal

analysis of thermoelectric devices, such as graphene sheets contacted by metal electrodes [39].

Here, we present an original application of the calorimetric technique in the microscopic scale. The mass of the sample used in the experiment is in the nanograms range, so a tailored device has been developed. In particular, the temperature increase due to the heat released during the exothermic reaction of hydrogen adsorption is detected, and subsequently analyzed, using a graphene monolayer sample transferred on a thermometric sensor a few nanometers thick. As shown in the experimental section, the sample holder (of much higher mass than the sample) acts as the thermal bath of our calorimetric setup, not varying its temperature in the time of our measurements.

2.1.1 Hydrogen adsorption: calorimetric measure

When a Ti-decorated graphene layer is exposed, at room temperature, to molecular hydrogen, we expect that Ti atoms bond H_2 through chemisorption and Kubas interaction. The purpose of this work is to measure the heat released during the adsorption process, that follows from the binding energy of H_2. This methods is complementary to the Thermal Desorption Spectroscopy measurement (TDS, which we also use as a control measurement), that is only subsequent and needs the complete desorption of the hydrogen stored in order to evaluate its amount.

Moreover, the calorimetric technique allows the evaluation of the adsorption of very small amounts of H_2 (on the order of 10^{-10} mol), while a commonly gravimetric measurement evaluates the mass increase of a storage medium after hydrogenation with much higher quantities of H_2 (of the order of grams), and therefore it is not usable for investigation of hydrogen absorption on small samples, like a graphene monolayer.

The idea of this experiment is to utilize a metal film as a thermometer, in order to evaluate the temperature increase of the Ti-decorated graphene as a consequence of the adsorption of H_2. In general, the electrical resistance of metals increases with temperature, following a linear relation (in a limited temperature range [40]):

$$R(T) = R_0 \left[1 + \alpha \left(T - T_0\right)\right] \tag{2.7}$$

where R_0 is the resistance at the reference temperature T_0 and α is the temperature coefficient. Therefore, a temperature increase of the sensor leads to a resistance increase of the metal thermometer that can be detected. Gold film resistance can be measured with volt-amperometric techniques, described in detail in Chapter 3. The sample holder allows four electrical connections which can be utilized for a 2-wire + thermocouple configuration or a 4-wire configuration. During the first thermometer calibration we have utilized a 2-wire + thermocouple setup, whereas in the subsequently measurements, we passed to a more accurate 4-wire setup.

The physical support of the sensor is a $\sim$ 300 μm-thick substrate of silicon whose top face has been oxidized to have a 280 nm layer of SiO_2 as an electrical and thermal insulation. Then a thin layer of 5 nm of titanium is deposited on the substrate to allow the proper sticking of the upper 20 nm layer of deposited gold. Gold has been chosen as metal for the thermometer because of its good resistance temperature coefficient. Moreover it has good thermal and electrical conductivities, and low chemical reactivity that reduces the amount of impurities collected from the environment. Finally a high-quality monolayer of CVD-grown polycrystalline graphene is transferred on the gold layer and titanium is evaporated on the top to functionalize the surface (see Fig. 2.3).

Figure 2.3: Scheme of the sensor (dimensions not in scale). From the top: Ti evaporated (dark gray islands), graphene monolayer (black an white), Au layer (yellow), Ti layer for proper sticking (gray), SiO_2 insulator layer (light blue), Si substrate (dark blue)

During the exposure of the sample to molecular hydrogen we record the resistance evolution. Due to the very low heat capacity of the graphene monolayer, the heat released is quickly transferred to the gold thermometer and the silicon substrate underneath.

In order to thermally decouple as much as possible the sample from the sample holder we don't use metallic foils for direct current heating, but a different sample holder with an integrated tungsten filament of $\sim$ 1 Ω resistance for radiative heating. Furthermore the sample is placed between two sapphire washers and the only direct connections are through four metal wires having 125 μm diameter. Therefore, as shown later on, we can neglect the heat losses toward the sample holder.

The sample can be considered as composed by two parts: the substrate and the sensor (the thermometer plus the graphene layer). For this reason we can contemplate two different limiting scenarios:

- the sensor is thermally decoupled from the substrate;
- the substrate and the sensor are fully thermalized.

2.1.2 First scenario: thermal decoupling

In this first approximation we neglect the heat losses towards the silicon substrate.

In this case we can consider only the upper layers (graphene + gold + titanium) for the temperature increase estimation and the following analysis. Because the silica layer is thin with respect to the silicon substrate, we can add a further estimation in the case of its fast thermalization with the upper layers (graphene + gold + titanium + silica). In the following, titanium layer refers to the layer deposited on silica for the proper sticking of gold, while we can neglect the contribution of Ti layer deposited on graphene. The latter will be in the order of the monolayer, and so its contribute to the heat capacity of the sensor will be negligible. We start by calculating the *heat capacity* of the sensor:

$$C_{sensor} = C_{graphene} + C_{Au} + C_{Ti} + C_{SiO_2} \tag{2.8}$$

where C is the heat capacity and can be calculated knowing c, the *mass heat capacity*, as:

$$\begin{aligned} C_{Au} &= mass_{Au} \cdot c_{Au} \\ C_{Ti} &= mass_{Ti} \cdot c_{Ti} \\ C_{SiO_2} &= mass_{SiO_2} \cdot c_{SiO_2} \\ C_{graphene} &\ll C_{Ti}, C_{Au} \end{aligned} \tag{2.9}$$

We can neglect the heat capacity of the graphene monolayer because of its monoatomic thickness (for the area of our sample, $C_{graph} = 5.8 \cdot 10^{-4} \cdot \mathrm{m}^{-2}$ J/K $\sim 10^{-8}$ J/K [41]). From the well known physical properties of gold, titanium and silica [42], we obtain for gold:

$$\begin{aligned} \rho_{Au} &= 19.3 \text{ g/cm}^3 \\ c_{Au} &= 0.129 \text{ J/K} \cdot \text{g} \end{aligned}$$

for titanium:

$$\begin{aligned} \rho_{Ti} &= 4.507 \text{ g/cm}^3 \\ c_{Ti} &= 0.52 \text{ J/K} \cdot \text{g} \end{aligned}$$

and for silica:

$$\begin{aligned} \rho_{SiO_2} &= 2.196 \text{ g/cm}^3 \\ c_{SiO_2} &= 0.703 \text{ J/K} \cdot \text{g} \end{aligned}$$

Knowing the dimensions (5.10 mm x 5.95 mm of length and width for each layer) of the gold layer:

$$\begin{aligned} t_{Au} &= 20 \text{ nm} \\ A_{Au} &= 30.345 \text{ mm}^2 \end{aligned}$$

the titanium layer:

$$\begin{aligned} t_{Ti} &= 5 \text{ nm} \\ A_{Ti} &= 30.345 \text{ mm}^2 \end{aligned}$$

and the silica layer:

$$t_{SiO_2} = 280 \text{ nm}$$
$$A_{SiO_2} = 30.345 \text{ mm}^2$$

we finally obtain:

$$C_{Au} = \rho_{Au} \cdot t_{Au} \cdot A_{Au} \cdot c_{Au} = 1.51 \cdot 10^{-6} \text{ J/K}$$
$$C_{Ti} = \rho_{Ti} \cdot t_{Ti} \cdot A_{Ti} \cdot c_{Ti} = 0.36 \cdot 10^{-6} \text{ J/K}$$
$$C_{SiO_2} = \rho_{SiO_2} \cdot t_{SiO_2} \cdot A_{SiO_2} \cdot c_{SiO_2} = 13.12 \cdot 10^{-6} \text{ J/K}$$

In the first case, with a fast thermalization of graphene + gold + titanium, neglecting the silica, we have:

$$C_{sensor} = 1.87 \cdot 10^{-6} \text{ J/K} \tag{2.10}$$

In this condition the exothermic heat release rate can be calculated according to the eq. (2.5):

$$\frac{\delta H_r}{\delta t} = C_{sensor}(t) \frac{\delta \Delta T}{\delta t} \tag{2.11}$$

Since C_{sensor} is constant during the measurement, equation (2.11) becomes:

$$H_r = C_{sensor} \cdot \Delta T \tag{2.12}$$

In order to evaluate the temperature increase, we need an estimation of the total energy released in the exothermic adsorption process. From literature, in a similar system [26], has been obtained the following:

- binding energy per molecule of H_2, $E_b \sim 1$ eV$= 1.6 \cdot 10^{-19}$ J
- moles of H_2 adsorbed, $n \sim 10^{-10}$ mol

that correspond to a released heat of:

$$H_r = E_b \cdot n \cdot N_A \sim 9.6 \ \mu\text{J} \tag{2.13}$$

where $N_A = 6.022 \cdot 10^{23}$ mol^{-1} is the Avogadro constant. From (2.12):

$$\Delta T = \frac{H_r}{C_{sensor}} = \frac{9.6 \cdot 10^{-6} \text{ J}}{1.87 \cdot 10^{-6} \text{ J/K}} \approx 5.1 \text{ K} \tag{2.14}$$

If we also consider the silica layer in the fast thermalization, we have:

$$C_{sensor} = 14.99 \cdot 10^{-6} \text{ J/K} \tag{2.15}$$

and from (2.12):

$$\Delta T = \frac{H_r}{C_{sensor}} = \frac{9.6 \cdot 10^{-6} \text{ J}}{14.99 \cdot 10^{-6} \text{ J/K}} \approx 0.64 \text{ K} \tag{2.16}$$

2.1.3 Second scenario: complete thermalization

In the same way we can estimate the temperature increase in the second limiting case, i.e. when the entire silicon substrate is warmed by the heat released during the adsorption process. Knowing that:

$$\rho_{Si} = 2.329 \text{ g/cm}^3$$
$$c_{Si} = 0.705 \text{ J/K} \cdot \text{g}$$
$$t_{Si} = 290 \ \mu\text{m}$$
$$A_{Si} = 30.345 \text{ mm}^2$$

we can calculate the heat capacity of the substrate:

$$C_{Si} = 144.49 \cdot 10^{-4} \text{ J/K}$$

Because of $C_{Si} \gg C_{sensor}$ we can neglect the heat capacity of the sensor and the temperature increase can be estimated as ($C_{Si} = C_{sensor}$):

$$\Delta T \sim \frac{H_r}{C_{substrate}} = \frac{9.6 \cdot 10^{-6} \text{ J}}{144.49 \cdot 10^{-4} \text{ J/K}} \approx 6.6 \cdot 10^{-4} \text{ K} \tag{2.17}$$

As we will show in the experimental section, our thermometer can detect a ΔT in the order of $\sim$0.01 K. Therefore, with this setup we will be able to measure the actual temperature increase during the hydrogenation process, if it will be close to the first scenario, as we expect.

However, because the system is not in equilibrium conditions, in order to extract the heat released from the temperature increase of the sample, we need a dynamic thermal model. In the next section we present the thermal model which will be used for describing the heat transfer through the sample, and therefore calculate the heat release.

2.1.4 Thermal model

To better describe the system we can introduce a very simple thermal model in which the thermometer sensor is heated by the absorption of a thermal power $P(t)$ (therefore its temperature T_{sensor} increases) and in the meantime gives off energy by heat losses towards the substrate. The losses are described by the *heat transfer coefficient* λ, and we assume that the silicon substrate is acting as a thermal bath at fixed temperature T_0, because of its very high heat capacity with respect to that of the sensor. We also assume that the heat capacity of the sensor remains constant during the time interval of the measurement, so we can write (from eq. (2.6)):

$$C_{sensor} \cdot \frac{dT_{sensor}(t)}{dt} = P(t) - \lambda \cdot \Delta T(t) \tag{2.18}$$

where $\Delta T(t) = T_{sensor}(t) - T_0$ [43, 44].

Supplying a fixed power P and considering that $dT_{sensor}(t) = d\left(T_{sensor}(t) - T_0\right) = d\Delta T(t)$, eq. (2.18) becomes:

$$C_{sensor} \cdot \frac{d\Delta T(t)}{dt} = P - \lambda \cdot \Delta T(t) \tag{2.19}$$

which is a non-homogeneous first-order constant-coefficient linear differential equation in the variable $\Delta T(t)$. We impose the initial condition:

$$\Delta T\left(t = 0\right) = 0$$

Then, we can solve eq. (2.19), and the solution is:

$$\Delta T(t) = T(t) - T_0 = \frac{P}{\lambda} \cdot \left[1 - \exp\left(-\frac{t}{\tau}\right)\right] \tag{2.20}$$

where $\tau = C_{sensor}/\lambda$.

In order to extract the unknown heat release which will heat the sensor during the exothermic adsorption of hydrogen, we can adapt eq. (2.19), and use the following equation:

$$\frac{\delta H_r}{\delta t} = C_{sensor} \cdot \frac{\delta \Delta T(t)}{\delta t} + \lambda \cdot \Delta T(t) \tag{2.21}$$

where H_r is the total heat release [45].

2.2 Hydrogen desorption

The adsorption energy is measured more frequently by *desorption*, by breaking the adsorbate-surface bond. When an adsorbed layer of atoms or molecules is heated, the surface species may desorb. This is because their surface residence time depends exponentially on temperature:

$$\tau = \tau_0 \exp\left(\frac{\Delta E}{RT}\right) \tag{2.22}$$

where R is the gas constant, ΔE is the energy needed for the desorption, and τ_0 is the surface residence time in case of no heating.

If the adsorbate is not resupplied from the gas phase, its surface concentration diminishes rapidly with increasing temperature, until the surface becomes clean. For each molecule-substrate combination, there is an optimum temperature at which the adsorbed molecules are removed. By rapidly heating the surface (at

a rate in the order of one or few degrees per second) to this optimum temperature, the adsorbed molecules are removed at a maximum rate before their surface concentration is depleted. From the temperature at which the desorption peak occurs, the activation energy of desorption (which reflects the binding energy of the adsorbed species) can be calculated [46].

2.2.1 Thermal Desorption Spectroscopy

Molecular hydrogen that adsorbs onto the Ti-covered surface minimizes their energy by forming bonds with the atoms of the surface. For a better detection in this work we use molecular deuterium (molecular mass = 4), instead of hydrogen (molecular mass = 2), due to a better signal-to-noise ratio. In fact, as we can seen from the mass spectrum of the residual gas after the bake-out of the UHV chamber, shown in Fig. 2.4, is still present a big partial pressure in correspondence of mass channel = 2, whereas for mass channel = 4 we have a very low base pressure.

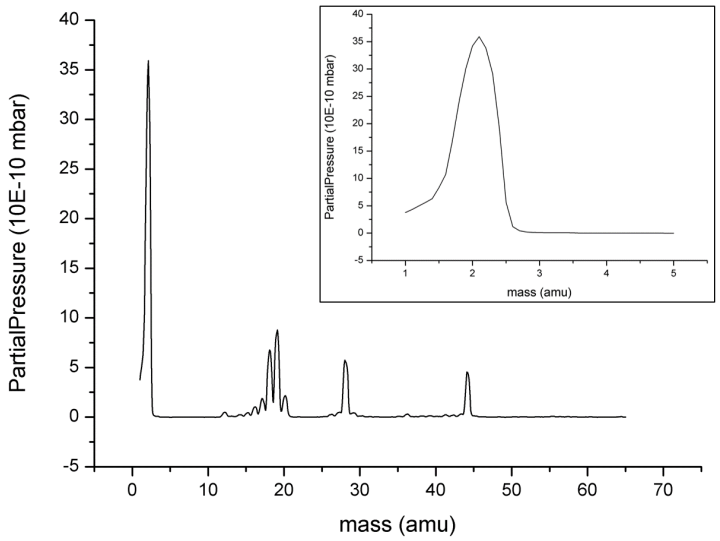

Figure 2.4: TDS spectrum in the mass range (1–65) amu. An intensive peak around mass = 2 is shown, whereas a much lower pressure around mass = 4 is shown in the inset.

In order to evaluate the binding energy of D_2 molecules and the quantity of adsorbed deuterium, it is useful to heat the surface and to measure the desorbed molecules with a mass spectrometer. We record the *desorption spectrum*, i.e. pressure-time curve which gives us information about:

- the quantity of gas desorbed,
- the activation energy of desorption,
- the order of desorption.

The order of desorption gives information on the kinetics of the process, and is related to the probability of dissociation or recombination of the adsorbed molecules. In particular, *first-order* desorption occurs when a molecule desorbs without dissociating. The desorption temperature is independent of coverage and asymmetric peaks with an ascending leading edge are expected. By contrast, a *second-order* desorption occurs when an adsorbed molecule dissociates on the surface, and then desorbs. In this case, we expect symmetric peaks with shared trailing edge shifts to a lower temperature with increasing coverage (as shown in Fig. 2.5, from ref. [47]).

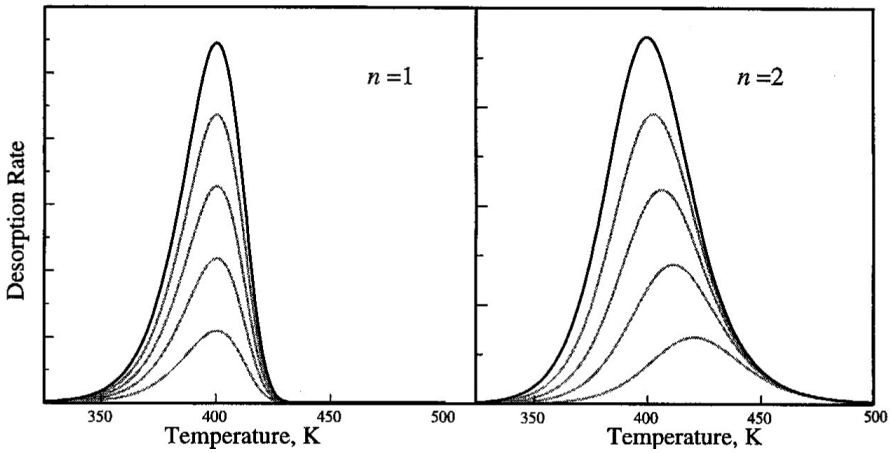

Figure 2.5: TDS spectrum for first-order ($n = 1$) and second-order ($n = 2$) desorption, for different surface coverage.

The temperature dependence of the desorption rate can be described through the *Arrhenius equation* [48]:

$$N(t) = -\frac{d\sigma}{dt} = \nu_n \cdot \sigma^n \cdot \exp\left(-\frac{E_d}{RT}\right) \tag{2.23}$$

where:

n is the order of the desorption kinetics
σ is the surface coverage (in $molecules/cm^2$)
ν_n is the rate constant

E_d is the activation energy of desorption
R is the gas constant

We assume that the sample temperature changes linearly with time following the relation $T = T_0 + \beta t$, where $\beta = dT/dt$ is the heating rate. In case of first-order process, the desorption energy, hence the desorption temperature, is independent of the surface coverage (as seen in [26, 49]), and equation (2.23) is solved to find the peak temperature (from [50]):

$$\frac{E_d}{R \cdot {T_p}^2} = \frac{\nu_1}{\beta} \cdot \exp\left(-\frac{E_d}{R \cdot T_p}\right) \tag{2.24}$$

where T_p is the temperature at which the desorption rate is maximum. Defining τ_m as the time from the start of the desorption ramp to the moment at which T_p is reached, we have:

$$\frac{E_d}{k_B T_p} = A\tau_m \exp\left(-\frac{E_d}{k_B T_p}\right) \tag{2.25}$$

where k_B is the Boltzmann constant and A is the Arrhenius constant (typical value 10^{13} s^{-1}).

2.2.2 TDS spectrum analysis

By recording the partial pressure of H_2 as a function of the sample temperature (this is the TDS spectrum), we can estimate the activation energy of desorption (related to the binding energy) from eq.(2.25), knowing T_p and β.

From the TDS spectrum it is possible to evaluate the total amount of molecular deuterium adsorbed. First of all, we must subtract the background pressure of the vacuum chamber. Then the integration of the TDS curve gives us the area under the curve, which we call F (in mbar·s). If we assume no re-adsorption on the sample during the desorption measurement and we neglect adsorption on the walls of the chamber (see [50]), the amount of desorbed gas at a given pressure is equal to the pumping speed of the vacuum system, which we call S (in L/s). From the gas equation we can write (see [33]):

$$p \cdot V = F \cdot S = n \cdot R \cdot T \tag{2.26}$$

With $R = 8.314$ J/K·mol we can then calculate the number of moles of deuterium desorbed, n, and from it the number of deuterium molecules.

This allows us to estimate the total adsorption enthalpy H_r released during the process, by simply multiplying the binding energy of a D_2 molecule by the total number of molecules adsorbed.

Furthermore the number of molecules adsorbed is needed in order to evaluate the gravimetric density (GD) of the system. This can be calculated as the ratio between the mass of the stored hydrogen M_D and the total system mass:

$$GD = \frac{M_D}{M_{Ti} + M_{Graphene} + M_D} \tag{2.27}$$

In a similar estimation we can use hydrogen, instead of deuterium, in order to evaluate the GD, and therefore the efficiency, of our sample as an actual hydrogen storage system.

Experimental Setup 3

In this chapter the experimental apparatus is described, in order to allow a complete understanding of the measurement setup utilized for the experiments.

First of all, the vacuum environment is explained, the reason for its use, and the equipments directly mounted on the vacuum chamber where the measurements have been performed. The RHK Technology system is equipped with deuterium and nitrogen gas inlets, a residual gas analyzer, titanium and lithium evaporators, low energy electron diffraction and Auger electron spectroscopy systems, and a thermal hydrogen cracker. In particular, only the instruments actually used in our experiments will be described.

After that, the two different setups for measuring the sensor resistance are presented, in the order of their use (first the 4-wire setup, later the Wheatstone bridge setup).

Finally, scanning tunneling microscopy and Raman spectroscopy, both used for characterizing the surface and the quality of the samples, are briefly described.

3.1 Vacuum System

In order to limit the adsorption of impurities and avoid the contamination of the surface of our samples, we perform all measurements in an *Ultra High Vacuum* (UHV) environment. In general, vacuum is used when it is required to decrease the number of molecules per volume. This lowered molecular population can be also viewed as decreased pressure, and therefore as decreased number of molecular collisions, which is fundamental if, as in our case, one wants to deposit a material on a substrate and/or deal with clean surfaces. In fact, in a vacuum system, the material of interest is heated and evaporated from a source to a substrate over a certain distance. If there was gas in the chamber, the gas particles would prevent the evaporated material from reaching the substrate. Moreover, if the gas in the

chamber contains oxygen, it would oxidize the material that we are depositing (titanium in our case, a very reactive element).

Useful parameters for defining the vacuum are: the molecular density (n, number of molecules per cm^{-3}), the mean free path (λ, the average distance a molecule travels before colliding with another particle.), and the monolayer formation time (τ, the time needed to coat a perfectly clean surface with a monolayer of gas), listed in Table. 3.1.

As we decrease the pressure in the vacuum chamber, the average distance between the gas molecules increases, so the particles bump into each other less frequently. The mean free path depends on the size of the gas particles, and on the number of molecules present, and therefore on the pressure:

$$\lambda = \frac{1}{\sqrt{2}\pi d^2 n} \tag{3.1}$$

where d is the particle diameter (in cm), and n is the molecular density (in molecules/cm^3). For air at room temperature (for example), the mean free path can be found from:

$$\lambda(\text{cm}) = \frac{3.8 \cdot 10^{-3}}{P(\text{mbar})} \tag{3.2}$$

Once the pressure in a vacuum system has reached high vacuum levels, most gas particles reside on the walls of the system. Thus, at high vacuum and ultra-high vacuum levels, the pressure in the system is determined by the equilibrium between the adsorption and desorption of gas particles on the surfaces of the walls. At a gas pressure of $1.3 \cdot 10^{-6}$ mbar it only takes 2.2 seconds to create a monolayer of gas on the walls, while at $1.3 \cdot 10^{-12}$ mbar it will take 25 days! This explains why surface analysis equipment usually operates in UHV environment.

Vacuum Level	P (mbar)	n (cm^{-3})	λ (cm)	τ (s)
Rough	10^3	$2.5 \cdot 10^{19}$	$6.7 \cdot 10^{-6}$	$2.9 \cdot 10^{-9}$
($> 10^{-3}$) mbar	1.3	$3.3 \cdot 10^{16}$	$5.1 \cdot 10^{-3}$	$2.2 \cdot 10^{-6}$
High	$1.3 \cdot 10^{-3}$	$3.3 \cdot 10^{13}$	5.1	$2.2 \cdot 10^{-3}$
($10^{-3} \div 10^{-9}$) mbar	$1.3 \cdot 10^{-6}$	$3.3 \cdot 10^{10}$	$5.1 \cdot 10^{3}$	2.2
Ultra-High	$1.3 \cdot 10^{-9}$	$3.3 \cdot 10^{7}$	$5.1 \cdot 10^{6}$	$2.2 \cdot 10^{3}$
($< 10^{-9}$) mbar	$1.3 \cdot 10^{-12}$	$3.3 \cdot 10^{4}$	$5.1 \cdot 10^{9}$	$2.2 \cdot 10^{6}$

Table 3.1: Useful vacuum parameters: pressure interval P, molecular density n, mean free path λ, and monolayer formation time τ for different levels of vacuum [51].

High vacuum levels demand the use of special materials of construction, as *316 stainless molybdenum–alloyed steel* suitable for its characteristics of low gas permeability, non-magnetic, resistance to corrosion, and ability to take a high polish. Common materials for evaporators and sample holders are copper, aluminum, and refractory metals, such as tungsten, while different types of ceramics are used for electrical insulation inside the vacuum chamber. Finally, for the window flanges, pyrex is commonly used, because of its low gas permeability and good vacuum characteristics. Moreover fittings and gaskets used between components in a UHV system must prevent even trace leakage. Therefore, nearly all such fittings are *ConFlat* metal flanges, with knife-edges on both sides cutting into a soft gasket, typically copper. These all-metal seals can maintain integrity to UHV ranges.

To reach UHV conditions, some processing techniques are necessary, such as preheating (*bake-out*) of the entire system for several hours up to 150 °C to remove water and other trace gases, which adsorb on the surfaces of the chamber. The bake-out, as shown in Fig. 3.1, accelerates the outgassing process from the walls, which would require a very long time otherwise.

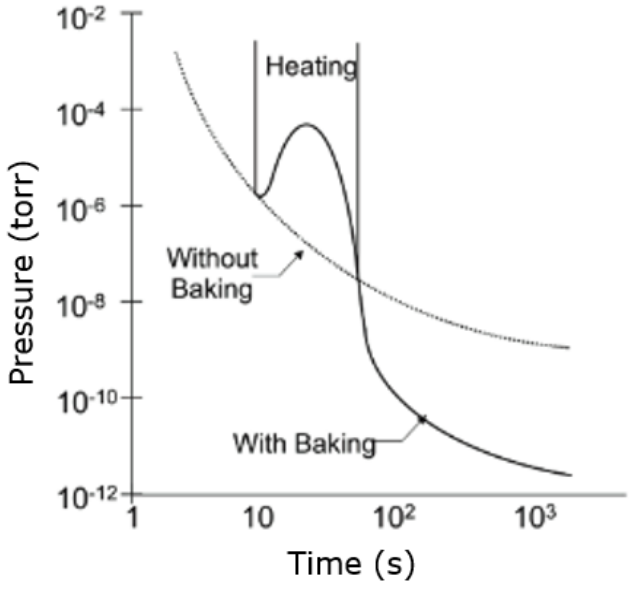

Figure 3.1: Degassing of the system, with and without the bake-out. This shows the advantage of bake-out the UHV chamber, in order to accelerate the outgassing process.

In order to reach these vacuum levels starting from atmospheric pressure (1 atm$\sim 10^3$ mbar), a composed pumping system is required, as described in the following section.

3.1.1 Pumping system

In the first step, starting from atmospheric pressure a *Scroll pump*, is used to get rough vacuum (down to $10^{-2} - 10^{-3}$ mbar), as an oil-free rough pump. The operation principle consists in the use of two interleaving scrolls, one fixed, while the other orbits eccentrically without rotating. The circular motion (see Fig. 3.2) of the orbiting scroll forms crescent shaped spaces into which the gas enters and becomes isolated. Then, the orbiting motion moves the gas towards the center and its volume becomes smaller, therefore the pressure increases. Finally, the crescent is connected to the exhaust port and moved to the next set of scrolls, until the gas is exhausted from the pump.

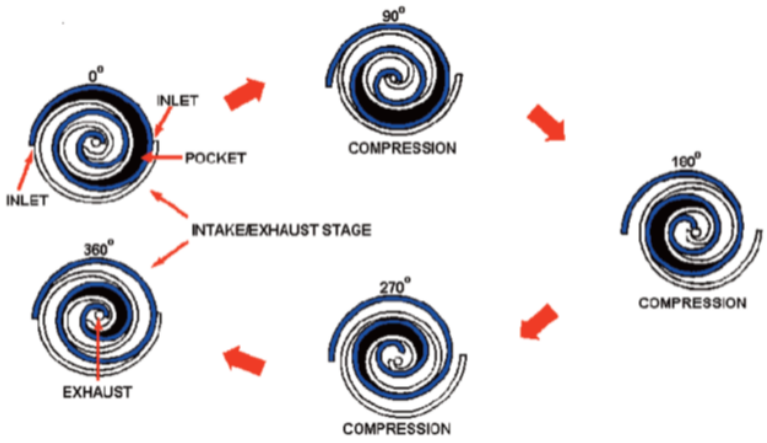

Figure 3.2: Principle of operation of a scroll pump. The gas enters from the inlet valve (left-up), is compressed while moving between the scrolls, and is finally exhausted from the pump (left-down).

The second step is high vacuum (down to 10^{-8} mbar), achieved using a *Turbomolecular pump*. This type of pump employs multiple stages of blade pairs, one consisting in a quickly rotating rotor blade, the other acting as a stationary stator blade. As the gas molecules enter through the inlet valve, they hit the angled blades of the rotor, which transfer momentum to the particles, in the direction of the holes in the stator (see Fig. 3.3). This carries them to the next stage, where they collide again with the rotor surface, and finally are exhausted through the foreline. The performance of a turbomolecular pump is strongly related to the rotation frequency of the rotor. In fact, as rpm increases, the rotor blades deflect more. To increase speed and reduce the deformation, stiffer materials and different blade designs have been suggested. In our case the operational frequency is 1200 rpm.

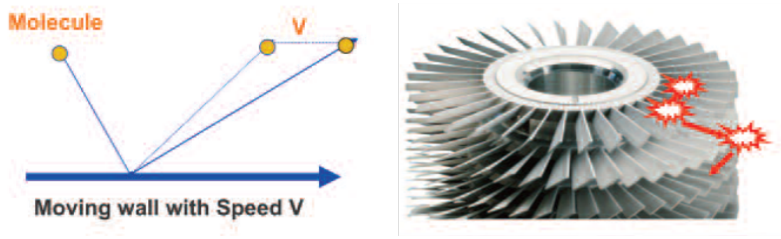

(a) (b)

Figure 3.3: Principle of operation of a turbomolecular pump. (a) Transfer of momentum to the gas particle in the direction of the stator holes. (b) Consecutive collisions with the blades lead particles outwards.

Finally, ultra-high vacuum (down to 10^{-11} mbar) is achieved using an *Ion pump*, which operates via ionization and adsorption of residual gas molecules. The pump configuration includes two titanium plates, acting as cathode, mounted near to several short stainless steel tubes, which act as anode. A strong magnetic field, parallel to the tubes' axes, is used to contain and guide electrons (which are generated applying high voltage to the electrodes) within the circular anode rings. As the gas molecules move into the anode assembly, they are struck by electrons, and, in the collision, they are ionized, and subsequently forced by the high voltage field out of the anode tube towards the cathode plates. There, in the physical impact (*sputtering*) cathode materials (in our case Ti atoms) are ejected toward the anode tube and the positive gas ions can either react with the cathode, forming new solid compounds, or acquire electrons and be reflected toward the anode assembly. These reflected ions still have enough energy to implant themselves physically in the pump surfaces and stop contributing to the vacuum environment pressure.

Besides that, also a *Titanium Sublimation pump* (TSP) is present. It consists of a Ti filament through which a current of around 40 A passes, in order to sublimate titanium. This allows to coat the chamber walls with a clean film of titanium, which reacts with the residual gas molecules hitting the walls, forming stable and solid products, and therefore reducing the chamber pressure. However, because of the reactivity of the films, this procedure is periodically repeated, in order to deposit new clean layers.

In particular, the UHV system used in our experiment consists in three chambers: a fast-entry sample loading chamber (*Load Lock*), a preparation chamber, and the STM chamber (see Fig. 3.5). The load lock is a small chamber used for loading and removing samples, without inducing atmospheric pressure in the entire system. This chamber is pumped by a turbomolecular pump connected to a scroll pump, down to $\sim 10^{-8}$ mbar, and is separated from the preparation chamber by a

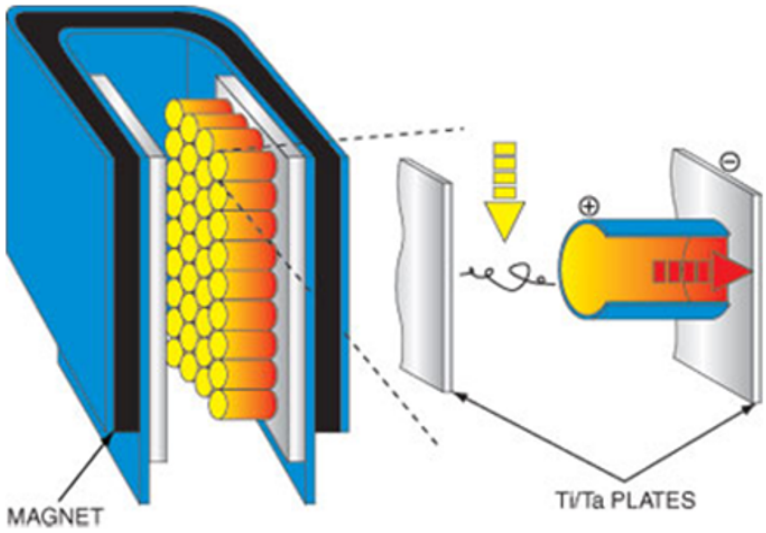

Figure 3.4: Principle of operation of an ion pump. The ionized molecules are accelerated and sputter Ti, when striking the cathode. After chemical reaction with Ti, residual gas molecules are buried into pump surfaces.

manual gate valve. The prep chamber is pumped down to $\sim 10^{-10}$ mbar using an ion pump, and is equipped with a Residual Gas Analyzer, a D_2 inlet gas line, and a titanium evaporator. The calibrations, the calorimetric measurements, and the TDS measurements have been performed in the preparation chamber. Whereas, the STM characterization has been done in the STM chamber of the same RHK system, separated by another manual gate valve, and pumped down to a pressure of the order of 10^{-11} mbar, using a second ion pump. Both the preparation and the STM chambers also have a titanium sublimation pump.

3.1.2 Residual Gas Analyzer

The preparation chamber of our RHK system is equipped with a Residual Gas Analyzer (RGA). This instrument consists in a mass spectrometer of small physical dimensions, that can be connected directly to a vacuum system and whose function is to analyze the gases inside the vacuum chamber. The operational principle is based on the ionization of a small fraction of gas molecules. The resulting ions are separated, detected and measured according to their molecular masses. It is important to note that the quadrupole mass filter must operate in a vacuum environment (at a pressure lower than 10^{-4} mbar), in order to avoid collisional scattering between the ions and the neutral gas molecules.

The total probe equipment consists of three parts: the ionizer (electron impact),

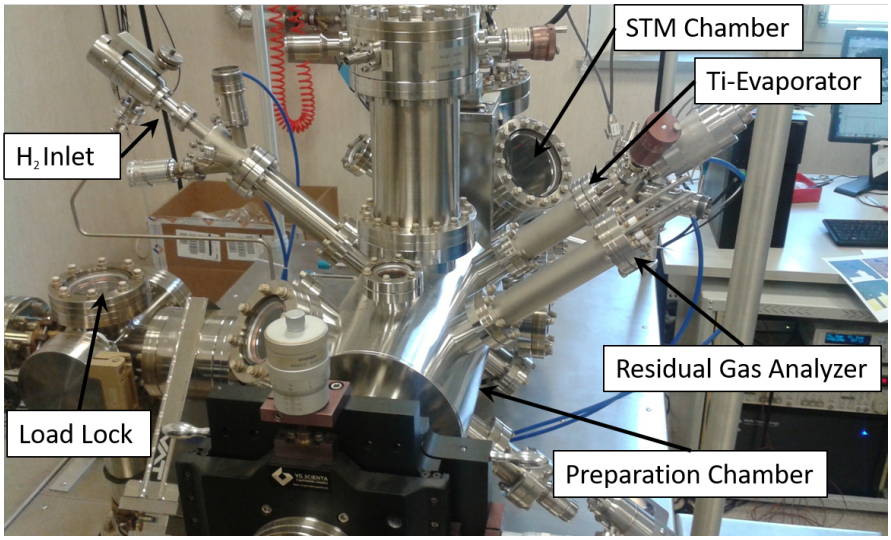

Figure 3.5: Photo of the RHK system, showing the three vacuum chambers and the equipped instruments.

the quadrupole mass filter, and the ion detector (as shown in Fig. 3.6). All of these parts reside in the vacuum space where the gas analysis measurements are made. The detector can measure the ion currents either directly, using a *Faraday Cup*, or through an optional electron multiplier detector, which measures an ion signal proportional to the ion current. In the first case, positive ions enter the grounded detector, strike a metal wall, and are neutralized by electron transfer from metal to the ion, resulting in an electrical current that has the same intensity as the incoming ion current. However, when the pressure is lower than 10^{-7} mbar, the Electron Multiplier upgrade is recommended. The Multi-Channel Continuous Dynode Electron Multiplier (CDEM) consists of a conical system made out of a special resistive glass. When the cone is biased negatively relative to the back end, positive ions are very efficiently attracted and strike the cone at high velocity, producing electrons by secondary electron emission. This process continues, and depending on the bias voltage applied, up to 10^7 electrons come out at the back end and are picked up by a grounded plate. Because of gain degradation is unavoidable, a careful calibration of the measure parameters is fundamental, before using the RGA.

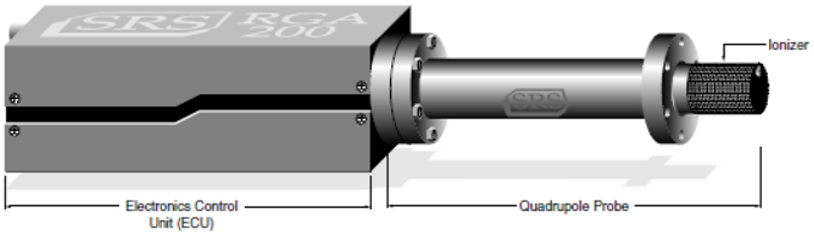

Figure 3.6: Scheme of the Residual Gas Analyzer, composed of an electronic control unit connected to the PC, and a quadrupole probe which ionizes and detects the residual gas.

3.1.3 Ti Evaporator

In order to deposit titanium atoms on the surface of the samples, we need to evaporate Ti in the preparation chamber. The metal evaporator mounted in the prep chamber uses electron bombardment to produce an intense localized heating that warms up of the titanium rod. The rod is placed close to a grounded ring filament and is held at high positive potential. Electrons from the incandescent filament are accelerated and attracted towards the rod, allowing the delivering of an high heating power in a very small area, with maximum possible local temperatures of the order of 3500°C. In order to avoid that the surrounding environment gradually heats up it is necessary to cool down the evaporator, connecting it to a water cooling system (a scheme of the metal evaporator is shown in Fig. 3.7). The titanium atoms flux is started and maintained at a constant value, via the flux controller. This converts the small ion current signal intercepted by the flux electrode into a voltage in the range (0-10)V, and shows a numerical value on the panel screen. After the calibration of the evaporator at a fixed value, possible thanks to a feedback loop control unit, the flux controller allows to repeat the Ti evaporation in the same conditions of constant atom flux.

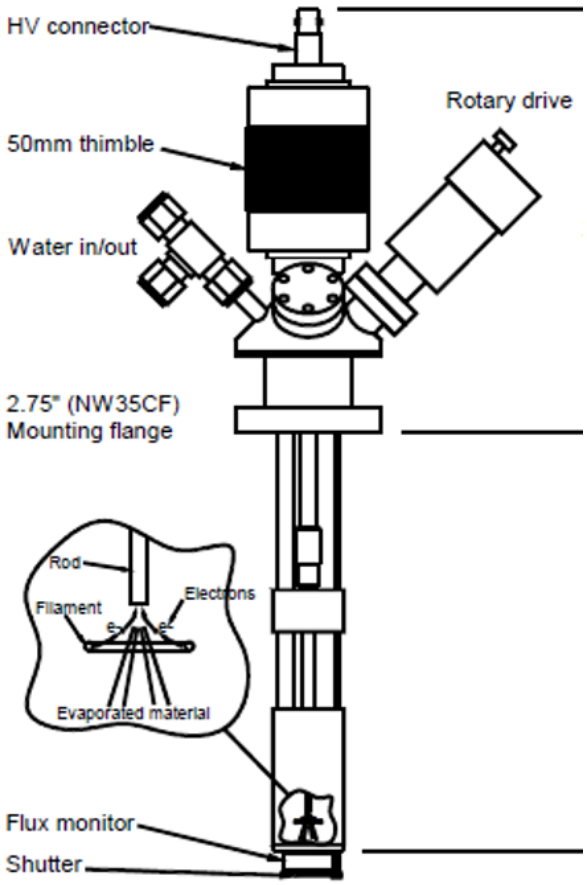

Figure 3.7: Scheme of the metal evaporator with a Ti rod inserted. Electrons from the filaments are accelerated towards the rod, allowing the heating and evaporation of titanium.

3.1.4 Sample Holder

The sample holder for inserting samples in the RHK system is shown in Fig. 3.8. It consists of a double grooved copper body (for firmly grasp it in the sample stage and for its transferring) and a helical top ramp (which acts as base for the scan head during STM imaging). Utilizing this sample holder a round or squared flat sample (of maximum dimensions 7 mm x 7 mm) can be mounted from the top of the ramp, and sandwiched between two sapphire washers in order to be electrically and thermally isolated from the body. The diameter of the round hole of the washers is 5.35 mm. The sample holder has a built-in thermocouple (TC) to measure the sample temperature. The two leads of the TC stick out on one side of the sample holder, as shown in the figure (*TC contacts*). These connections mate with a pair of spring thermocouple contacts on the sample stage, when the sample holder is placed on the stage. In addition there are two more contacts (*add contacts*) on the back of the holder for electrical contacts to the sample. Finally an integrated filament used for radiative heating of the sample is mounted on the bottom of the sample holder (indicated by the red arrow in the figure). Its electrical connections (*filament contacts*) protrude from the side of the holder body, below the TC leads.

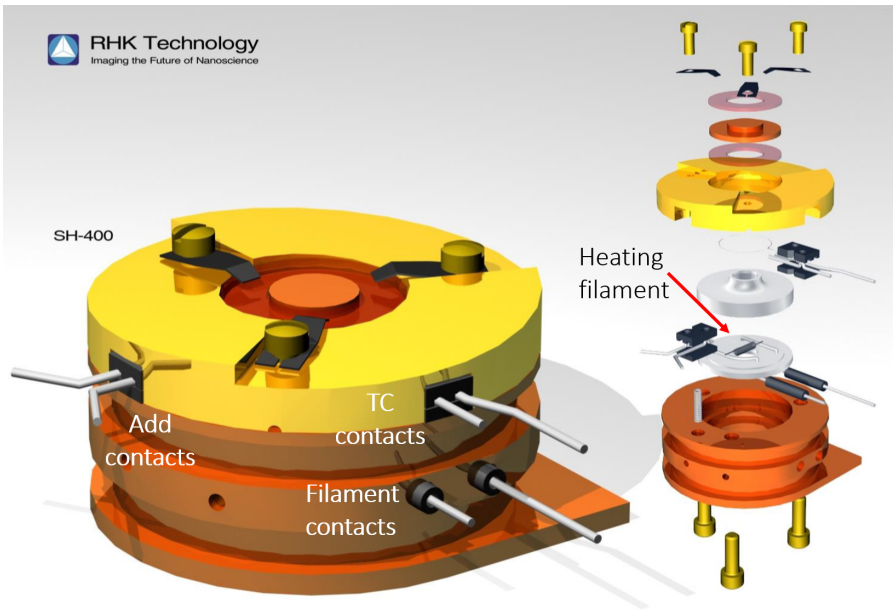

Figure 3.8: Scheme of the sample holder used for the RHK system. The heating filament is shown by the red arrow, and the six leads are separately indicated as filament contacts, TC contacts, and additional contacts.

When using a 2-wire measuring setup (as explained in the following section)

only two electrical contacts to the sample are necessary. Therefore it is possible to keep the TC and have a direct measure of the sample temperature. However, when a 4-wire setup is needed in order to avoid the contact resistance (as explained in the following section), we use both the add contacts and the TC contacts as four electrical contacts to the sample (so no TC can be mounted on the sample).

3.2 Resistance Measurements

In oder to measure the extremely small resistance variation of our gold sensor (in the order of hundredths of Ω) during the hydrogenation process, we need a very sensitive measurement setup. First of all we supply the sensing current (5 μA) and we collect the voltage signal through a Lock-In Amplifier. Moreover, we initially performed the measurements using a 2-wire setup for a calibration with a thermocouple. Subsequently, we pass to the 4-wire setup in order to avoid the contact resistance, and finally we use the Wheatstone bridge setup in order to increase the measure sensitivity. In the following section these experimental methods are briefly explained.

3.2.1 Lock-In Amplifier

Lock-In Amplifiers (LIAs) are commonly used to detect and measure very small signals (down to a few nV), even when the signal is obscured by noise sources. The operation principle is based on the Phase-Sensitive Detection technique, that permits to single out the component of the signal at a specific reference frequency and phase. Noise signals at frequencies other than the reference frequency are rejected and do not affect the measurement.

Typically an experiment is modulated at a fixed frequency (from an oscillator or function generator) and the lock-in detects the response from the experiment at the reference frequency, as shown in the diagram below, where the ref signal is a square wave at frequency ω_r (see Fig. 3.9). The LIA used in our measurements generates its own sine wave (shown as the reference in the diagram):

$$V_L \sin(\omega_L t + \theta_{ref}) \tag{3.3}$$

whereas the response might be the signal waveform:

$$V_{sig} \sin(\omega_r t + \theta_{sig}) \tag{3.4}$$

where V_{sig} is the signal amplitude. The LIA amplifies the signal and then multiplies it by the lock-in reference using a phase-sensitive detector (PSD). The output of

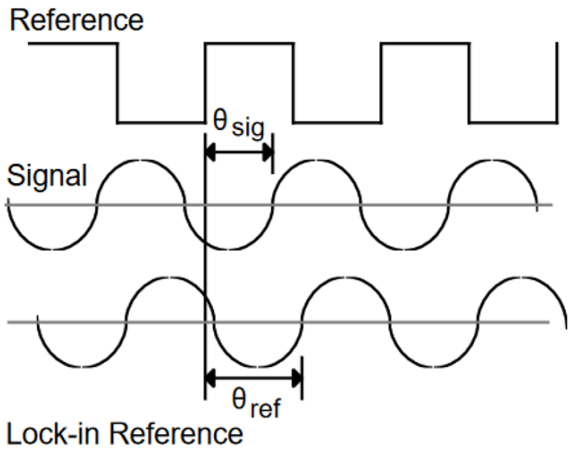

Figure 3.9: Diagram of the reference and output signals, and the lock-in reference.

the PSD is simply the product of two sine waves:

$$\begin{aligned} V_{psd} &= V_{sig} V_L \sin(\omega_r t + \theta_{sig}) \sin(\omega_L t + \theta_{ref}) = \\ &= \frac{1}{2} V_{sig} V_L \cos\left[(\omega_r - \omega_L)\, t + \theta_{sig} - \theta_{ref}\right] + \\ &\quad - \frac{1}{2} V_{sig} V_L \cos\left[(\omega_r + \omega_L)\, t + \theta_{sig} + \theta_{ref}\right] \end{aligned} \tag{3.5}$$

The PSD output consists in two AC signals, one at the difference frequency $(\omega_r - \omega_L)$ and the other at the sum frequency $(\omega_r + \omega_L)$. If this signal is passed through a low pass filter, the AC signals are removed, and only if $\omega_r = \omega_L$ the difference component will be the DC signal (and therefore will be left):

$$V_{psd} = \frac{1}{2} V_{sig} V_L \cos\left(\theta_{sig} - \theta_{ref}\right) \tag{3.6}$$

This is DC signal, proportional to the signal amplitude.

Now suppose the input is made up of signal plus noise. The PSD and low pass filter only detect signals whose frequencies are very close to the lock-in reference frequency. Noise signals at frequencies far from the reference are attenuated at the PSD output by the low pass filter (neither $\omega_{noise} - \omega_{ref}$ nor $\omega_{noise} + \omega_{ref}$ are close to DC). Noise at frequencies very close to the reference frequency will result in very low frequency AC outputs from the PSD ($|\omega_{noise} - \omega_{ref}|$ is small). Their attenuation depends upon the low pass filter bandwidth and roll-off. A narrower bandwidth will remove noise sources very close to the reference frequency, a wider bandwidth allows these signals to pass. The low pass filter bandwidth determines

the bandwidth of detection. Only the signal at the reference frequency will result in a true DC output and be unaffected by the low pass filter. This is the signal we want to measure.

3.2.2 2-wire Setup

At the beginning, we need to correlate the electrical power supplied to the heating filament of the sample holder with the temperature of the sample. For that reason, because our sample holder has only four electrical connections, we perform the initial calibration using a thermocouple, for the thermometer temperature, and a 2-wire setup for measuring the resistance variation of the gold thermometer via Ohm's Law ($R = V/I$) (see Fig. 3.10).

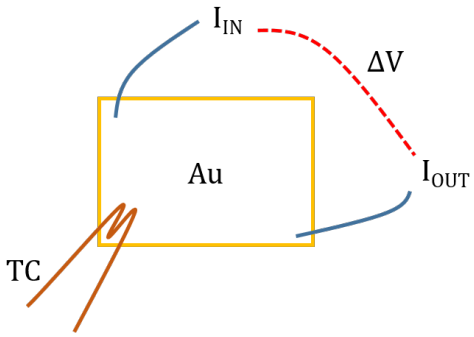

Figure 3.10: Scheme of the 2-wire setup with the thermocouple for the power calibration. We supply the sensing current and we read the voltage drop with the same 2 contacts.

When the resistance is measured via Ohm's Law using the same two contacts for both supplying current and measuring the voltage difference, the *contact resistance* cannot be avoided. This consists in the contribution to the total resistance of the system which can be attributed to the contacting interfaces of electrical connections, as opposed to the intrinsic resistance, which is an inherent property, independent of the measurement method.

3.2.3 4-wire Setup

Using instead the 4-wire setup it is possible to measure the exact resistance of the sensor (see Fig. 3.11).

In a 4-point probe measurement one pair of leads is used to inject the sensing current, while a second pair of leads, in parallel with the first, is used to measure the voltage drop across the sensor. In this case, since almost no current flows to the voltmeter, there is no potential drop across the voltage measurement leads,

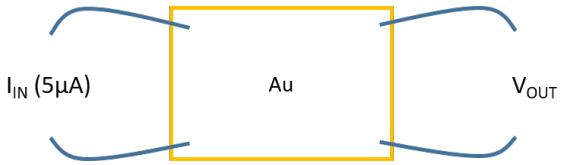

Figure 3.11: Scheme of the 4-wire setup which allows to directly measure the actual sensor resistance. We supply the sensing current using the TC contacts and we read the voltage drop using the add contacts.

so the contact resistance drop is not included. This is an advantage for precise measurement of low resistance values, so this setup is commonly used to measure the resistance of thin metal films.

3.2.4 Wheatstone Bridge

In order to increase the measurement sensitivity and therefore to be able to measure very small resistance variations, a *Wheatstone bridge* can be utilized. A Wheatstone bridge is an electrical circuit commonly used to measure an unknown electrical resistance by balancing two arms of a bridge circuit, one of them including the unknown component (see the scheme in Fig. 3.12). Notwithstanding this is a 2-probe measurement, and so the contact resistance cannot be avoid, the Wheatstone bridge exploit the concept of difference measurement, which are extremely accurate.

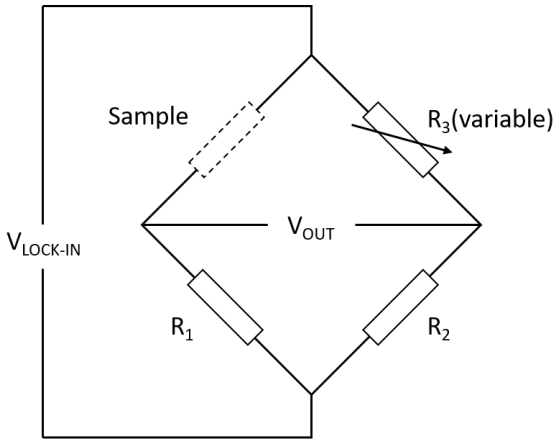

Figure 3.12: Scheme of the Wheatstone bridge setup: $R_1 = R_2$ and R_3 is variable, so to be able to balance the bridge, setting it as close as possible to R_{sample}.

Usually the unknown resistance is fixed, so for balancing the bridge it is nec-

essary to regulate the variable resistance, until the voltage output is zero and no current flows through the detecting instrument. In this condition the unknown resistance equals the value assumed by the variable resistance. In our experiment, on the contrary, the sample resistance varies during the hydrogenation measurement, because of the temperature increase of the sensor. For this reason we balance the bridge as much as possible, in order to have the lowest possible voltage output, and we analytically resolve the bridge circuit, obtaining the value of the sample resistance:

$$R_{sample} = \frac{R_1 R_3 \cdot V_{LIA} + (R_3 + R_2)\, R_1 \cdot V_{OUT}}{R_2 \cdot V_{LIA} - (R_3 + R_2) \cdot V_{OUT}} \tag{3.7}$$

where V_{LIA} is the input voltage from LIA, V_{OUT} is the voltage difference between the two arms of the bridge, R_1 and R_2 are the fixed resistances, and R_3 is the variable resistance. The Wheatstone bridge has been assembled on a breadboard, welding to the metallic tracks the R_1 and R_2 resistances (in the order of 1 KΩ, ideally equal), and connecting the variable R_3 (in the range of $1 \div 13$ Ω), as shown in Fig. 3.12.

The sample is mounted in the sample holder in the same configuration of the 4-wire setup (see Fig. 3.11). This allows us to swap from one setup to the other without removing the sample from the high vacuum chamber (a very time consuming procedure) or changing the contact positions on the sample.

3.3 Raman Spectroscopy

In order to verify the quality of the monolayer graphene transferred on the gold sensor, *Raman Spectroscopy* has been performed. A laser with a known wavelength is focused onto a material of interest and the photons scattered by the material are collected and analyzed in terms of such parameters as wavelength, polarization, and scattering angle. Most of the scattered light has the same wavelength as the laser, but a small amount of the scattered light changes wavelength. When the wavelength is unchanged during the scattering process, it is known as elastic light scattering or Rayleigh scattering. On the other hand, a small amount of the scattered radiation has a different frequency from the excitation photon due to the creation or annihilation of a quantized excitation in the material. This light scattering process is inelastic and is known as the Raman effect. Raman spectroscopy is nowadays acknowledged as an extremely valuable nondestructive method for extracting structural and chemical information of a material. In this thesis work, Raman spectroscopy is only used as a tool for distinguish how many graphene layers were present in the sample.

In fact, graphene has a characteristic Raman spectrum which has become a standard in both identifying the number of layers in the sample as well as the

quality of the graphene [52]. Using a 532 nm green laser in order to illuminate the sample, there is a first order Raman mode in graphene known as the G mode. The corresponding phonon is an in-plane stretching motion of the two sublattices, A and B, of graphene. In monolayer graphene, the G mode is a sharp peak centered at $\sim$1585 cm^{-1}. In addition, there is a second very prominent sharp Raman peak at around $\sim$2700 cm^{-1} known as the $2D$ peak. This is the second order overtone of a different plane vibration known as D peak, at $\sim$1350 cm^{-1}.

The $2D$ peak is sensitive to the number of graphene layers. In fact, from literature (see Fig. 3.13) we can see the difference between Raman spectra of a multilayer graphene and a monolayer graphene: because of added forces from the interactions between layers if are, the spectrum change and the narrow $2D$ single peak becomes a combination of two or more smaller peaks that are seen as a broader, less intense, peak ([53, 54, 52]).

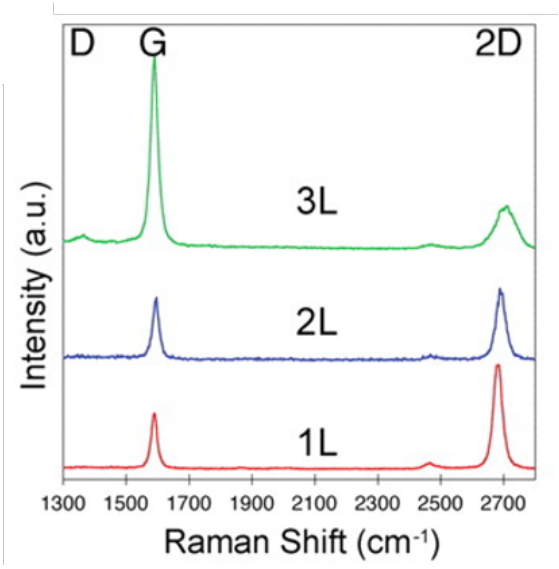

Figure 3.13: Raman spectrum of multilayer and monolayer graphene [54].

3.4 Scanning Tunneling Microscopy

A *Scanning Tunneling Microscope* (STM) is an imaging instrument, used for investigating surfaces at the atomic level (in the scale of Å), and therefore visualizing the atoms' positions on the sample surface. The STM is based on the quantum tunneling effect: when a conductive tip is brought very close to the surface to be examined, a bias voltage applied between the tip and the surface can allow electrons to tunnel through the vacuum (or air) between them. The resulting tunneling current is a function of several parameters, as tip position, applied bias voltage, and the local density of states (LDOS) of the sample [55]. Once tunneling is established, the tip's bias and position with respect to the sample can be varied. Moving the tip across the sample in the $x-y$ plane allows to obtain surface images from the resulting changes in the current.

In classical mechanics (in a simple one dimensional model), an electron with energy E, moving under a potential $U(z)$ can be described by the equation:

$$E = \frac{p_z^2}{2m} + U(z) \tag{3.8}$$

If $E > U(z)$ the electron has a momentum $p_z \neq 0$. On the contrary, if $E < U(z)$, the electron cannot penetrate the potential barrier described by $U(z)$.

In quantum mechanics, instead, the same electron can be described by a wavefunction $\psi(z)$, which follow the Schrödinger equation:

$$E\psi(z) = -\frac{\hbar^2}{2m} \cdot \frac{d^2}{dz^2}\psi(z) + U(z)\psi(z) \tag{3.9}$$

Considering a piecewise-constant potential, the solutions of Schrödinger equation are nonzero in both the classically allowed and forbidden regions (see Fig. 3.14). For the case of $E > U$, the solution is:

$$\psi(z) = \psi(0)e^{\pm ikz} \tag{3.10}$$

with $k = \sqrt{2m(E-U)}/\hbar$ the wave vector, and $p_z = \hbar k = \sqrt{2m(E-U)}$ the momentum. Where, on the contrary, $E < U$ the solution is:

$$\psi(z) = \psi(0)e^{-\kappa z} \tag{3.11}$$

with $\kappa = \sqrt{2m(U-E)}/\hbar$ the decay constant. This equation describes the state of an electron decaying in the (positive) z direction. The probability density to observe an electron near a chosen point z is then proportional to $|\psi(0)|^2 e^{-2\kappa z}$, which is different from zero in the potential barrier region. Thus, also the probability to penetrate the barrier is nonzero.

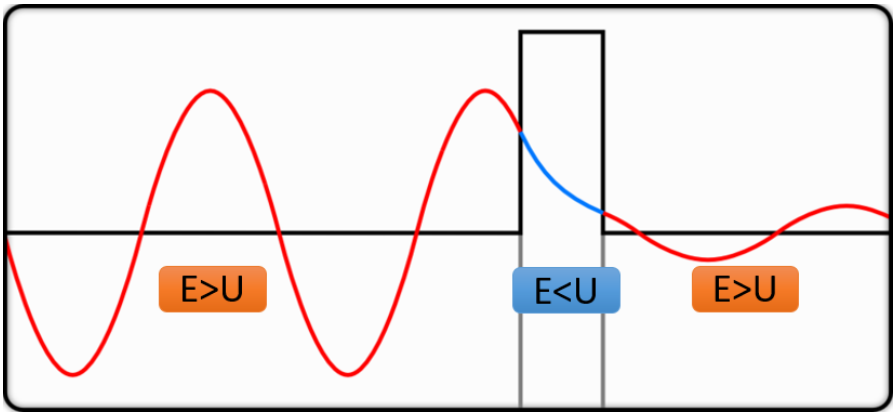

Figure 3.14: Solution to the Schrdinger equation in the classically allowed region (red line) and forbidden region (blue line). E is the initial energy of the electron, whereas U is the potential barrier.

In the case of tunneling the tip and the sample wave functions overlap, therefore there is a finite probability for the electron to overcome the barrier and pass from the tip to the sample (or viceversa). If $V_b = 0$ the probability is the same for the two directions, so no net current flows, whereas when a bias voltage $V_b \neq 0$ is applied, one direction is more probable than the other, and a tunneling current starts. If V_b is small (so that $eV_b \ll \phi$), we can consider $U - E \approx \phi$, where ϕ is the work function of the surface (the minimum energy needed to extract an electron from the Fermi level, the highest occupied level, to the vacuum level). In this condition, only electronic states very close to the Fermi level, within eV_b, are excited and can tunnel across the barrier (see Fig. 3.15).

Hence, the probability P for an electron, which for $z = 0$ is at the sample surface, in the state ψ_n to reach the tip surface at $z = s$, is:

$$P \propto |\psi_n(0)|^2 e^{-2\kappa s} \tag{3.12}$$

with $\kappa = \sqrt{2m\phi}/\hbar$. We can estimate the decay constant, using eV as unit of the work function, from:

$$\kappa = 0.51\sqrt{\phi(\text{eV})}\ \text{Å}^{-1} \tag{3.13}$$

Using as common distance s in the order of 10 Å, and typical value for ϕ in metals $\sim$4 eV, therefore the tunneling current decreases by one order of magnitude for a distance increase of $\sim$1 Å.

Introducing $M_{\mu\nu}$, the tunnel matrix between tip (μ) and sample (ν), and $f(E)$, the Fermi function, the Bardeen formalism [56] gives a more complete result for

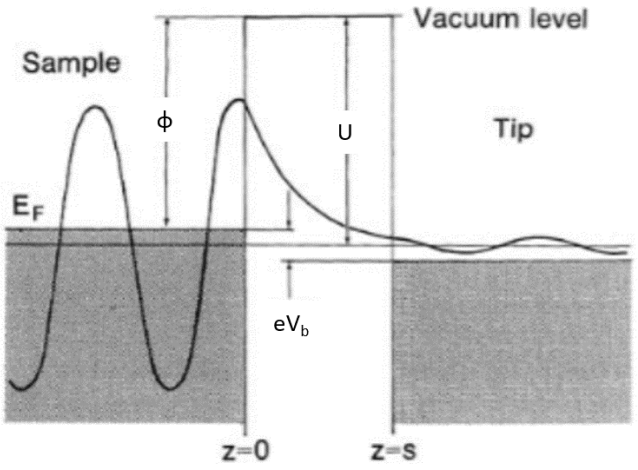

Figure 3.15: Scheme of a one dimensional metal-vacuum-metal tunneling junction, from ref [55].

the tunneling current:

$$I = \frac{2\pi e}{\hbar} \sum_{\mu\nu} f(E_\mu)[1 - f(E_\nu + eV_b)]|M_{\mu\nu}|^2 \delta(E_\mu - E_\nu) \tag{3.14}$$

An actual STM consists of a tube scanner, which moves the probe tip, via three-dimensional piezoelectric elements, on the sample surface. Moving the tip in the z direction and applying a bias voltage, the tunneling conditions can be established. If the tip is moved across the sample in the $x - y$ plane, the changes in surface height and density of states causes changes in current, which are mapped in images. It is possible to measure both the change in current with respect to position (*constant height mode*), or the height, z, of the tip corresponding to a constant current (*constant current mode*). The benefit to using the former mode is that it is faster, as the piezoelectric movements require more time to register the height change in constant current mode than the current change in the latter mode. However, keeping the tip at a constant height can be dangerous, especially when scanning highly corrugated samples, because of the risk of damaging both the tip and the surface. Finally the current is amplified and the data are processed and shown on the computer (a scheme of an STM is shown in Fig. 3.16).

In order to isolate the STM system from the external vibrations as much as possible, the STM unit must be as rigid as possible, and the transmission of environmental vibrations to the STM unit have to be limited. The vibration isolation system generally consists of a set of suspension springs and a damping mechanism to reduce as much as possible the vibrations transmitted to the system. In order

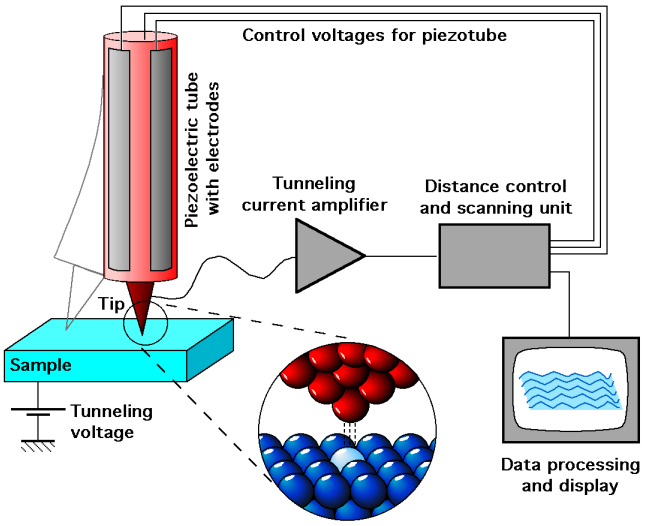

Figure 3.16: Schematic view of an STM.

to better reduce vibrations, the STM is usually placed on a table which must be in floating condition (using gas spring legs) to allow isolation from the ground vibrations. The STM scanning occurs in floating conditions and (usually) in vacuum, to reduce as much as possible the external noise.

Sample Preparation and Calibration

4

4.1 Thermometer Preparation

The structure of the thermometer is schematically shown below, in Fig. 4.1.

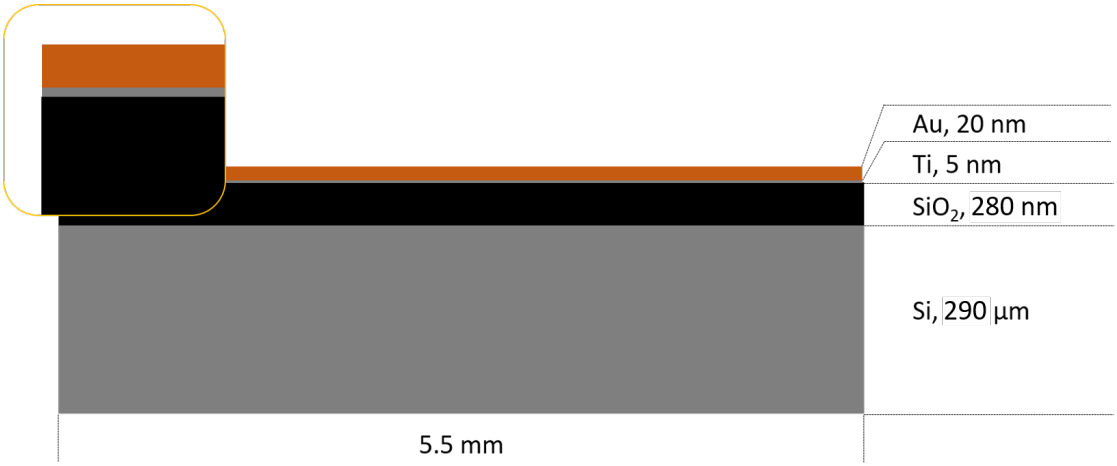

Figure 4.1: Structure of the sample.

The physical support of the sensor is a ∼300 μm-thick substrate of silicon whose top face has been oxidized to have a 280 nm layer of SiO_2 acting as an electrical and thermal insulator. Then a thin layer of 5 nm of titanium is deposited via metal sputtering on the substrate to allow the proper sticking of the upper 20 nm layer of gold (also deposited via metal sputtering). Gold has been chosen as metal for the thermometer because of its good resistance temperature coefficient. Moreover it has good thermal and electrical conductivities, and low chemical reactivity that reduces the amount of impurities collected from the environment. Furthermore we

need a very thin layer of metal in order to have a thermometer with a very low heat capacity and therefore obtain an high sensitivity for the temperature increase. On the other hand we measure the thermometer resistance through metal wire contacts thus we need a thicker substrate in order to give robustness to the sample.

The graphene sheets have been prepared in the controlled environment of the clean room, via Chemical Vapour Deposition (CVD) on copper substrate, and then have been transfered on the thermometer to obtain the final samples. They are then mounted on the sample holder in order to perform the experiment in the UHV chamber. The mounting has been made using gloves and clean tools to avoid as much as possible contamination of the samples and to reduce the pumping time in the UHV chamber.

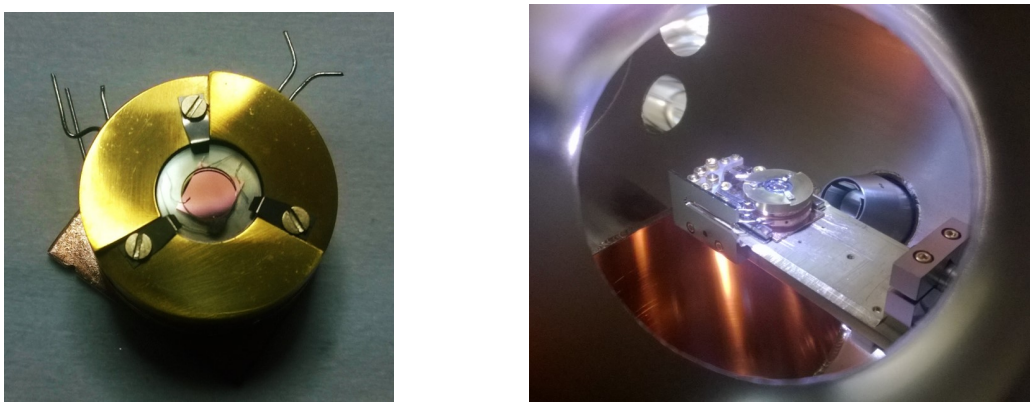

(a) (b)

Figure 4.2: (a) Thermometer mounted on the sample holder in four-wire setup. (b) Sample in the UHV chamber.

In the following sections we will describe the procedures for the characterization of the samples, in the order listed below:

- calibration of the thermometer, and STM images of the gold surface;
- transfer of the graphene monolayer, calibration, and characterization via Raman spectroscopy and STM;
- calibration of the Ti evaporator, evaporation of Ti on graphene, STM images of Ti on graphene;
- calculation of the heat transfer coefficient;
- calibration of the RGA.

4.2 Thermometer Calibration

Before using our sensor as a thermometer we need to know its thermal and electrical property, and perform a proper and complete calibration. As a result of the calibration, the temperature coefficient and the electrical resistivity of the gold thermometer are obtained for different measuring setups. This allows us to compare these parameters with the standard ones, listed in literature.

4.2.1 Two-Wire Measurements and Power Calibration

The manipulator stage in the UHV chamber (and thus the sample holder) has six electrical contacts: two are used to supply current to a tungsten filament placed in the lower part of the sample holder to heat the sample, two are connected to a thermocouple mounted on the sample and the last two of them are used to supply current to the sample or read the voltage drop. Because we want finally to use a four-wire setup for the measurements, first of all we need to calibrate the temperature increase of the sample during the heating using the filament. Hence we mount a thermocouple in one corner of the sample and the two other contacts are placed in two opposite corners in order to supply the sense current in the most uniform way. Before starting the real measurement, the best experimental configuration must be chosen. To avoid heating the sample with the sense current, it is kept very low by mounting a 467 kΩ at the output of the Lock-In Amplifier. Because the LIA output can be set in the range $(0 - 10)$ V, the allowed sense current ranges from 0 to 20 μA. After some preliminary measurements the sense current has been fixed at 5 μA because this is the best value with regard to the signal to noise ratio. Then the voltage difference between the two contacts is measured by the lock-in amplifier and the thermometer resistance is calculated.

The first step of the experiment is a preliminary degassing of the sample, supplying current to the filament up to 2 A in two slow ramps of 20000 s for heating, 20000 s for cooling and 3000 s of pause at the end before the next ramp. Finally we perform the measurement doing a slow ramp up to 2.5 A, with 15000 s of heating and 15000 s of cooling, in order to slowly heat the sample and allowing possible mechanical adjustments of the contacts. During the heating ramp we record the temperature of the gold sensor measured by the thermocouple, the current and the voltage supplied to the filament which give us the absorbed power. The ramps are controlled via LabView and we record data with a time interval of 1 s or 5 s and a time constant of integration of the lock-in amplifier of 0.3 s or 1 s.

We can fit the temperature data with a fourth-order polynomial equation:

$$T(P) = T_0 + \beta_1 \cdot P + \beta_2 \cdot P^2 + \beta_3 \cdot P^3 + \beta_4 \cdot P^4 \tag{4.1}$$

as seen in Fig. 4.4, This calibration has been performed several times on the first

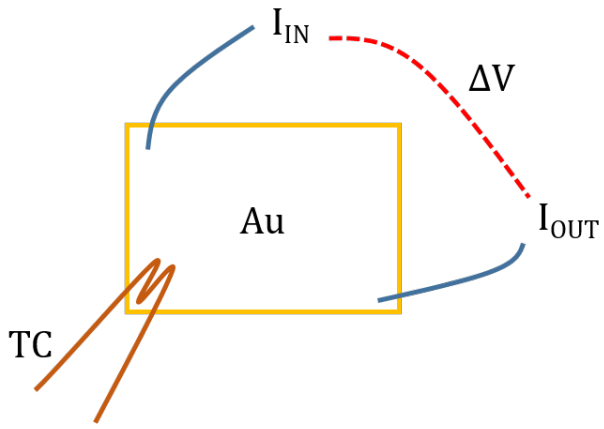

Figure 4.3: Scheme of the two-wire setup. The TC in the corner allows us to directly measure the sample temperature during the heating.

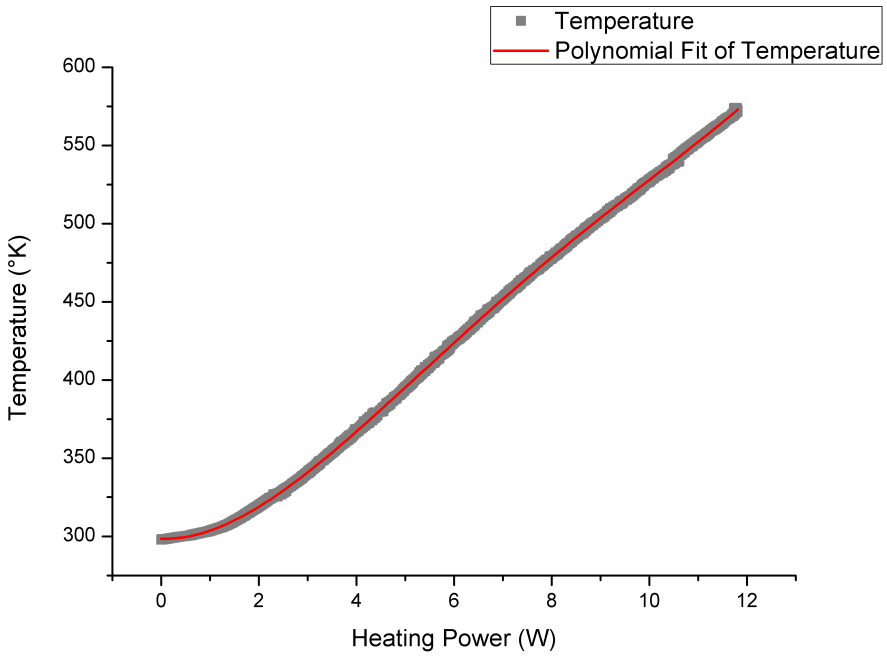

Figure 4.4: Polynomial fit of Temperature (measured by the thermocouple) vs Heating Power.

sample, obtaining the average parameters reported in Table 4.1. Later on we use the same calibration for every sample, because all of them have been obtained cutting the same silicon + silica + gold wafer, and so we can expect the same thermal properties.

Parameter	Value	Error
β_1	-0.887	0.014
β_2	6.771	0.006
β_3	-0.6512	0.0008
β_4	0.02132	0.00004

Table 4.1: Average parameters of the polynomial fit, performed as calibration of the thermometer.

We must keep in mind that the resistance obtained with the two-wire setup is the sum of the sensor resistance and the contact resistance. To avoid measuring the contact resistance we have to use the 4-wire setup. The 2-wire configuration has the only purpose ro relate the heater current to the sample temperature. In fact, utilizing the 4-wire configuration, we lost the thermocouple information (the sample holder has only four contacts).

4.2.2 Four-Wire Measurements

After the Temperature vs Heating Power calibration we can pass to the four-wire setup, in which we substitute the thermocouple with two other contacts as shown in Fig. 4.5. In this setup we supply the sense current by the thermocouple contacts and we read the voltage difference by the other contacts. In this way through the

Figure 4.5: Scheme of the four-wire setup. To avoid the contact resistance the sensing current is supplied through the TC contacts, while the voltage drop is measured by the add contacts (in this way we also avoid the thermovoltage from the TC contacts).

reading contacts does not pass any current and so the resistance obtained is the true sensor resistance (without the contact resistance). Using the add contacts for reading the voltage drop we avoid any thermovoltage which would come from the TC contacts.

After a preliminary degassing of two slower ramps up to 2 A (6.3 W of adsorbed power, which corresponds to $\sim$ 430 K from Fig. 4.4, we always need to degas the sample after a new mounting in air) we perform 5 ramps up to 2.5 A (11.3 W, so $\sim$ 560 K from Fig. 4.4) of 15000 s for the heating and the same time for the cooling with 4000 s of pause before the next ramp. We can convert the heating power supplied to the filament into the estimated temperature of the sensor and then plot the resistance vs the temperature. As shown in Fig. 4.6 there is a linear proportionality, then we can perform a linear fit of the data expecting that the resistance follows the relation:

$$R(T) = R_0 \left[1 + \alpha \left(T - T_0\right)\right] \tag{4.2}$$

The good agreement with the linear fit is the evidence of the reliability of the previous calibration. This is an important results which allows us to use the calibration in the following of the experiment.

The slopes obtained from the fit will correspond to the product $R_0 \cdot \alpha$ and the intercepts will correspond to R_0, where T_0 (the reference temperature) is the room temperature (so $\sim$ 300 K).

For the first sample (**Sample1**) we obtain the parameters listed in Table 4.2 (the average values are the results of the weighted average and the errors are the standard deviations).

Ramp	**Slope**	**Error**	**Intercept**	**Error**	**Adjusted R^2**
1	0.00827	$3{\cdot}10^{-6}$	2.8485	0.0004	0.995
2	0.00866	$2{\cdot}10^{-6}$	3.0010	0.0002	0.999
3	0.00829	$2{\cdot}10^{-6}$	3.0016	0.0002	0.999
4	0.00809	$2{\cdot}10^{-6}$	2.9774	0.0002	0.999
5	0.00779	$2{\cdot}10^{-6}$	2.9693	0.0002	0.999
average	0.0082	0.0003	2.96	0.06	

Table 4.2: Parameters of the linear fit and the weighted average.

From the average parameter we can obtain the average temperature coefficient of resistance for the first sample:

$$\alpha_{sample1} = (2.8 \pm 0.2) \cdot 10^{-3}\ \mathrm{K}^{-1} \tag{4.3}$$

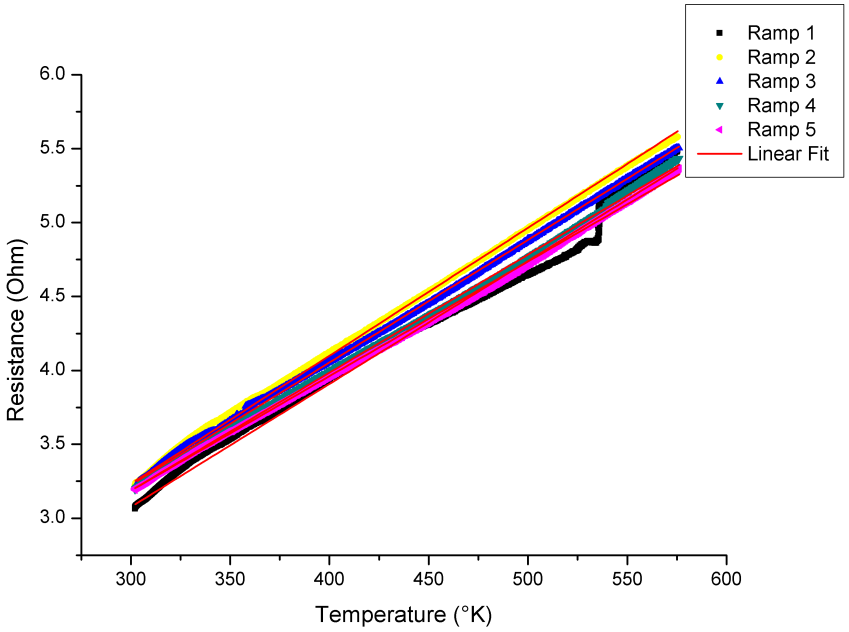

Figure 4.6: Data and linear fit of the ramps.

A second important parameter for calibrating and comparing samples is the Electrical Resistivity (ρ), that is defined as:

$$\rho = \frac{R \cdot A}{l} \tag{4.4}$$

where R is the resistance of the sample, A is the cross-sectional area of the conductor and l is its length. In our case we can obtain the average section from the ratio between the volume of the gold layer and its diagonal length d and we use the same diagonal length as l:

$$\rho = \frac{R_0 \cdot V/d}{d} \tag{4.5}$$

Measuring the dimension of the sample:

$$a = (5.65 \pm 0.01)\ \text{mm}$$
$$b = (5.60 \pm 0.01)\ \text{mm}$$

and knowing that:

$$thickness = (20 \pm 1)\ \text{nm}$$

we can calculate the volume and the diagonal length, and obtain the electrical resistivity:

$$\rho_{sample1} = (3.0 \pm 0.4) \cdot 10^{-8}\ \Omega \cdot \mathrm{m} \tag{4.6}$$

In order to study the repeatability of this calibration we mount a second sample (**Sample2**) in the same sample holder. Because of all our samples come from a large wafer which was then cut in smaller pieces, we expect the same behavior and we use the same temperature vs heating power calibration. After the preliminary degas of the sample we record several heating ramps up to 2.5 A. Then we take out the sample from the UHV chamber and we demount it and mount again in the sample holder and we repeat the measurements, for 3 times. Finally we take some STM images of the sample, we wait for two weeks, leaving the sample in the UHV chamber, and we repeat the measurements.

After plotting data and performing linear fit we obtain the average coefficients shown in Fig. 4.7 and listed in Table 4.3.

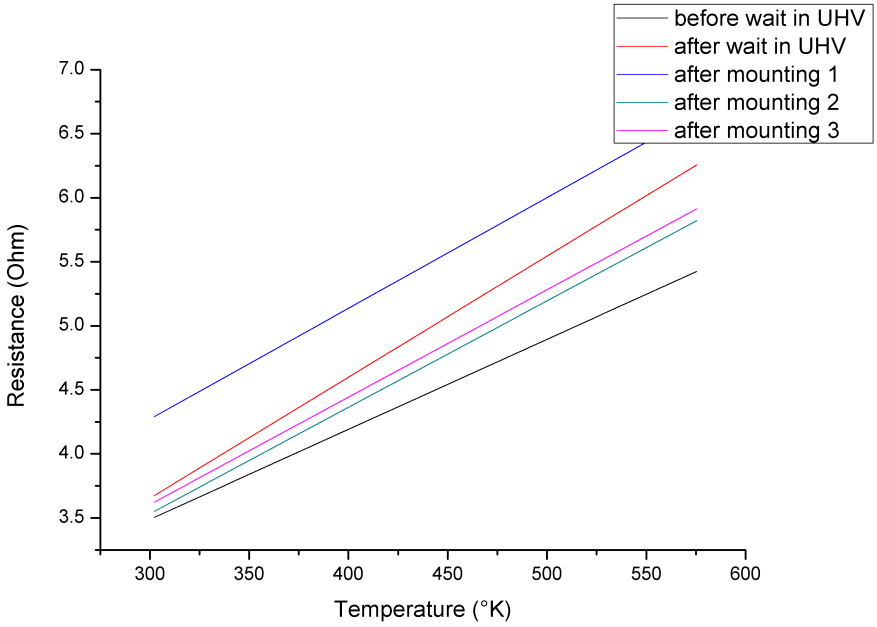

Figure 4.7: Average linear fit of the ramps during the reproducibility test of the thermometer.

From the average parameter we then obtain the average temperature coefficient of resistance for the second sample:

$$\alpha_{sample2} = (2.4 \pm 0.3) \cdot 10^{-3}\ \mathrm{K}^{-1} \tag{4.7}$$

Ramps	α (K^{-1})	**Error** (K^{-1})
before waiting in UHV	$2.1{\cdot}10^{-3}$	$0.7{\cdot}10^{-3}$
after waiting in UHV	$2.8{\cdot}10^{-3}$	$0.4{\cdot}10^{-3}$
after mounting 1	$2.1{\cdot}10^{-3}$	$0.1{\cdot}10^{-3}$
after mounting 2	$2.5{\cdot}10^{-3}$	$0.1{\cdot}10^{-3}$
after mounting 3	$2.5{\cdot}10^{-3}$	$0.1{\cdot}10^{-3}$
average	$2.4{\cdot}10^{-3}$	$0.3{\cdot}10^{-3}$

Table 4.3: Average temperature coefficients of resistance for sample2.

In order to obtain the electrical resistivity we measure the dimensions of the second sample:

$$a = (5.75 \pm 0.01)\ \text{mm}$$
$$b = (5.70 \pm 0.01)\ \text{mm}$$

and knowing that:

$$thickness = (20 \pm 1)\ \text{nm}$$

we obtain:

$$\rho_{sample2} = (3.6 \pm 0.5) \cdot 10^{-8}\ \Omega \cdot \text{m} \tag{4.8}$$

Comparing the average values of α and ρ of Sample1 and Sample2 we see that they correspond within the error range. This is a valuable result, which we will discuss later in section 4.5.

4.2.3 STM Images of the Gold Layer

To complete the analysis of the second sample we take several STM images of different areas of the gold layer. We start with a large scan area of 3x3 μm^2 and then we zoom in, down to 50x50 nm^2. We were able to get stable and reproducible images setting 1.0 V as bias voltage and 1.0 nA as set point current. Below are shown STM images of 500x500 nm^2 (Fig. 4.8(a)) and 100x100 nm^2 (Fig. 4.8(b)) scan area size. It is also shown a section view (Fig. 4.8(c)) taken along the blue line from which we can obtain the surface corrugation of our gold layer, between 1nm and 3 nm. Beside that, an average RMS roughness of (0.8 ± 0.2) nm is measured for the gold surface.

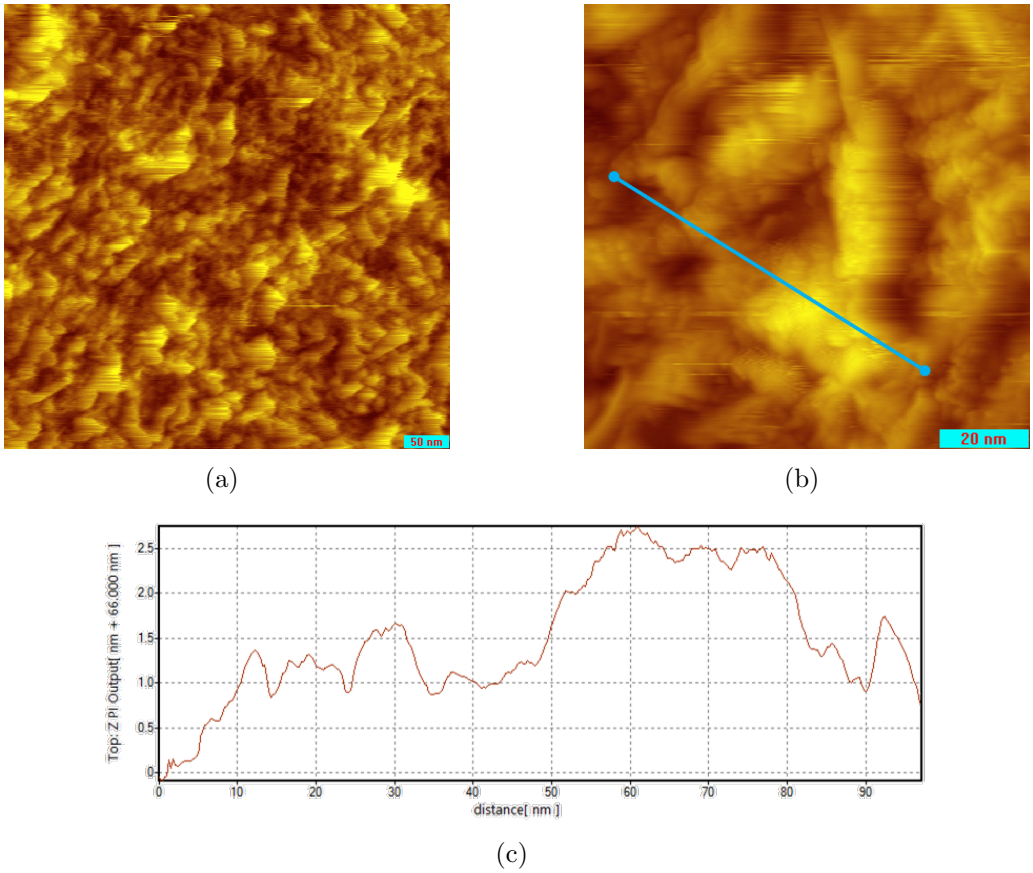

Figure 4.8: (a) STM images of 500x500 nm^2 of the Au layer. (b) STM images of 100x100 nm^2 of the Au layer. (c) Section view taken along the blue line.

4.3 Transfer of Graphene

A high quality monolayer graphene has been grown via chemical vapor deposition (CVD, see [54] for more details) on a copper substrate in a controlled environment and then transferred in the clean room onto six samples similar to the previous two utilized for the thermometer calibration (see Fig. 4.9). We can distinguish the graphene area on the gold sensor because of its different refractive index.

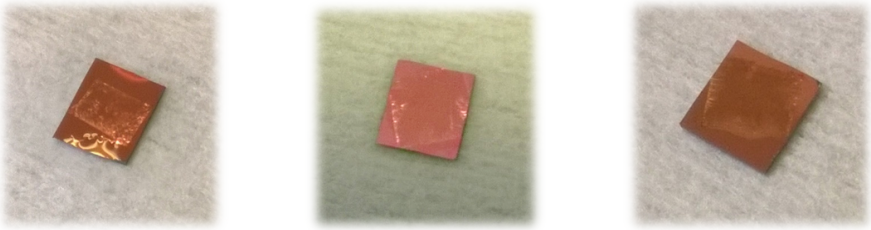

Figure 4.9: Three of the six samples with monolayer graphene on them.

The area dimensions of the graphene sheets are bigger than the hole of the sapphire washer, even if (as shown in the figure) graphene does not cover the entire gold surface. This means that, in the exposure experiments, the titanium is deposited entirely on graphene, and all the subsequent analysis which include Ti and molecular deuterium is restricted to the round surface directly underneath the washer hole.

4.3.1 Raman Spectroscopy of Graphene Layer

One method that allows us to analyze the quality of a monolayer graphene sample is Raman Spectroscopy (as described in Chapter 3).

We perform Raman spectroscopy on SampleG1 and SampleG2, using a 532 nm laser. The scan areas under investigations are 50x50 μm^2, each with 1320 points. Fig. 4.10(b) shows the ratio map, where each pixel reproduce the ratio between the intensity of the $2D$ peak vs the G peak (bright red means high ratio, dark red means low ratio). The intensity of the $2D$ peak (at ~ 2690 cm^{-1}) is (1.7–2.3) times higher than the intensity of the G peak (at ~ 1580 cm^{-1}), as shown in Fig. 4.10(a). Moreover, the average Full Width at Half Maximum (FWHM) of the $2D$ peak is very small:

$$FWHM_{avg} = 40 \text{ cm}^{-1} \tag{4.9}$$

This analysis confirms that the sample is monolayer graphene, because of the higher intensity of the G peak and its small width. Moreover, the absence of

a detectable D peak at $\sim$ 1350 cm^{-1}, connected to the presence of defects on graphene, confirms the high quality of our samples.

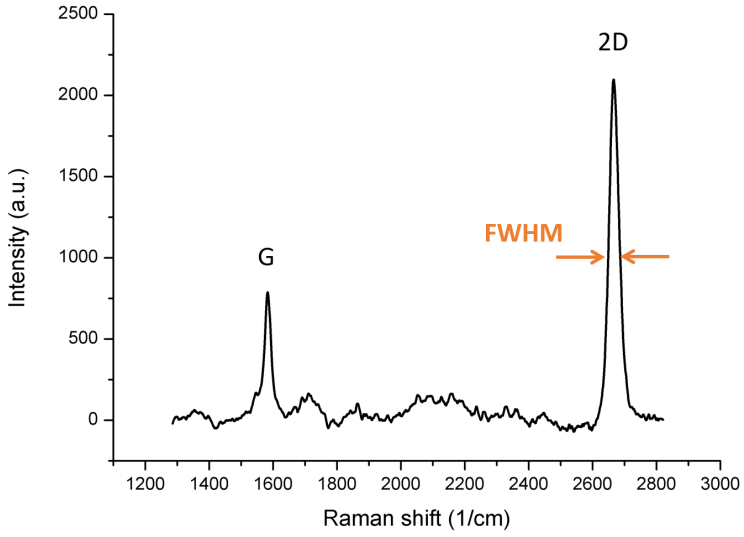

(a)

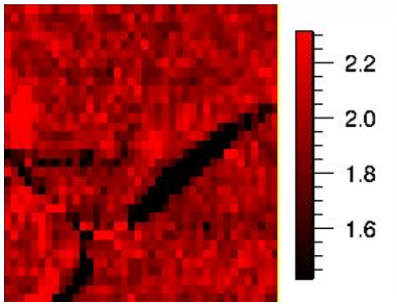

(b)

Figure 4.10: (a) Raman spectra of SampleG2, showing the expected G and $2D$ peaks. (b) Intensity ratio map: each pixel reproduce the ratio between the intensity of the $2D$ peak vs the G peak (bright red means high ratio, dark red means low ratio).

4.3.2 Resistance vs Temperature

After the preliminary degas of the first graphene sample (**SampleG1**) we record several heating ramps up to 2.5 A, with the 4-wire setup. Then we pass to the 2-wire setup with the Wheatstone Bridge (as described in the previous chapter) and we record another heating ramp up to 2.5 A. The resulting temperature coefficients of resistance are listed in Table 4.4. The error on the temperature coefficient of resistance obtained with the Wheatstone bridge setup is comparable with the one on the 2-wire or 4-wire setups. In fact, because these values are obtained heating the sample from room temperature up to ∼300 °C in around 4 hours, the error is mainly originated from the mechanical adjustments of the sample and the contacts, or due to the long term fluctuations of the power supply and the electronics. From Fig. 4.6 we can see as these fluctuations are more important at higher temperature and in the initial ramps of the measurements. On the contrary, the short term noise on the calorimetric measurements produces fluctuations on the signal mainly due to the stability of the measuring setup. As shown in Chapter 5, in this short time, the Wheatstone bridge setup allows a sensitivity much higher than the simple 2-wire or 4-wire setups.

Ramps	α (K^{-1})	**Error** (K^{-1})
4-wire	$2.5{\cdot}10^{-3}$	$0.2{\cdot}10^{-3}$
Wheatstone bridge	$2.6{\cdot}10^{-3}$	$0.2{\cdot}10^{-3}$

Table 4.4: Average temperature coefficients of resistance for SampleG1.

Because the fact that with the Wheatstone bridge setup we perform a 2-probe measurement, we must take into account the contribution of the contacts resistance. In our experiments we have considered this contribution as temperature-independent, and after its evaluation with a preliminary (or subsequent) 4-wire measurement, we have obtained the sensor resistance with a simple subtraction. This approximation would not affect the measure of the small temperature increase during the hydrogenation (of the order of hundredths of Ω), but should be evaluate in the future for a better understanding of our measuring setup. A possible procedure could be the alternate measurements of the sample resistance with 4-wire and Wheatstone bridge setup, after the heating of the sample at several, fixed temperature (from room temperature to 600 K, every 25 or 50 K).

In order to obtain the electrical resistivity we measure the dimensions of the

sample:

$$a = (5.20 \pm 0.01)\ \text{mm}$$
$$b = (6.00 \pm 0.01)\ \text{mm}$$

and assuming the same thickness of (20 ± 1) nm (monolayer graphene does not increase considerably the volume of the sensor) we obtain the values listed in Table 4.5.

	ρ (Ωm)	**Error** (Ωm)
after mounting	$2.9{\cdot}10^{-8}$	$0.4{\cdot}10^{-8}$
after Wheatstone bridge	$2.9{\cdot}10^{-8}$	$0.4{\cdot}10^{-8}$

Table 4.5: Electrical resistivity of the sensor for sampleG1.

We mount a new sample (**SampleG2**) and after the degas we record several heating ramps up to 2.5 A with the previous Wheatstone bridge and after mounting a new, more stable Wheatstone bridge. The resulting temperature coefficients of resistance are listed in Table 4.6.

Ramps	α (K^{-1})	**Error** (K^{-1})
Wheatstone bridge	$3.2{\cdot}10^{-3}$	$0.2{\cdot}10^{-3}$
New Wheatstone bridge	$2.3{\cdot}10^{-3}$	$0.4{\cdot}10^{-3}$

Table 4.6: Average temperature coefficients of resistance for SampleG2.

In order to obtain the electrical resistivity we measure the dimensions of the sample:

$$a = (5.10 \pm 0.01)\ \text{mm}$$
$$b = (5.95 \pm 0.01)\ \text{mm}$$

and assuming the same thickness of (20 ± 1) nm we obtain the values listed in Table 4.7.

	ρ (Ωm)	**Error** (Ωm)
Wheatstone bridge	$2.8{\cdot}10^{-8}$	$0.4{\cdot}10^{-8}$
New Wheatstone bridge	$3.6{\cdot}10^{-8}$	$0.5{\cdot}10^{-8}$

Table 4.7: Electrical resistivity of the sensor for sampleG2.

The differences between the values obtained using the two different Wheatstone bridge setup, and the higher errors on the second one, were not expected. As already explained at the beginning of this chapter, the new setup has a considerable lower short term noise, which allows a much higher sensitivity during the calorimetric measurements. Because of the errors are the standard deviation on the average of several ramps, the higher errors of the new bridge in this calibration can derive from the lower number of ramps performed on the new setup. In fact the initial ramps always show more fluctuations originated by the physical adjustments of the measuring setup with temperature.

We mount the last sample (**SampleG3**) and after the degas we record several heating ramps up to 2.5 A with the new Wheatstone bridge and later with the 4-wire setup. The resulting temperature coefficients of resistance are listed in Table 4.8.

Ramps	$\alpha(\mathrm{K}^{-1})$	**Error** (K^{-1})
Wheatstone bridge	$1.6{\cdot}10^{-3}$	$0.2{\cdot}10^{-3}$
4-wire	$1.8{\cdot}10^{-3}$	$0.2{\cdot}10^{-3}$

Table 4.8: Average temperature coefficients of resistance for sampleG3.

In order to obtain the electrical resistivity we measure the dimensions of the sample:

$$a = (5.35 \pm 0.01)\ \mathrm{mm}$$
$$b = (5.80 \pm 0.01)\ \mathrm{mm}$$

and assuming the same thickness of (20 ± 1) nm we obtain the values listed in Table 4.9.

	ρ (Ωm)	**Error** (Ωm)
Wheatstone bridge	$4.1{\cdot}10^{-8}$	$0.5{\cdot}10^{-8}$
4-wire	$3.6{\cdot}10^{-8}$	$0.5{\cdot}10^{-8}$

Table 4.9: Electrical resistivity of the sensor for SampleG3.

This is the only sample showing a so different value for the temperature coefficient of resistance, while for the others samples the values are comparable within the error ranges. Later in this Chapter these parameters will be compared, and their standard values from literature will be presented.

4.3.3 STM Images of the Graphene Layer

To complete the analysis of the samples we take several STM images of different areas of the graphene surface. We start with a scan area of 3x3 μm^2 and then we zoom in down to 50x50 nm^2. We were able to get stable and reproducible images setting 0.6 V as bias voltage and 0.5 nA as set point current. Below are shown STM images of 500x500 nm^2 (Fig. 4.11(a)) and 100x100 nm^2 (Fig. 4.11(b)) scan area size. It is also shown a section view (Fig. 4.11(c)) taken along the blue line from which we can obtain the corrugation of our graphene surface, between 1 nm and 3 nm. Comparing to the STM images of the gold layer the average corrugation remains similar. An average RMS roughness of (1.7 ± 0.5) nm is measured for the graphene monolayer.

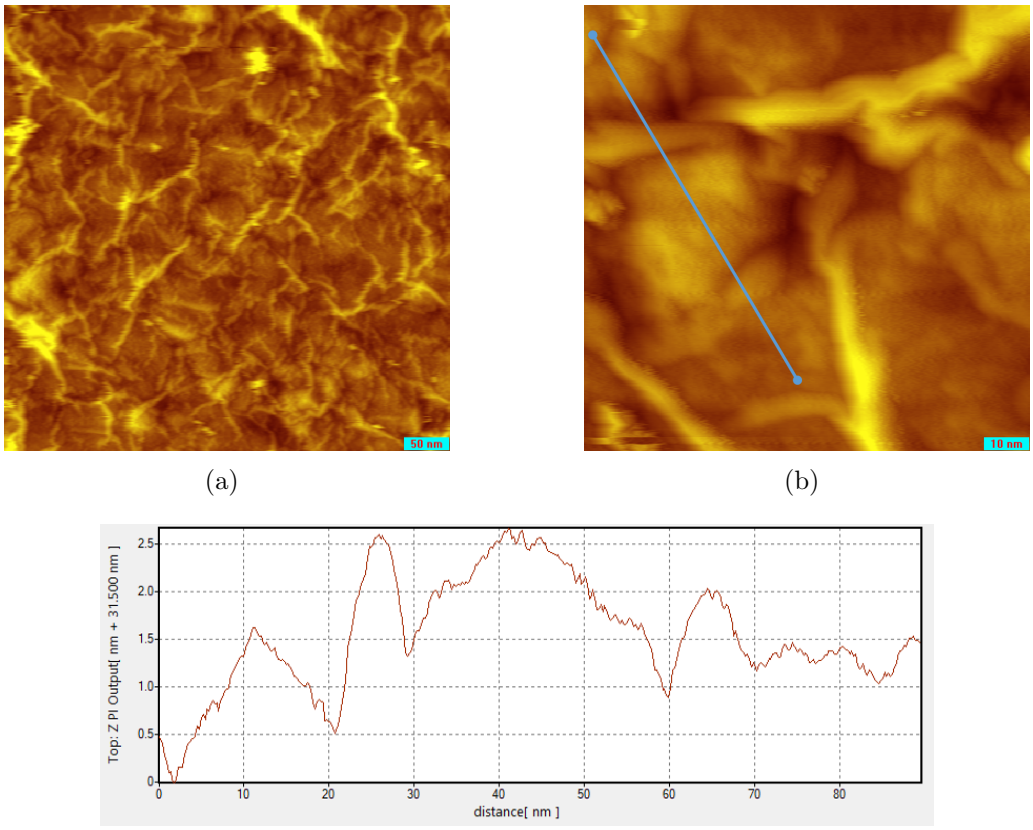

(a) (b)

(c)

Figure 4.11: (a) STM images of 500x500nm^2 of the graphene surface. (b) STM images of 100x100nm^2 of the graphene surface. (c) Section view taken along the blue line.

Besides the surface corrugation, Fig. 4.11(a) also shows the *wrinkles*, typical structures present on graphene on metal substrate after annealing. These wrinkles are believed to form during cool–down after annealing as a result of the difference in thermal expansion coefficients between the graphene monolayer and the gold layer underneath [57]. In our analysis of the wrinkles we measured heights between 2 and 4 nm, and widths between 10 and 20 nm, in good agreement with results from literature (from 2 to 5 nm in height and from 5 to 20 nm in width [58, 59]). The presence of wrinkles explains the higher RMS roughness measured in samples with graphene.

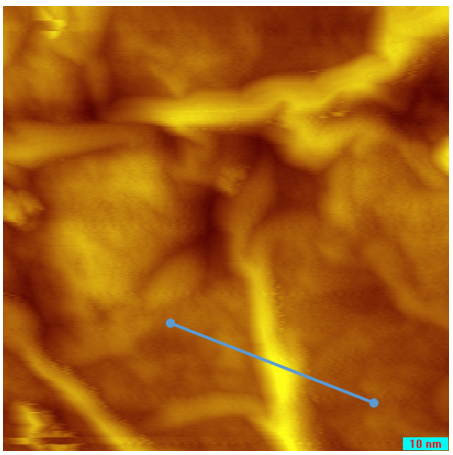

(a)

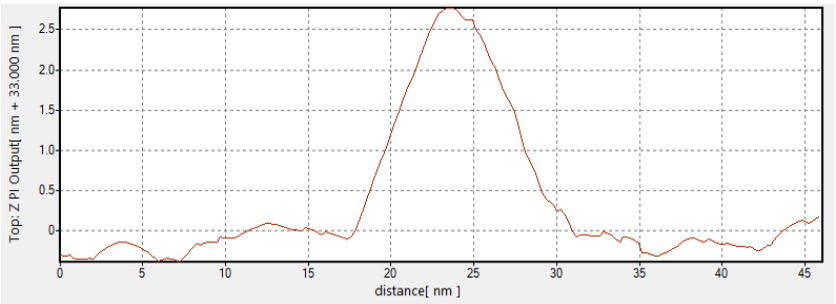

(b)

Figure 4.12: (a) STM images of 100x100nm^2 of the graphene surface. (b) Section view taken on a wrinkle-like structure (along the blue line).

4.4 Titanium on Graphene

In order to functionalize the graphene surface we need to deposit titanium, so first of all we have to calibrate the Ti evaporator. Then we can study the sample with titanium on it and after the exposition to hydrogen (or deuterium), the calorimetric and TDS measurements.

4.4.1 Calibration of Ti Deposition

For the calibration of the titanium evaporator we follow the same procedure used by Mashoff et al. in ref. [26]. First of all we set the same parameters for the Ti evaporator of a their experiment:

$$\begin{aligned} \text{beam voltage} &= 760 \text{ V} \\ \text{beam current} &= 18.40 \text{ mA} \\ \text{filament current} &= 6.2 \text{ A} \end{aligned}$$

and we wait until the flux controller arrives around the set point, then we set it on auto mode that will maintain the flux to the constant value of the set point varying automatically the filament current. In this conditions we perform our calibration by exposing a new, flat graphene on SiC sample to the flux of Ti ions for a time of 10 s, 20 s and 40 s.

After 10 s, 20 s and 40 s of deposition we take STM images (good images with 0.3 V as bias voltage and 0.2 nA as set point current) of the surface and we calculate the volume of Ti deposited on the surface. This analysis is possible because we have a very flat surface as substrate for Ti atoms. In Fig. 4.13 we can see that Ti atoms form small islands on graphene, and assuming a layer distance in the islands as in hexagonal closed packed bulk titanium ($d = 0.2342$ nm, see [26]), we obtain the number of Ti atoms deposited on the surface, in fraction of monolayer (ML) of titanium. From the images we also see that the area coverage of the surface increases but the Ti atoms tend to cluster in bigger islands for longer deposition time intervals (as shown in [26]). For the calibration we take several STM images of 100x100 nm^2 of scan area for the three deposition times (see Fig. 4.13) and we obtain the average values listed in Table 4.10.

We can also fit these values to obtain the flux of Ti, the volume (in ML) of titanium deposited per second, obtaining (see Fig. 4.14):

$$\text{Volume}_{\text{Ti}}(\text{t}) = 0.023 \text{ (ML/s)} \cdot t \tag{4.10}$$

where t is measured in seconds.

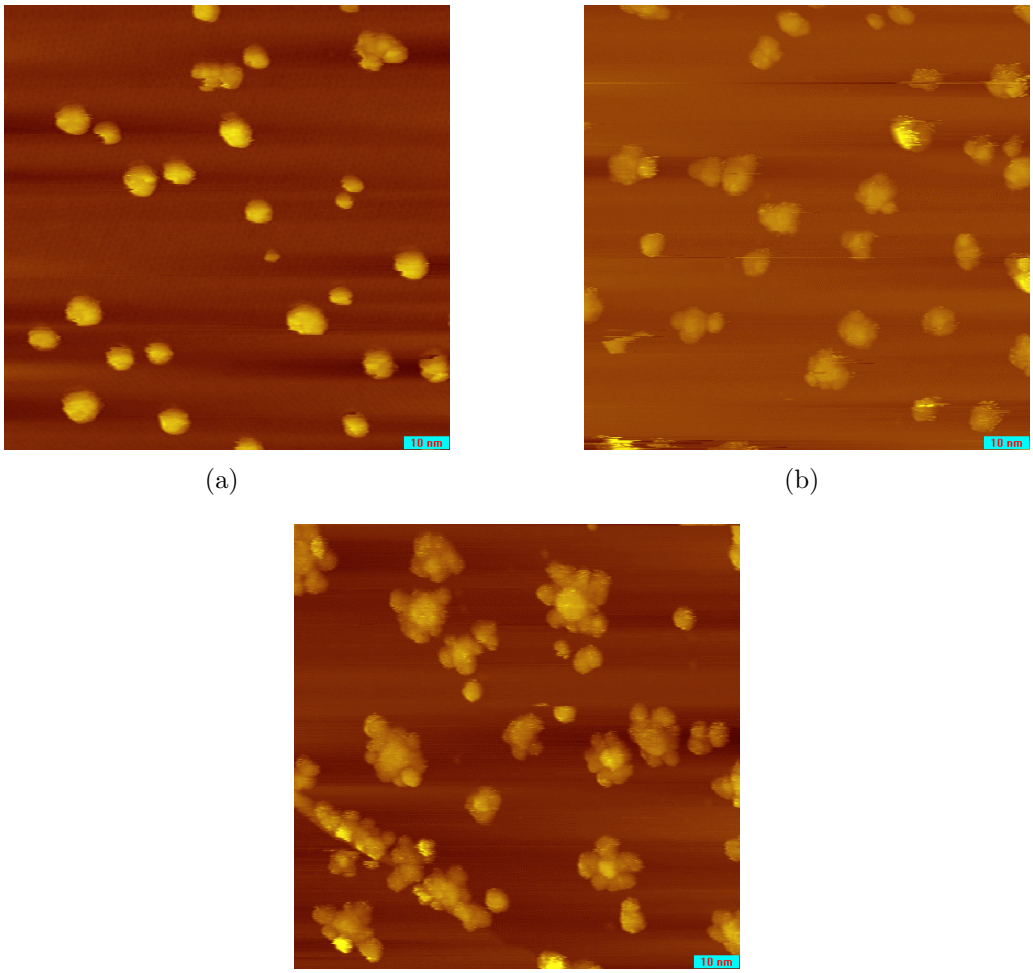

(a) (b)

(c)

Figure 4.13: (a) After 10 s of deposition. (b) After 20 s of deposition. (c) After 40 s of deposition.

Deposition time	Area coverage	Ti deposited
10s	$(8.2 \pm 1.6)\%$	(0.24 ± 0.03)ML
20s	$(14 \pm 3)\%$	(0.45 ± 0.05)ML
40s	$(25 \pm 2)\%$	(0.89 ± 0.10)ML

Table 4.10: Area coverage and amount of Ti deposited.

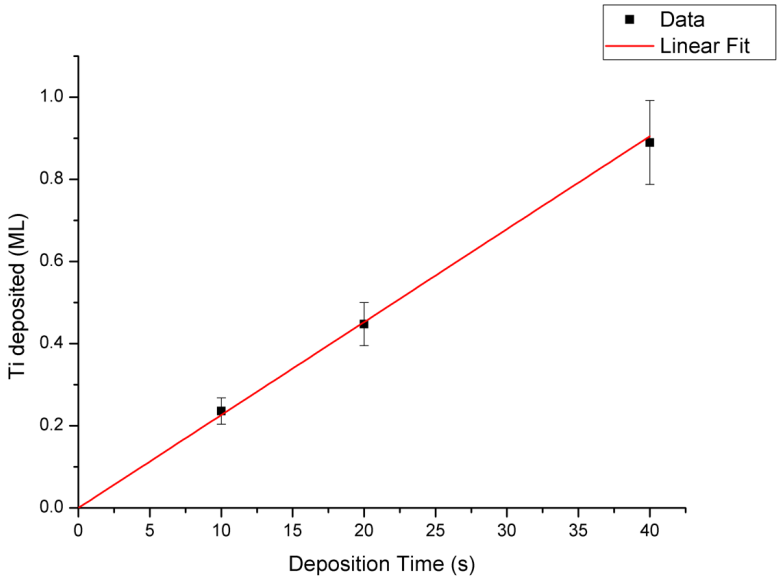

Figure 4.14: Fit of the amount of Ti deposited.

The values of area coverages and the respective fractions of ML of Ti deposited are in good agreement with the results of the previous calibration made my Mashoff et al. In particular they obtained that the deposition of 0.2 ML, 0.55 ML, and 1 ML of Ti correspond to area coverages of 6%, 16%, and 29%. On the contrary, the evaporation time necessary for the deposition of the aforementioned amounts of Ti, is different. In our calibration it is 2 times shorter than in the previous one. This could be due to some modification of the flux controller. The flux controller of the Ti evaporator detect the Ti-ion current during the evaporation. If in the previous experiments some Ti atoms has been adsorbed on the detector surface, and then have later oxidize, the ion current detection could be limited by this thick layer of titanium oxide. This means that, for obtaining the same signal from the ion detector, we need more evaporated Ti. Therefore, notwithstanding the same flux controller value, in our evaporation we have a higher flux of Ti than in the previous one.

4.4.2 Resistance vs Temperature

After the deposition of titanium on the samples and the calorimetric and TDS measurements we record the last heating ramps up to 2.5 A. Because of the reactivity of Ti we have to supply molecular deuterium as soon as possible, in order to avoid the decrease of titanium storage capacity. Therefore we cannot perform

any calibration ramp in the middle of the Ti deposition and the TDS measurement. The resulting temperature coefficients of resistance take into account both the gold sensor and the titanium layer after the desorption of deuterium, so they are different from the coefficient relating to the only sensor (we name them *effective* temperature coefficients of resistance, α_{EFF}). The effective coefficients for the three samples are listed in Table 4.11, together with the amount of Ti deposited on the sensor.

Sample	**deposited Ti** (ML)	α_{EFF} (K^{-1})	**Error** (K^{-1})
G1	13.8	$2.0 \cdot 10^{-3}$	$0.4 \cdot 10^{-3}$
G2	8.4	$1.7 \cdot 10^{-3}$	$0.3 \cdot 10^{-3}$
G3	12.4	$1.8 \cdot 10^{-3}$	$0.2 \cdot 10^{-3}$

Table 4.11: Temperature coefficients of resistance after calorimetric and TDS measurements.

With the same intent we calculate the *effective* electrical resistivity of the samples after the calorimetric and the TDS measurements, that are listed in Table 4.12, together with the amount of Ti deposited on the sensor.

Sample	**deposited Ti** (ML)	$\rho_{EFF}(\Omega m)$	**Error**(Ωm)
G1	13.8	$3.5 \cdot 10^{-8}$	$0.4 \cdot 10^{-8}$
G2	8.4	$3.6 \cdot 10^{-8}$	$0.5 \cdot 10^{-8}$
G3	12.4	$3.6 \cdot 10^{-8}$	$0.5 \cdot 10^{-8}$

Table 4.12: Electrical resistivity after calorimetric and TDS measurements.

The good agreement between the values obtained for the three samples (both α and ρ correspond within the error ranges) is a valuable result. In Section 4.5 we will compare these values with the ones obtained for the samples before Ti deposition.

4.4.3 STM Images of the Ti deposited

To complete the analysis of the samples we take several STM images of different areas of the titanium coverage. In each experiment we have deposited enough

Ti to reach 100% coverage. We start with a scan area of 3x3μm^2 and then we zoom in down to 50x50 nm^2. We were able to get stable and reproducible images setting 0.2 V as bias voltage and 0.09 nA as set point current. Below are shown STM images of 500x500 nm^2 (Fig. 4.15(a)) and 100x100 nm^2 (Fig. 4.15(b)) scan area size. It is also shown a section view (Fig. 4.15(c)) taken along the blue line from which we can obtain the corrugation of our titanium coverage, between 1 nm and 6 nm. An average RMS roughness of (2.0 ± 0.5) nm is measured for the Ti surface. From the STM images is clear that Ti atoms cluster forming a layer of large connected islands.

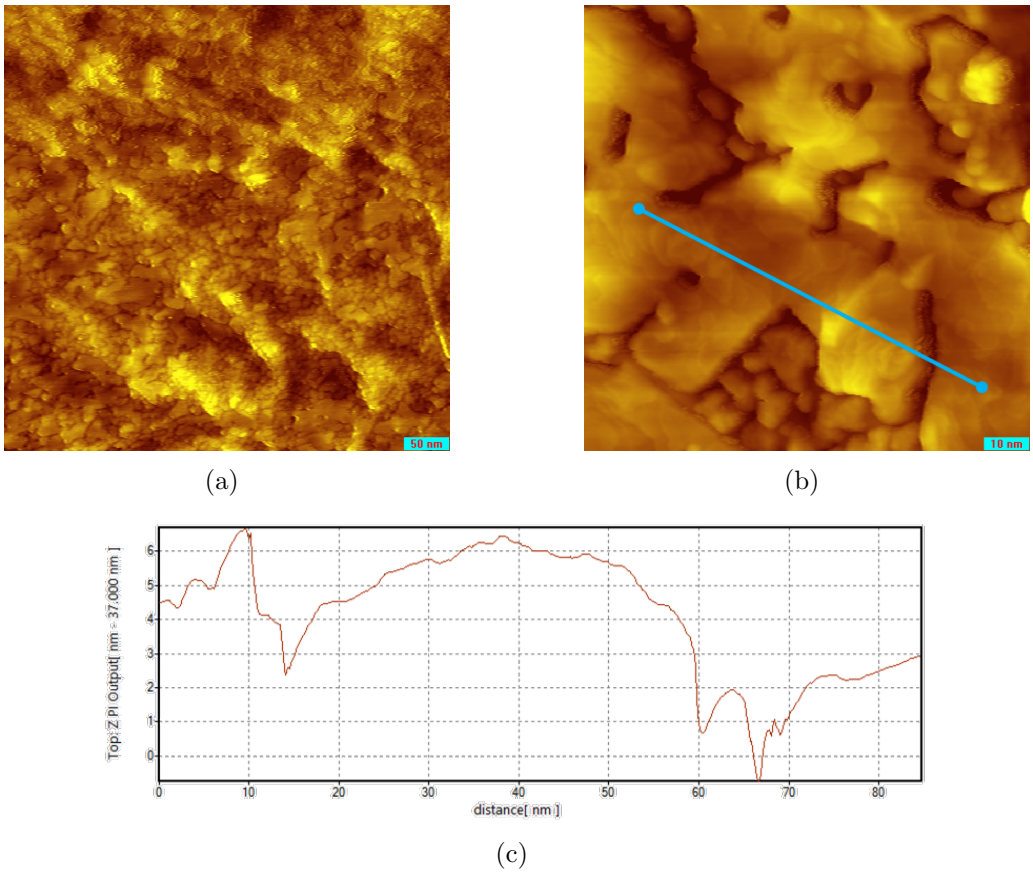

Figure 4.15: (a) STM images of 500x500 nm^2 of the titanium coverage. (b) STM images of 100x100 nm^2 of the titanium coverage. (c) Section view taken along the blue line.

4.5 Comparison of calibration parameters

After the calibration of our samples with only the gold sensor, with the graphene layer and finally with the titanium coverage we can compare the values of the temperature coefficient of resistance and the electrical resistivity, listed in Tables 4.13 and 4.14, together with the weighted average and the values known from literature (see [40]). For a visual comparison they are also plotted in Fig. 4.16.

Sample	α (K^{-1})	α_{EFF} (K^{-1})
1	$(2.8 \pm 0.2) \cdot 10^{-3}$	-
2	$(2.4 \pm 0.3) \cdot 10^{-3}$	-
G1	$(2.6 \pm 0.2) \cdot 10^{-3}$	$(2.0 \pm 0.4) \cdot 10^{-3}$
G2	$(2.8 \pm 0.5) \cdot 10^{-3}$	$(1.7 \pm 0.3) \cdot 10^{-3}$
G3	$(1.7 \pm 0.2) \cdot 10^{-3}$	$(1.8 \pm 0.2) \cdot 10^{-3}$
average (with G3)	$(2.4 \pm 0.4) \cdot 10^{-3}$	$(1.8 \pm 0.3) \cdot 10^{-3}$
(without G3)	$(2.7 \pm 0.1) \cdot 10^{-3}$	
literature	$3.4 \cdot 10^{-3}$	

Table 4.13: Comparison of temperature coefficients of resistance. α is measured for only thermometer + graphene, α_{EFF} is measured for thermometer + graphene + Ti.

Sample	ρ (Ωm)	ρ_{EFF} (Ωm)
1	$(3.0 \pm 0.4) \cdot 10^{-8}$	-
2	$(3.6 \pm 0.5) \cdot 10^{-8}$	-
G1	$(2.9 \pm 0.4) \cdot 10^{-8}$	$(3.5 \pm 0.4) \cdot 10^{-8}$
G2	$(3.2 \pm 0.4) \cdot 10^{-8}$	$(3.6 \pm 0.5) \cdot 10^{-8}$
G3	$(3.7 \pm 0.5) \cdot 10^{-8}$	$(3.6 \pm 0.5) \cdot 10^{-8}$
average	$(3.2 \pm 0.4) \cdot 10^{-8}$	$(3.6 \pm 0.4) \cdot 10^{-8}$
literature	$2.44 \cdot 10^{-8}$	

Table 4.14: Comparison of electrical resistivity. ρ is measured for only thermometer + graphene, ρ_{EFF} is measured for thermometer + graphene + Ti.

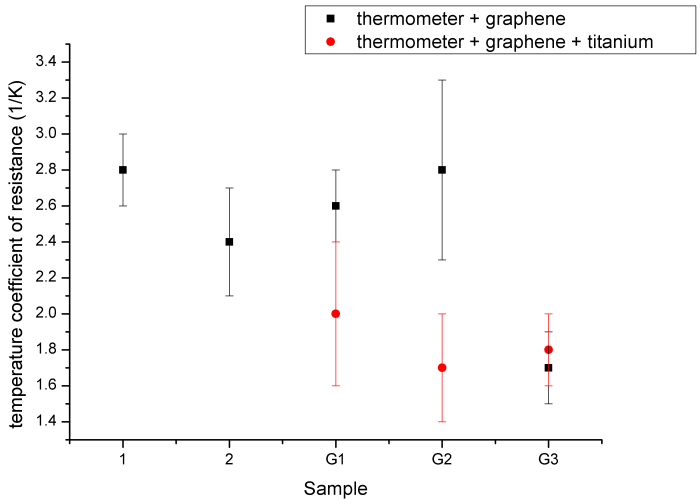

(a)

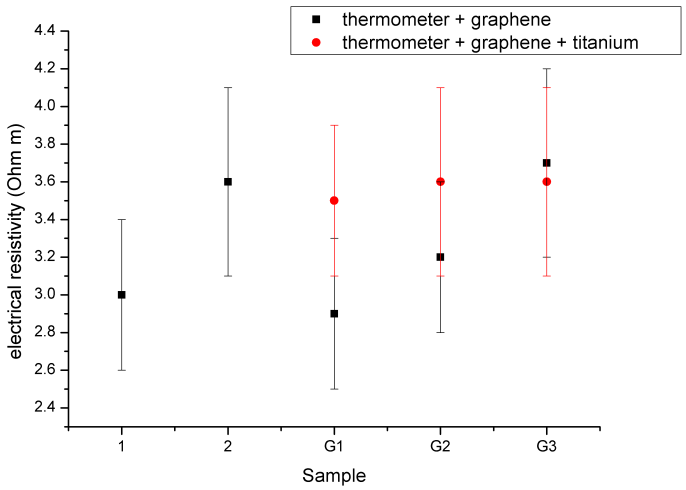

(b)

Figure 4.16: (a) Comparison of α values for the different samples and measurements (black: sample with thermometer + graphene; red: sample with thermometer + graphene + Ti). (b) Comparison of ρ values for the different samples and measurements (black: sample with thermometer + graphene; red: sample with thermometer + graphene + Ti)

The first result of the experiment can be extracted from the comparison of α and ρ of the different samples. We obtain a temperature coefficient of resistance in the range (1.7 - 2.8)·10^{-3} K^{-1} before Ti deposition (five samples), and in the range (1.7 - 2.0)·10^{-3} K^{-1} after Ti deposition (three samples). Except for the α of SampleG3, all the respective values correspond within the error range. Comparing the average values of α (without Ti) and α_{EFF} (with Ti, after adsorption and desorption of D_2) we notice that the latter is smaller. This is due to the Ti layer which introduces a different temperature coefficient of resistance, resulting in a modified α_{EFF}. In particular, considering Ti layer and graphene + gold as two parallel resistances, the resulting coefficient of resistance is lower than the one for only graphene + gold. The discrepancy between the α of SampleG3 and the others could be due to some inhomogeneities of the Ti layer underneath the gold layer, similarly to the ones produced during the evaporation of the additional Ti layer deposited before hydrogenation. In fact, the value for SampleG3 is very close to the values of α_{EFF}, whose change derives from the addition of a new Ti layer.

Regarding the electrical resistivity, we obtain values in the range (2.9 - 3.7)·10^{-8} Ωm before Ti deposition (five samples), and in the range (3.5 - 3.6)·10^{-8} Ωm after Ti deposition (three samples). In this calibration, all the respective values correspond within the error range. This results in a good repeatability of our experiment. Comparing the average values of ρ (without Ti) and ρ_{EFF} (with Ti, after adsorption and desorption of D_2) we notice that the latter seems to be bigger. A possible reason is that the deposited Ti layer introduces additional scattering, also for the presence of a new interface, which results in a slightly major electrical resistivity.

Variations from the standard values of α (3.4·10^{-3} K^{-1} [40]) and ρ (2.44·10^{-8} Ωm [40]) are expected because we are not considering a gold homogeneous layer and an isolated system, but we have a corrugated, sputtered gold layer sandwiched between a Ti layer for proper sticking on the silica underneath, and a second Ti layer evaporated. Moreover, reference values are expectable in case of bulk materials, while in our case, the corrugation or even some superficial scratches, can affect the physical properties of the 20 nm-thin layer of gold.

Despite these variations, experimental values show a good compatibility, resulting in a good repeatability of the experiment.

4.6 Heat Transfer Calibration

In order to describe the heat transfer through the sample, we need to calculate the heat transfer coefficient for the different parts of the sample. In particular we can expect three different behavior: since the SiO_2 layer acts as a thermal insulator, we expect a first and fast thermalization of the upper layers (graphene,

gold, titanium and silica) with the underlying silicon substrate, followed by a slower thermalization of the substrate with the sample holder, and finally a very slow thermalization of our system with the environment. In the time interval of our measurements we can neglect the last (long) thermalization. Moreover we can separate the fast heat losses of the upper layers through the substrate from the subsequent losses toward the sample holder, described by two different heat transfer coefficient.

To extract these parameters, we heat up the sample using a lamp focused on the surface, and the absorption of the optical power increases the temperature of the sample. First of all we illuminate the sample for 3 minutes and we record the cooling of the system, which can be described with the following exponential decay:

$$\Delta T(t) = \Delta T(0) + A_1 \exp\left(-\frac{t}{\tau_1}\right) + A_2 \exp\left(-\frac{t}{\tau_2}\right) + A_3 \exp\left(-\frac{t}{\tau_3}\right) \qquad (4.11)$$

in order to verify the presence of three different characteristic time of decay. As shown in Fig. 4.17 we can fit the data, obtaining:

- $\tau_1 = (3.0 \pm 0.2)$ s
- $\tau_2 = (47 \pm 2)$ s
- $\tau_3 = (475 \pm 5)$ s

Because all our calorimetric measurements will last less than 5 minutes, and we are interested in the heat transfer through the sample, we can focus on the first part of the cooling. Thus, we illuminate the sample for several time intervals, from 10 to 150 seconds, and we record the cooling down, which can be described (without considering the longer thermalization with the environment):

$$\Delta T(t) = \Delta T(0) + A_1 \exp\left(-\frac{t}{\tau_1}\right) + A_2 \exp\left(-\frac{t}{\tau_2}\right) \qquad (4.12)$$

Performing this calibration on **SampleG2** we obtain the characteristic times listed in Table 4.15, where the errors are the standard deviation of the values, and is also shown the weighted average (an example of the cooling data is shown in Fig. 4.18).

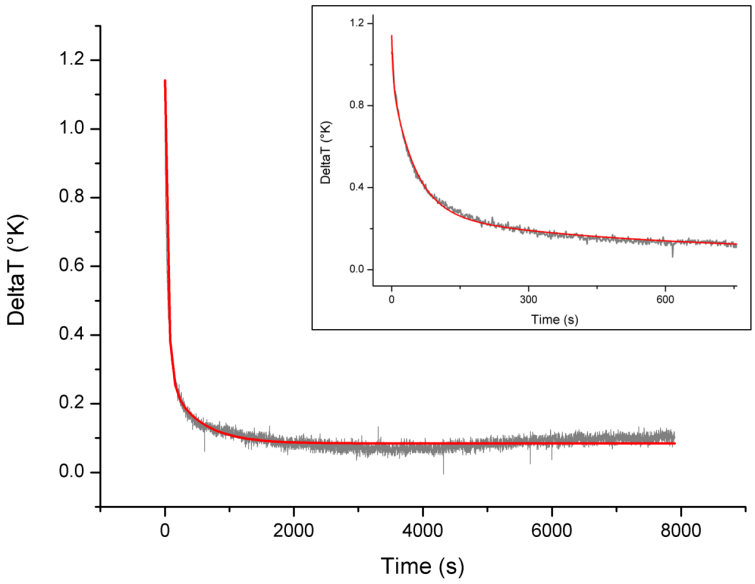

Figure 4.17: Exponential fit (red line) of the cooling of the sample, three different characteristic time are highlighted. The inset is the zoom of the initial part, showing the good agreement of the fit with the data.

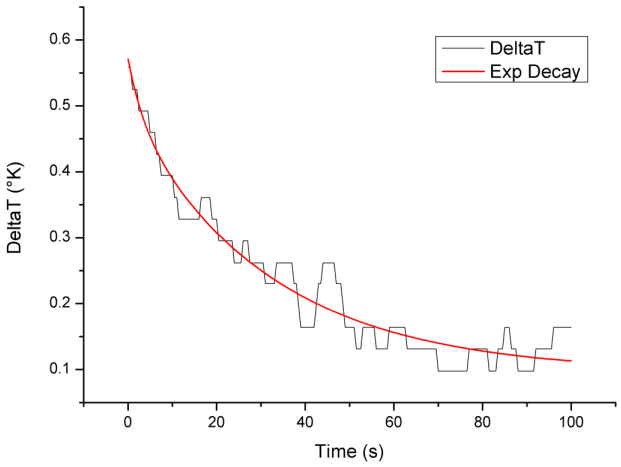

Figure 4.18: Exponential fit of the cooling of SampleG2, after being illuminated for 90 seconds.

Time (s)	τ_1 (s)	**Error** (s)	τ_2 (s)	**Error** (s)
10	36	14	4	5
10	32	6	2.3	1.2
20	31	4	1.0	1.2
20	44	13	4.3	1.9
30	47	6	1.0	1.1
30	32	4	4	2
40	29	2	1.0	1.3
40	44	5	2.2	0.6
60	44	3	3.3	1.2
60	41	2	3.3	1.1
90	32	3	4	2
90	37	3	3.0	1.0
average	37	6	2.8	1.3

Table 4.15: Decay parameters for SampleG2, and weighted average (the error is the standard deviation).

We repeat the same calibration on **SampleG3** and we obtain the characteristic times listed in Table 4.16, in which is also shown the weighted average (an example of the cooling data is shown in Fig. 4.19).

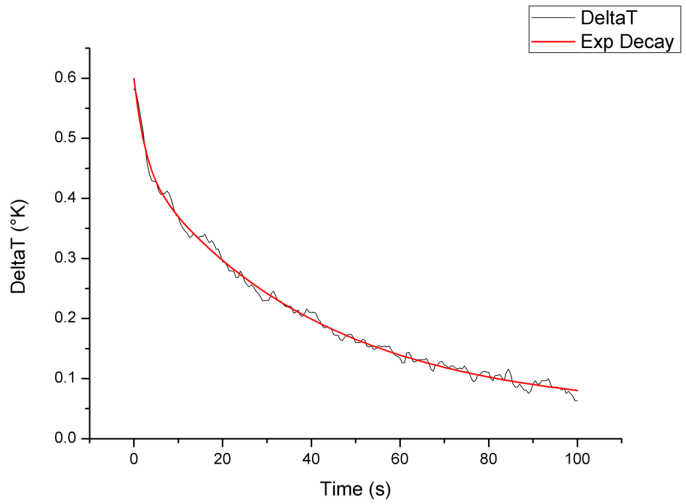

Figure 4.19: Exponential fit of the cooling of SampleG3, after being illuminated for 90 seconds.

Time (s)	τ_1 (s)	**Error** (s)	τ_2 (s)	**Error** (s)
10	35	3	3.0	0.4
10	46	5	3.0	0.4
20	34.5	1.7	2.8	0.4
20	33.0	1.5	2.5	0.4
30	39.0	1.4	3.0	0.3
30	34.6	0.9	2.0	0.2
40	40.6	1.2	2.5	0.2
40	38.4	1.2	2.5	0.3
60	41.2	1.2	3.1	0.3
60	39.0	1.2	3.5	0.3
150	42.8	1.2	4.4	0.5
average	39	4	2.9	0.6

Table 4.16: Decay parameters for SampleG3, and weighted average (the error is the standard deviation). The lower errors derive from the more stable setup.

Comparing the figures, it is clear that the noise is reduced on SampleG3 with respect to SampleG2. As explained in the next Chapter, this has been achieved by using a more stable Wheatstone bridge setup, with low temperature coefficient resistances and a high quality pre-amplifier.

Examining the characteristic times τ_1 and τ_2 for the two samples, we can see that they are in good agreement, within the error range. If we consider also the initial fit with three exponential terms, we notice that τ_1 also correspond, while τ_2 are slightly different, even if their difference still remains below the 10%. In the following analysis we will use the respective characteristic times for each sample.

4.7 Residual Gas Analyzer Calibration

The Residual Gas Analyzer (RGA) is controlled via a LabView program that converts the current reading related to the mass in analysis into the partial pressure of the molecular gas with that mass. Before using the RGA we need to calibrate it, opening the molecular deuterium bottle until in the UHV chamber there is a stable partial pressure of D_2 of around $9 \cdot 10^{-10}$ mbar. In the meanwhile (as shown in Fig. 4.20) we record the reading current of the RGA and we obtain the conversion coefficient:

$$C_{SignalRGA \rightarrow D_2 PartialPressure} = (3.04 \pm 0.06) \cdot 10^{-2} \text{ mbar/A} \tag{4.13}$$

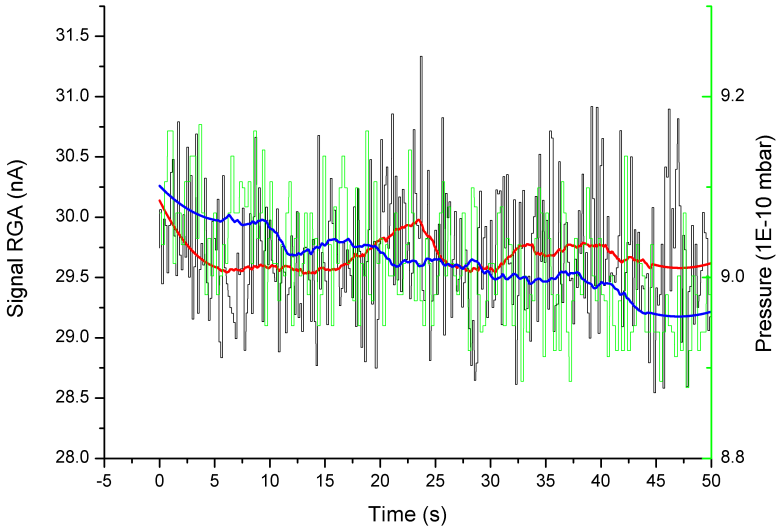

Figure 4.20: Contemporary recording of the partial pressure of D_2 in the chamber and reading current from the RGA.

This conversion coefficient will be later utilized in the LabView software during the TDS measurements, in order to record the partial pressure of D_2 with respect to the sample temperature.

Experimental Results 5

In this chapter are firstly present the results of the blank measurements, which have been done with the purpose of verifying that neither the gold film nor the graphene layer stably adsorb molecular deuterium in the conditions of our experiment. Subsequently, we show the results of the hydrogenation measurements with the 4-wire setup. Finally, we show that the Wheatstone bridge setup allows us to reach a better resolution, and so a very clear signal during the calorimetric measurements is obtained.

5.1 Blank Measurements

In order to verify that deuterium is not adsorbed, in measurable amount, on the gold film, we firstly expose the sample to molecular deuterium. We mount the **Sample2** on the sample holder, using the 4-wire setup, then we transfer it in the preparation chamber and we perform a preliminary degas (slowly, up to ~ 500 K). After that, we wait until the pressure reaches the base pressure of the chamber ($\sim 10^{-10}$ mbar) and we place the sample, on the manipulator, just in front of the gas inlet. Then we carefully open the D_2 bottle in order to have a chamber pressure of $1.0 \cdot 10^{-7}$ mbar. We expose the sample to D_2 for 5 minutes and in the meanwhile we record the sensor resistance. We supply a sensing current of 5 μA, and using the parameters calculated in the previous calibration, we obtain the sensor temperature variation (subtracting the chamber temperature $T_0 = 33.8$ K), as shown in Fig. (5.1). The exposure time has been chosen in order to be sure that almost 1 monolayer of molecular deuterium could be adsorbed on the sample. In fact, 1 *Langmuir* (L), a unit of exposure to a surface used in UHV surface physics, is defined as 10^{-6} Torr s, so it corresponds to a gas exposure of 10^{-6} Torr during 1 second. Assuming a sticking coefficient = 1 (every gas molecule hitting the surface sticks to it), 1 L leads to a coverage of about 1 ML of the adsorbed molecules on the surface [60]. In our experiments we have $7.5 \cdot 10^{-8} \cdot 300$ Torr s

$= 2.25 \cdot 10^{-5} \gg 1$ L. Therefore, 5 minutes of exposure are enough to have 1 ML of adsorbed D_2.

As can be clearly seen, no temperature increase has been detected during the exposure to D_2.

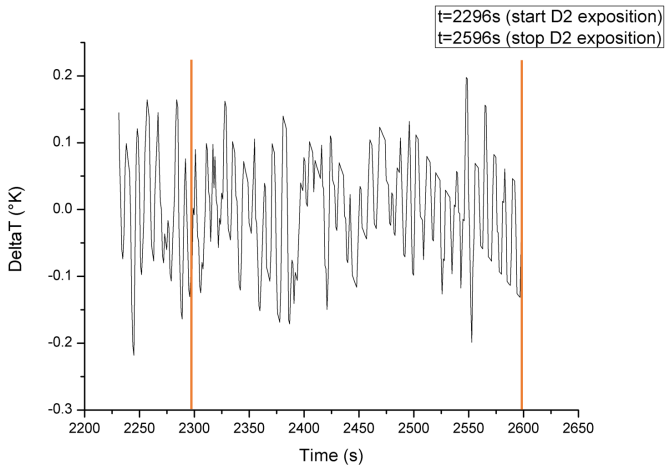

Figure 5.1: Sensor temperature variation during D_2 exposure on the gold film. Blank measurement on Sample2, does not show any temperature increase.

Subsequently, we wait until the pressure goes down to $\sim 5 \cdot 10^{-10}$ mbar and, as a control measurement, we perform a TDS. After placing the sample in front of the RGA, we heat up the sample from room temperature to around 600 K, at an average rate of ~ 0.4 K/s, and we record a TDS spectrum (as shown in Fig. (5.2)).

Besides a little degassing of the sample (which is also seen in the total pressure of the UHV chamber, not only in the selected channel mass=4), no desorption peak was detected. These measurements confirm that stable hydrogen adsorption does not occur on the thin gold film, or other parts, of our sample.

Once we have transferred the graphene monolayer on the gold film, we repeat the blank measurements. We expect that, at room temperature, no stable adsorption of molecular deuterium on graphene would take place. During D_2 exposure at a pressure of $1.0 \cdot 10^{-7}$ mbar, for 5 minutes, we record the sensor temperature. After the chamber pressure has decreased, down to $\sim 5 \cdot 10^{-10}$ mbar, we perform the TDS. The calorimetric measurement does not show any perceivable temperature increase (see Fig. (5.3)), and from the TDS spectrum no desorption peak is detected (see Fig. (5.4)).

These results confirm that, at room temperature, neither gold nor monolayer graphene are able to stably adsorb molecular deuterium.

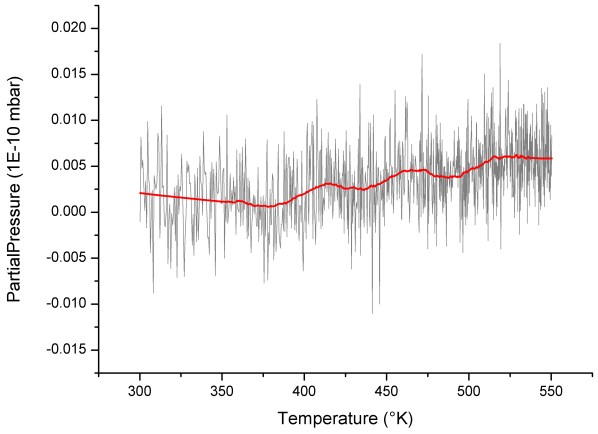

Figure 5.2: TDS spectrum, showing the partial pressure of D_2 (mass=4) vs the sample temperature, after 5 min of D_2 exposure at $P_{D2} = 1.0 \cdot 10^{-7}$ mbar. Blank experiment on Sample2, does not show any desorption peak. (Red line: smoothing)

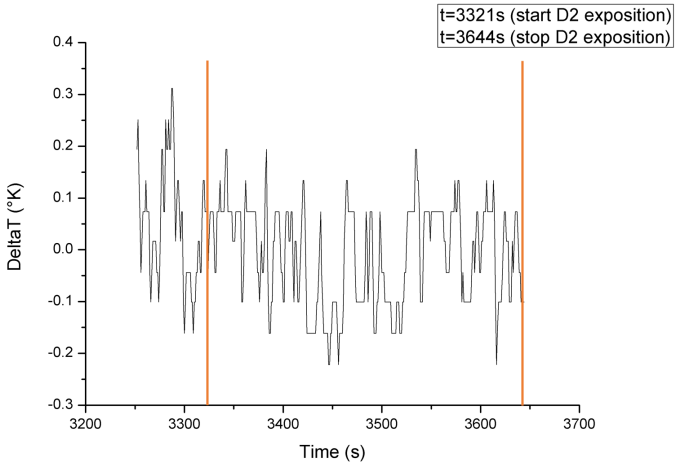

Figure 5.3: Sensor temperature variation during D_2 exposure on the graphene monolayer. Blank measurement on SampleG1, does not show any temperature increase.

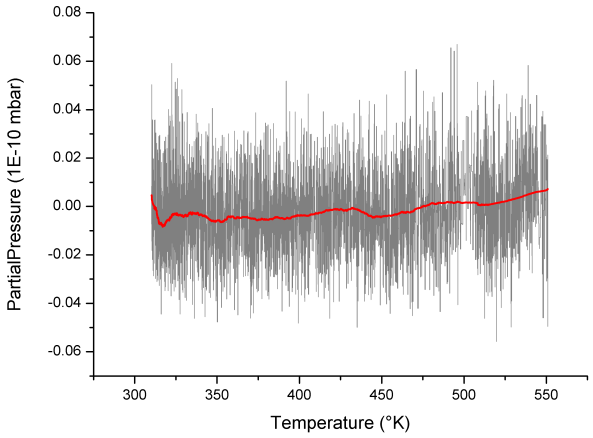

Figure 5.4: TDS spectrum after D_2 exposure, after 5 min of D_2 exposure at $P_{D2} = 1.0 \cdot 10^{-7}$ mbar. Blank experiment on SampleG1, does not show any desorption peak. (Red line: smoothing)

In particular, because the temperature increase during hydrogenation of Ti-decorated graphene should be of the order of (0.05–0.25) K, as we will see later, in this initial calorimetric measurement we do not have the necessary sensitivity for its detection. In fact, as shown in Fig. 5.3, the noise level is of the order of 0.05 K, and the fluctuations are of the order of 0.15 K, so in the same interval range of the possible calorimetric signal. In these conditions the TDS is the reliable measurement which assures us that no molecular deuterium has been stably adsorbed.

5.2 Four-Wire Setup

After the blank measurements, we mount the first sample with graphene on the sample holder, using the 4-wire setup. Because of the heater inside the titanium evaporator, we do not place the manipulator with the sample in front of the evaporator. In such a way we avoid a warming of the sample before the measurement. We turn on the Ti evaporator and we set, as deposition parameters, the same values we used for the calibration:

- beam voltage = 760 V
- beam current = 18 mA
- filament current = 6 A
- flux controller = 20

then we set the controller in *auto* mode and we wait until the value shown on the flux screen is stably 20. This ensures us to work in the same conditions of titanium deposition of the previous calibration. Before starting the deposition we wait until the pressure in the chamber, which has increased because of the degassing of the evaporator, reaches again a value of $\sim 5 \cdot 10^{-10}$ mbar. We place the sample stage in front of the evaporator, but rotated by 90°, so we can carefully adjust the x,y,z alignment of the manipulator without heating the sample. When we are in the same position of the calibration, we rotate the sample in front of the evaporator and we open the shutter. In order to have the highest possible adsorption we need to deposit an amount of titanium which corresponds to 100% coverage ($\sim$ 6.5 ML, from ref. [26]), or more. So, we deposit Ti for 677 seconds, which corresponds to 15.6 ML of titanium. We deposited an higher quantity of Ti than what needed in the experiments, because we initially utilized a different calibration of the titanium evaporator, which was later discovered being incorrect (it underestimated the amount of deposited Ti). The thicker Ti layer deposited on the graphene would increase the quantity of deuterium adsorption (through bulk absorption), but at the same time it would increase the heat capacity of the sensor. The former phenomenon would cause an higher calorimetric signal, whereas the latter would decrease the heat transferred to the thermometer and therefore generate a reduction of the thermometric measure. Even though these two effects affected the measurements, after a careful revision of the experimental setup, we were able to get a clear calorimetric signal (as will be shown in the next section).

In Fig. 5.5 is shown the sensor resistance variation during the Ti deposition. As we open the shutter, the resistance increases because of the heating of the sample

in front of the evaporator heater. Subsequently another effect becomes dominant: the Ti layer is acting as an additional resistance in parallel to the sensor, so the effective resultant resistance is decreasing while more Ti is being deposited on the sample. As we close the shutter and we rotate the manipulator of 90°, the sensor begins to thermalize and the resistance slowly decreases.

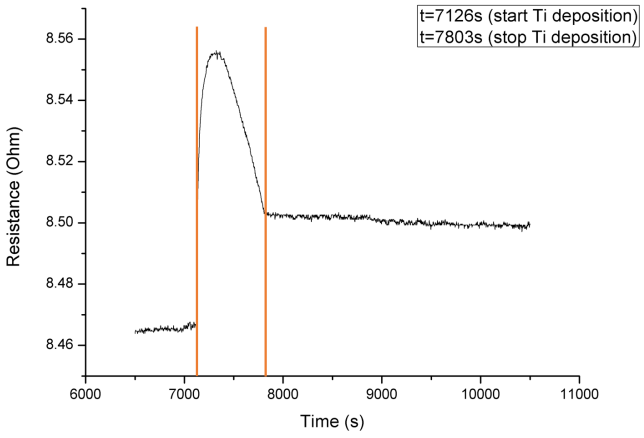

Figure 5.5: Sensor resistance variation during Ti deposition (for 677 seconds, 15.6 ML of Ti) on SampleG1.

Titanium is a very active element, therefore it would oxidate quite fast, in few hours, even in a UHV environment. Because of that we cannot wait for the complete thermalization of the sample, but we have to expose it to molecular deuterium as fast as possible. Therefore, we place the sample in front of the D_2 valve and wait for 20 minutes after the Ti deposition. We carefully open the valve in order to have a chamber pressure of $1.0 \cdot 10^{-7}$ mbar and we expose the sample to D_2 for 5 minutes, while recording the sensor resistance. After subtracting the thermalization trend, we obtain the sensor temperature variation, as shown in Fig. 5.6. Within the sensitivity of the measure setup, no temperature increase is detected during the hydrogenation. In the figure are highlighted both the noise level of the measured signal, and the fluctuations due to the thermal variation of the environment temperature.

In order to verify that molecular deuterium was actually adsorbed on titanium decorated graphene, we perform a TDS measurement. We place the sample in front of the RGA and heat it from room temperature up to around 600 K, while recording the TDS spectrum (shown in Fig. 5.7). A clear desorption peak is detected at $T_p = (464 \pm 3)$ K.

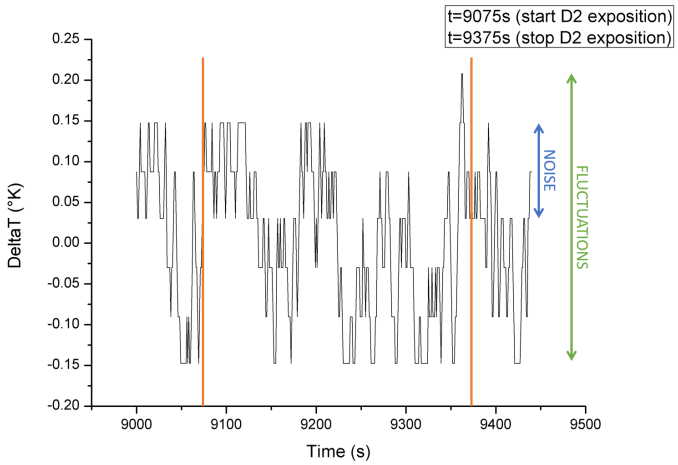

Figure 5.6: Sensor temperature variation during D_2 exposure on the Ti layer, on sampleG1. No temperature increase is detected. Blue arrow: noise level; green arrow: thermal fluctuations.

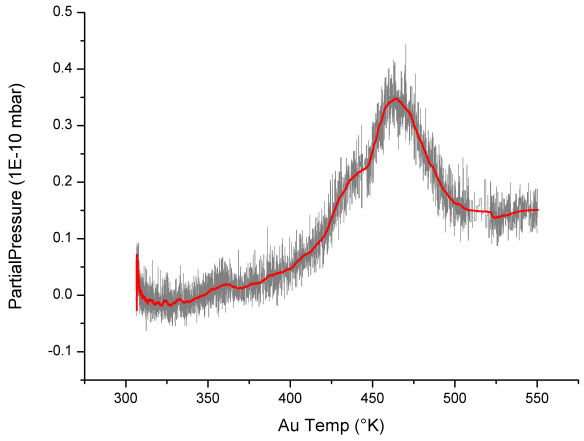

Figure 5.7: TDS spectrum of SampleG1 after 5 min of D_2 exposure at $P_{D2} = 1.0{\cdot}10^{-7}$ mbarD_2. It shows a clear desorption peak at 464 K. (Red line: smoothing)

The desorption measurement shows that deuterium was adsorbed on titanium, which means that the calorimetric signal was below the noise level of our experimental setup, so we need a better sensitivity for the next experiments.

5.2.1 Sample G1

First of all we repeat the measurement with another sample (**SampleG1**), which we mount using the 4-wire setup. After the proper calibration, we deposit Ti on the graphene monolayer for 360 seconds (8.3 ML of deposited Ti) and we wait 26 minutes for the thermalization of the sample. Unfortunately, the subsequently calorimetric measurement was disturbed by an unexpected electrical noise, which prevented us from any thermal detection. Because of that, after a complete degas of the sample, which clearly showed a deuterium desorption, we repeat again the measurement, with the same sample.

We deposit a second layer of Ti, for 446 s (10.3 ML of Ti, as shown in Fig. 5.8(a)), and we wait 10 minutes for the sample thermalization. Then we expose the sample to D_2 for 5 minutes at a pressure of $1.0 \cdot 10^{-7}$ mbar, while recording the sensor resistance. After subtracting the thermalization trend, we obtain the sensor temperature variation, as shown in Fig. 5.8(b). Again, no temperature increase is detected during the exposure to D_2.

After that, we perform the TDS measurement. We place the sample in front of the RGA and we heat it from room temperature up to around 600 K, while recording the TDS spectrum (shown in Fig. 5.8(c)). A clear desorption peak is detected at $T_p = (443 \pm 3)$ K.

In conclusion, after two samples measured, it is clear that in order to detect the temperature increase due to the heat transfer from the Ti layer to the gold sensor, we need a better sensitivity of the experimental setup. For this reason we moved to a Wheatstone bridge setup.

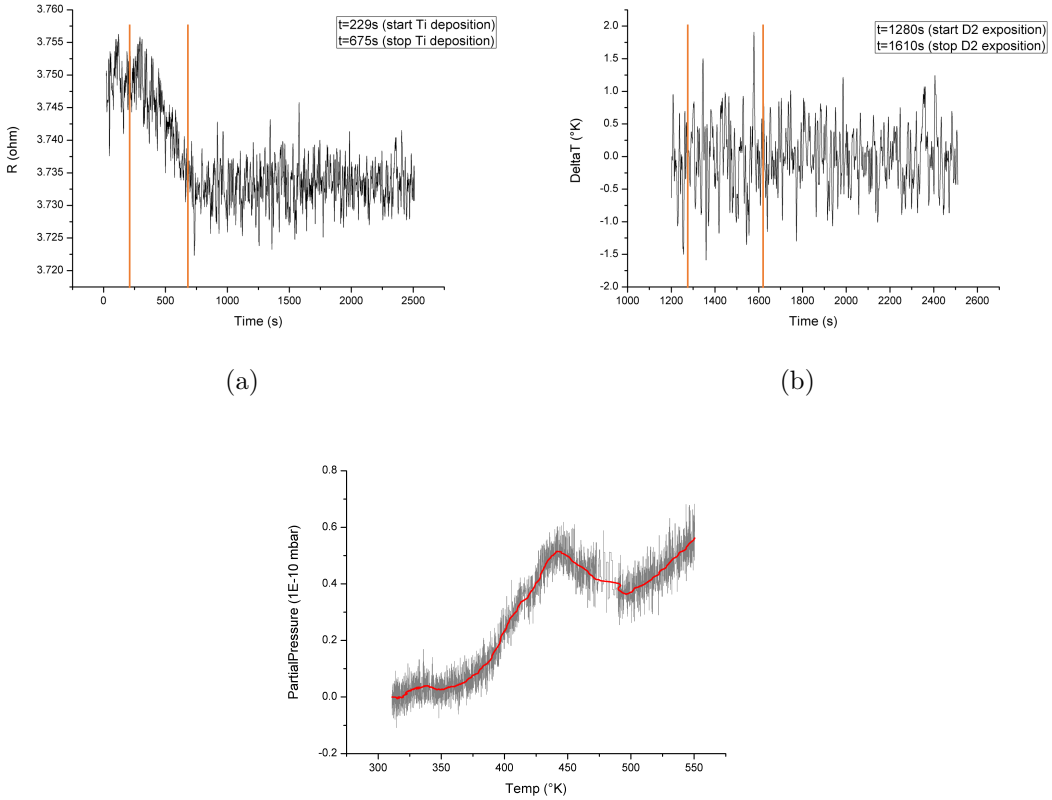

Figure 5.8: (a) Sensor resistance variation during the second Ti deposition (for 446 s, 10.3 ML of Ti) on SampleG1. (b) Sensor temperature variation during D_2 exposure on the Ti layer. No temperature increase is detected. (c) TDS spectrum of SampleG1 after 5 min of D_2 exposure at $P_{D2} = 1.0 \cdot 10^{-7}$ mbarD_2. It shows a clear desorption peak at 443 K. (Red line: smoothing)

5.3 Wheatstone Bridge Setup

We prepare the Wheatstone bridge setup, as shown in Fig. 5.9, with $R_1 \approx R_2 \approx 1$ KΩ and $R_3 \approx R_{sample}$. We set the output of the Lock-In Amplifier at 0.100 V, so the sensing current is in the order of 100 μA. In order to work with the best sensitivity of the LIA, we equilibrate the bridge, varying R_3 until the input signal, read with the LIA, is as low as possible. In our initial conditions we achieve to have an output signal of 264.1 μV, with $R_3 = 2.6$ Ω.

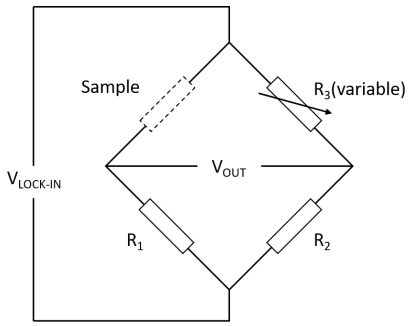

Figure 5.9: First Wheatstone bridge setup, with $R_1 \approx R_2 \approx 1$KΩ, $R_3 \approx R_{sample}$, $V_{LIA} =$ 0.100 V.

We repeat the measure procedure, by depositing Ti for 600 s (on the same SampleG1, a third layer of 13.8 ML of Ti, as shown in Fig. 5.10(a)) and afterwards we wait for 12 minutes for the thermalization of the sample. Then we expose the sample to D_2 for 5 minutes at a pressure of $1.0 \cdot 10^{-7}$ mbar, while recording the sensor resistance. After subtracting the thermalization trend, we obtain the sensor temperature variation, as shown in Fig. 5.10(b). Performing a data smoothing (red line in the figure), we can slightly catch a temperature increase in the time interval of the deuterium exposure.

After that, we perform the TDS measurement. We place the sample in front of the RGA and we heat it from room temperature up to around 600 K, while recording the TDS spectrum (shown in Fig. 5.10(c)). A clear desorption peak is detected at $T_p = (422 \pm 4)$ K.

In order to further improve the measure setup, we mounted a new Wheatstone bridge, with low temperature coefficient resistances, for reducing the signal fluctuations. We measured the exact values of the new resistances and we obtained: $R_1 = 996.85$ Ω and $R_2 = 998.06$ Ω. In addition we amplified and filtered the input signal using a low-noise voltage Pre-Amplifier (by Stanford Research Systems) with a gain factor of 10 and very high quality filters. Because the frequency of our LIA output is set at 17 Hz, we can use the *High Pass* filter at 10 Hz (with

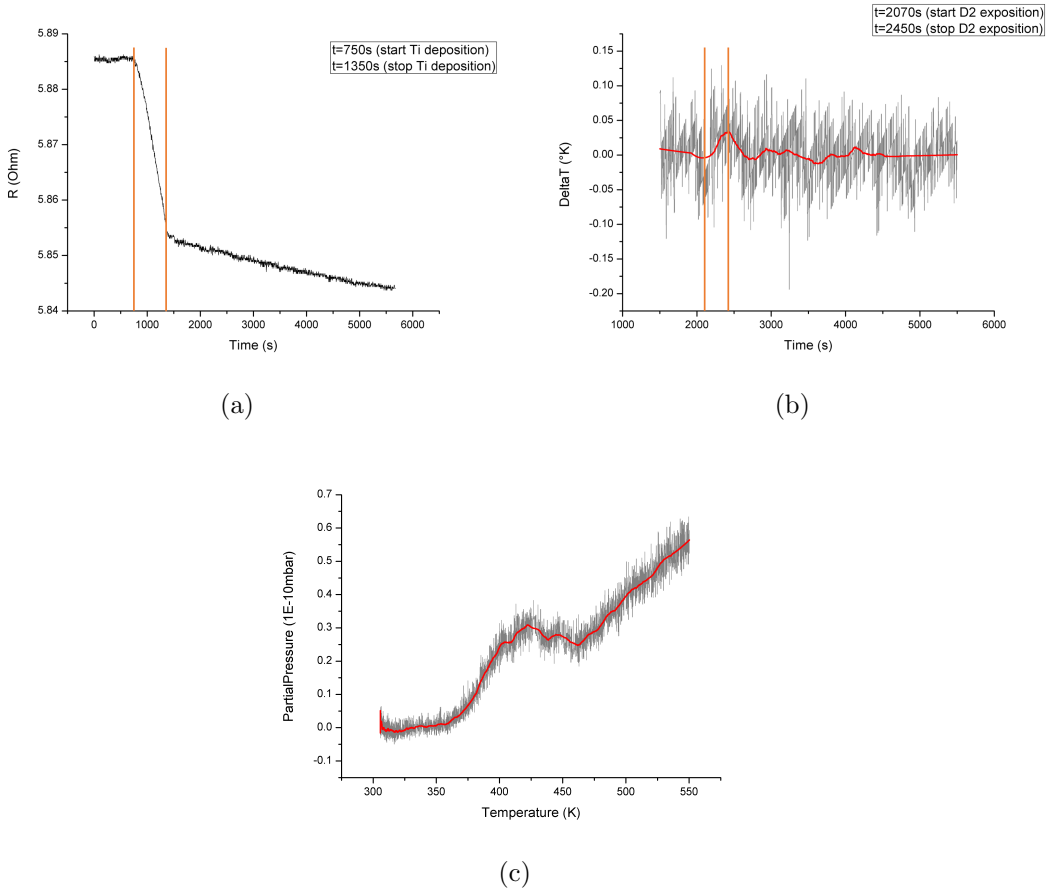

Figure 5.10: (a) Sensor resistance variation during the third Ti deposition (for 600 s, 13.8 ML of Ti) on SampleG1. (b) Sensor temperature variation during D_2 exposure on the Ti layer. (Red line: smoothing) A slightly detection of the temperature increase is achieved. (c) TDS spectrum of SampleG1 after 5 min of D_2 exposure at $P_{D2} = 1.0 \cdot 10^{-7}$ mbarD_2. It shows a clear desorption peak at 422 K. (Red line: smoothing)

a suppression of 6 dB) and the *Low Pass* filter at 30 Hz (with a suppression of 6 dB). In Fig. 5.11 is clearly shown the noise reduction achieved by using the new experimental setup, tested by illuminating the sensor with a lamp and recording the resistance variation due to the optical power absorption.

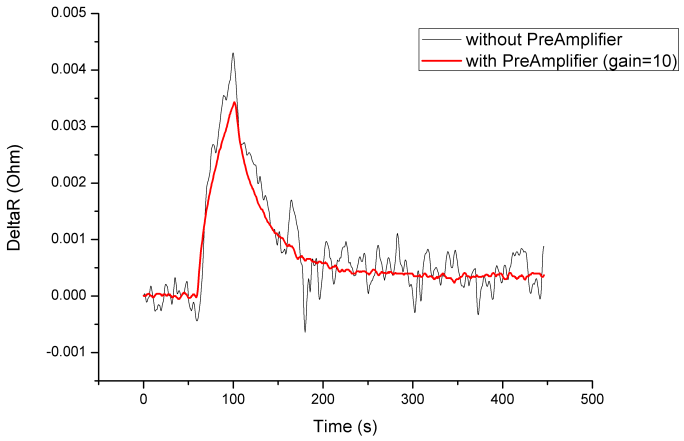

Figure 5.11: Comparison between the input signal with and without the use of the low-noise voltage Pre-Amplifier (with a gain factor of 10).

5.3.1 Sample G2

We mount a new, clean sample (**SampleG2**), and after the calibration, we are ready to repeat the experiment. We firstly equilibrated the bridge in order to work at the lowest input signal possible, and we measured $R_3 = 6.94\ \Omega$. Then, we controlled that even with a LIA output of 0.100 V or 0.200 V, no self-heating of the sensor occurred because of the sensing current ($\sim 100\ \mu$A or $\sim 200\ \mu$A), which is flowing through the gold layer. Moreover, we tested different settings for the LIA and the Pre-Amplifier, finding that the clearest signal is measured with $V_{LIA} = 0.200$ V as output, and 200 mV as full-scale for the LIA input. In the best setting conditions, we degassed the sample two times, recording the TDS spectra (shown in Fig. 5.12), from which we can be sure that no further desorption of impurities (with molecular mass = 4) will occur during the TDS measurement subsequent to the hydrogenation (in the temperature range of interest).

After the complete thermalization of the sample, we deposit Ti for 365 s (8.4 ML of Ti, as shown in Fig. 5.13(a)) and afterwards we wait 10 minutes for the thermalization of the sample. Then we expose the sample to D_2 for 5 minutes

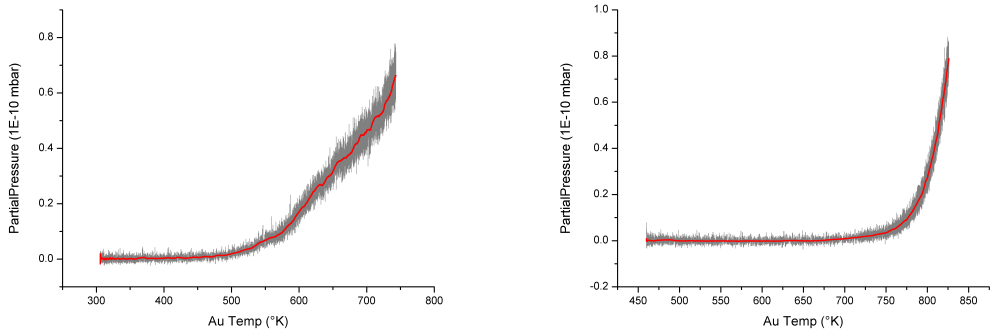

(a) (b)

Figure 5.12: (a) First degas of the SampleG2, showing a desorption of impurities starting from around 500 K. (b) Second degas of the SampleG2, showing a desorption of impurities starting from around 750 K.

at a pressure of $1.0 \cdot 10^{-7}$ mbar, while recording the sensor resistance. After subtracting the thermalization trend, we obtain the sensor temperature variation, as shown in Fig. 5.13(c). An increase in the sensor temperature is clearly detected ($\Delta T \approx 0.045$ K).

After that, we perform the TDS measurement. We place the sample in front of the RGA and we heat it from room temperature to around 600 K, while recording the TDS spectrum (shown in Fig. 5.13(d)). A clear desorption peak is detected at $T_p = (465 \pm 3)$ K.

A critical point, for this analysis, is the exponential fitting of the thermalization trend. In fact, depending on the sample, if it was the first or the second measurement, and depending on the time we waited before the exposure to deuterium, the cooling down was slightly different. For that reason, we had to be very careful when fitting the temperature decreasing trend.

Because of that, we restrict the evaluation of the calorimetric signal to the rising part (while the sample is heated by the heat release during the deuterium exposure), because its thermalization part depends more significantly from the thermalization trend of the entire system, which has a characteristic time much longer than the hydrogenation time.

We repeat the same procedure a second time, with the same sample. We deposit again Ti for 719 s (a second layer of 16.5 ML of Ti, as shown in Fig. 5.14(a)) and afterwards we wait 16 minutes for the thermalization of the sample. Then we expose the sample to D_2 for 5 minutes at a pressure of $1.0 \cdot 10^{-7}$ mbar, while recording the sensor resistance. After subtracting the thermalization trend, we obtain the sensor temperature variation, as shown in Fig. 5.14(c). An increase

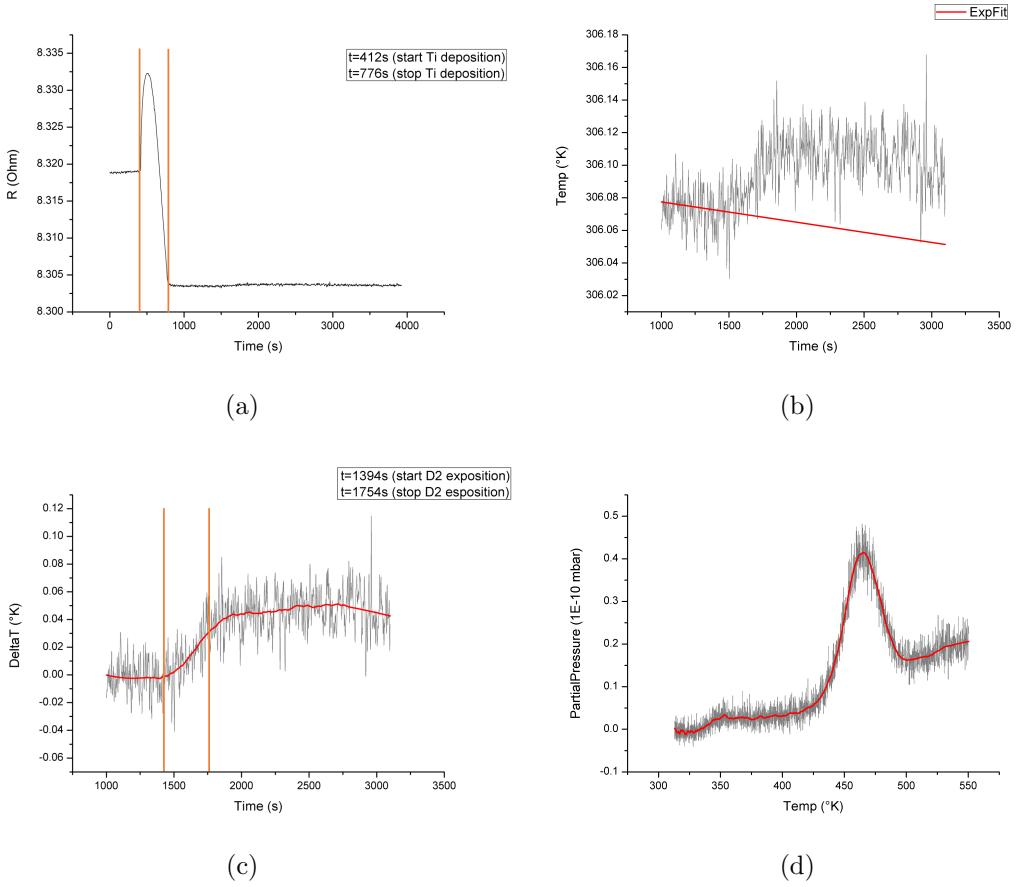

Figure 5.13: (a) Sensor resistance variation during the first Ti deposition (for 365 s, 8.4 ML of Ti) on SampleG2. (b) Sensor temperature variation, showing the increase due to the adsorption process (red line: exponential fit of the thermalization trend), in the second measurement performed with SampleG2. (c) Sensor temperature variation during D_2 exposure on the Ti layer. (Red line: smoothing) A $\Delta T \approx 0.045$ K is clearly detected. (d) TDS spectrum of SampleG2 after 5 min of D_2 exposure at $P_{D2} = 1.0 \cdot 10^{-7}$ mbarD_2. It shows a clear desorption peak at 465 K. (Red line: smoothing)

in the sensor temperature is clearly detected ($\Delta T \approx 0.10$ K).

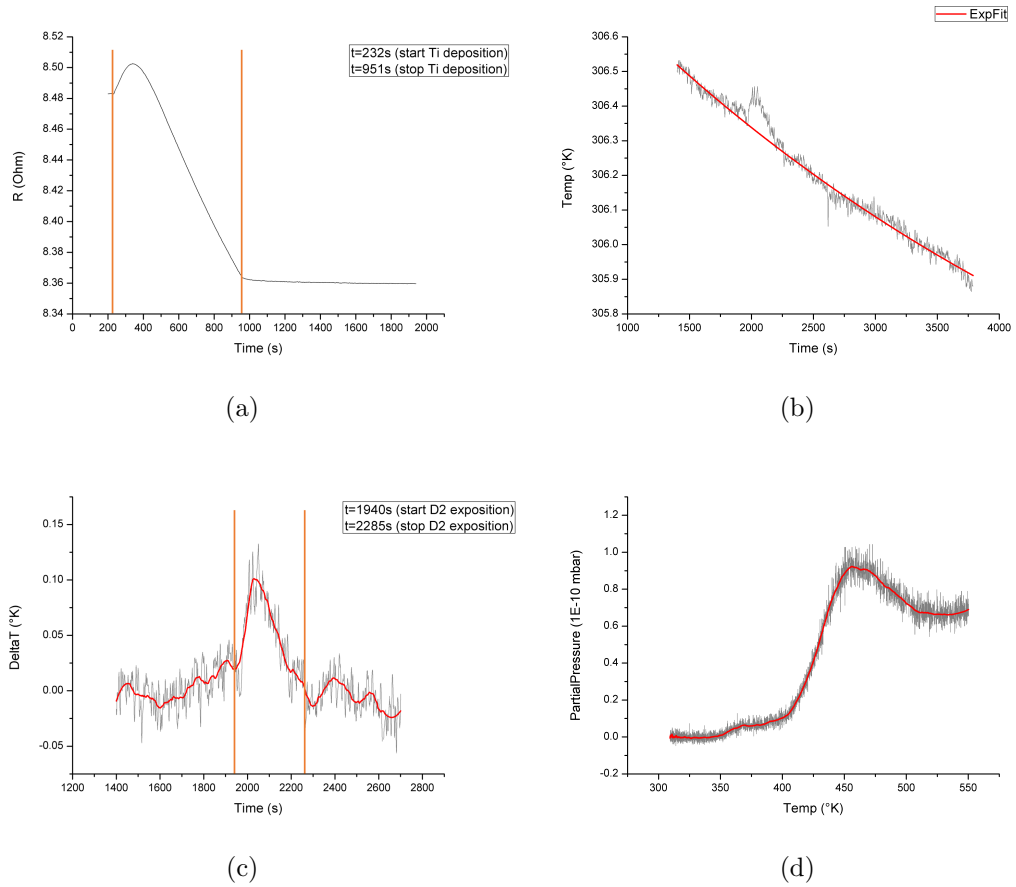

Figure 5.14: (a) Sensor resistance variation during the second Ti deposition (for 719 s, 16.5 ML of Ti) on SampleG2. (b) Sensor temperature variation, showing the increase due to the adsorption process (red line: exponential fit of the thermalization trend), in the second measurement performed with SampleG2. (c) Sensor temperature variation during D_2 exposure on the Ti layer. (Red line: smoothing) A $\Delta T \approx 0.10$ K is clearly detected. (d) TDS spectrum of SampleG2 after 5 min of D_2 exposure at $P_{D2} = 1.0 \cdot 10^{-7}$ mbarD_2. It shows a clear desorption peak at 459 K. (Red line: smoothing)

After that, we perform the TDS measurement. We place the sample in front of the RGA and we heat it from room temperature up to around 600 K, while recording the TDS spectrum (shown in Fig. 5.14(d)). A clear desorption peak is detected at $T_p = (459 \pm 5)$ K.

In order to confirm the previous calorimetric detection, we repeat the measurements with a new, clean sample, as described in the following section.

5.3.2 Sample G3

We mounted a new sample (**SampleG3**), and after the calibration and the degas, we recorded a TDS spectrum, in order to be sure of its clearness.

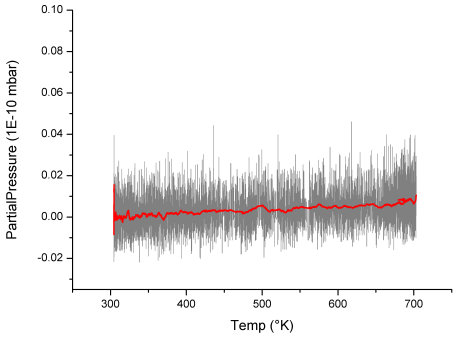

Figure 5.15: TDS spectrum after complete degas of SampleG3.

After the complete thermalization of the sample, we deposit Ti for 539 s (12.4 ML of Ti, as shown in Fig. 5.16(a)) and afterwards we wait 15 minutes for the thermalization of the sample. Then we expose the sample to D_2 for 5 minutes at a pressure of $1.0 \cdot 10^{-7}$ mbar, while recording the sensor resistance. After subtracting the thermalization trend, we obtain the sensor temperature variation, as shown in Fig. 5.16(c). An increase in the sensor temperature is clearly detected ($\Delta T \approx 0.065$ K).

After that, we perform the TDS measurement. We place the sample in front of the RGA and we heat it from room temperature up to around 600 K, while recording the TDS spectrum (shown in Fig. 5.16(d)). A clear desorption peak is detected at $T_p = (469 \pm 3)$ K.

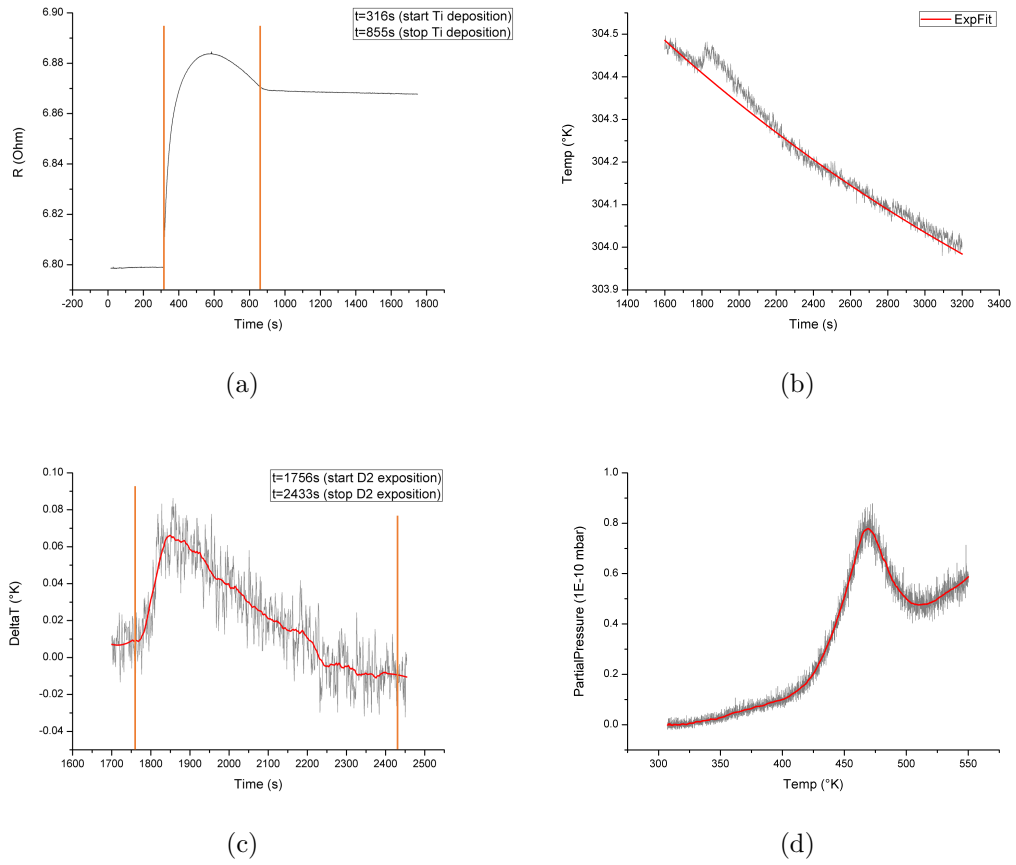

Figure 5.16: (a) Sensor resistance variation during the first Ti deposition (for 539 s, 12.4 ML of Ti) on SampleG3. (b) Sensor temperature variation, showing the increase due to the adsorption process (red line: exponential fit of the thermalization trend), in the second measurement performed with SampleG3. (c) Sensor temperature variation during D_2 exposure on the Ti layer. (Red line: smoothing) A $\Delta T \approx 0.065$ K is clearly detected. (d) TDS spectrum of SampleG3 after 5 min of D_2 exposure at $P_{D2} = 1.0 \cdot 10^{-7}$ mbarD_2. It shows a clear desorption peak at 469 K. (Red line: smoothing)

We repeat the same procedure a second time, with the same sample. We deposit again Ti for 723 s (a second layer of 16.6 ML of Ti, as shown in Fig. 5.17(a)) and afterwards we wait 20 minutes for the thermalization of the sample. Then we expose the sample to D_2 for 5 minutes at a pressure of $1.0 \cdot 10^{-7}$ mbar, while recording the sensor resistance. After subtracting the thermalization trend, we obtain the sensor temperature variation, as shown in Fig. 5.17(c). An increase in the sensor temperature is clearly detected ($\Delta T \approx 0.25$ K).

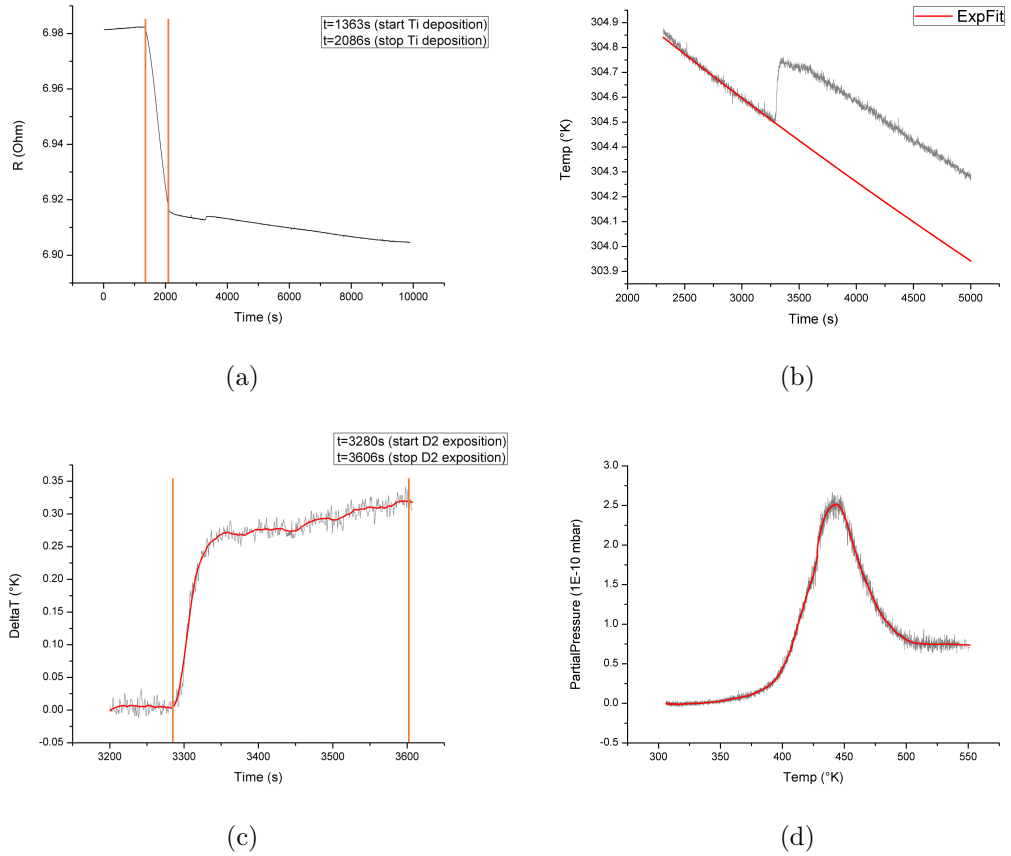

Figure 5.17: (a) Sensor resistance variation during the second Ti deposition (for 723 s, 16.6 ML of Ti) on SampleG3. (b) Sensor temperature variation, showing the increase due to the adsorption process (red line: exponential fit of the thermalization trend), in the second measurement performed with SampleG3. (c) Sensor temperature variation during D_2 exposure on the Ti layer. (Red line: smoothing) A $\Delta T \approx 0.25$ K is clearly detected. (d) TDS spectrum of SampleG3 after 5 min of D_2 exposure at $P_{D2} = 1.0 \cdot 10^{-7}$ mbarD_2. It shows a clear desorption peak at 442 K. (Red line: smoothing)

After that, we perform the TDS measurement. We place the sample in front of the RGA and we heat it from room temperature up to around 600 K, while

recording the TDS spectrum (shown in Fig. 5.17(d)). A clear desorption peak is detected at $T_p = (442 \pm 3)$ K.

5.3.3 Wheatstone bridge vs 4-probe

Looking at the calorimetric signals, in the range of $(0.045 - 0.25)$ K, it is clear that the Wheatstone bridge setup is necessary in order to decrease the noise, increase the sensitivity, and allow the detection of the temperature variation during the hydrogenation of Ti-decorated graphene. In fact, with the simple 4-wire setup, we can not avoid a noise level of around 0.05 K, and temperature fluctuations ~ 0.15 K caused by thermal instability of the measuring setup (see Fig. 5.18, dark blue line), or even higher. These values are superior than the signal we are trying to detect, therefore the noise would prevent any clear thermometric measurement.

Whereas, with the Wheatstone bridge setup (which includes low temperature coefficient resistances), the noise level is lowered to a value around 0.01 K (see Fig. 5.18, red line), with an improvement of a factor > 10. This reduction of the noise to a value minor than the calorimetric signal, finally has allowed us to clearly detect the temperature increase during deuterium adsorption, with a favorable signal-to-noise ratio, between 5 and 10.

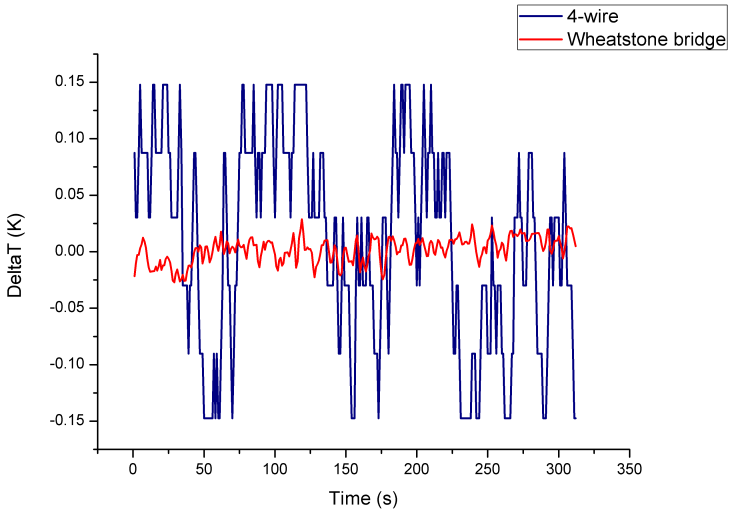

Figure 5.18: Comparison of the noise fluctuations with the 4-wire setup (dark blue line) and the Wheatstone bridge setup (red line).

Discussion and Conclusions

6

In the previous chapter the clear detection of the heat release during the deuterium adsorption process is demonstrated In this chapter we present the analysis performed in order to calculate, from the calorimetric measurements, the heat released in the process. Then, we compare the estimated energy with the one obtained through the TDS measurements, with the purpose of verifying the results of this new method. The TDS is also a complementary analysis, in fact it provides an estimation of the binding energy per molecule and the amount of deuterium stored in the system.

6.1 Calorimetric Analysis

As already seen in Chapter 2, we can describe our system with a simple thermal model. The temperature increase, in the order of tenths of K, is comparable with the estimation done in Chapter 2 for graphene + gold + titanium + silica. This confirms that we must take into account also the silica layer in the fast thermalization, and therefore include it in the sensor heat capacity calculation. In fact, during the exothermic adsorption process, the heat released initially warms the sensor, down to the silica layer, in a fast thermalization process. From the characteristic time of the cooling, we have calculated the heat transfer coefficient (see Chapter 4), which allow us to describe the heat transmission through the sensor with the eq. (2.6):

$$\frac{\delta H_r}{\delta t} = C_{sensor} \cdot \frac{\delta \Delta T(t)}{\delta t} + \lambda \cdot \Delta T(t) \tag{6.1}$$

The $\Delta T(t)$ has been recorded during the deuterium exposure, while the C_{sensor} has been calculated from the physical properties of the sample (see eq. (2.9)). Using the data analysis software OriginPro, we can perform a point-by-point derivative of the recorded data of $\Delta T(t)$, and obtain the first term. An example of the

$\delta\Delta T(t)/\delta t$ is shown in Fig. 6.1(b) (second measurement of SampleG3, shown in Fig. 5.17). The second one is the simple product of the thermometric signal and the heat transfer coefficient. Via point-by-point integration (with the OriginPro software), from eq. 6.1, we calculate the enthalpy release. An example of the $\delta H_r/\delta t$ is reported in Fig. 6.1(c) (second measurement of SampleG3), showing also the area integration which gives the value of H_r (light blue area).

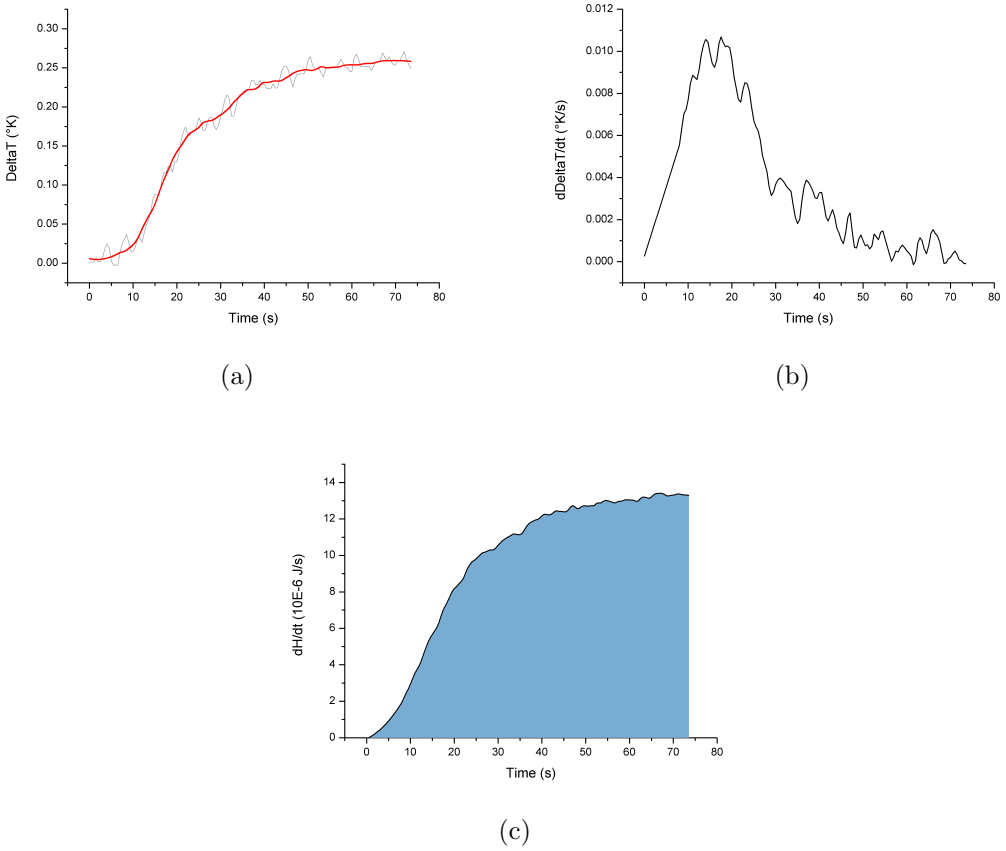

Figure 6.1: (a) Rising part of $\Delta T(t)$ at the beginning of D_2 exposure of SampleG2, second measurement. (Red line: smoothing) (b) $\delta\Delta T(t)/\delta t$ during the second measurement on SampleG2. (c) $\delta H_r/\delta t$ for the same measurement (the area integration is shown in light blue).

For the **SampleG2**, we have:

- $C_{sensor} = 14.99 \cdot 10^{-6}$ J/K [see eq. (2.15)]
- $\tau = (2.8 \pm 1.3)$ s [see Tab. 4.15]
- $\lambda_{G2} = C_{sensor}/\tau = (5.4 \pm 2.7) \cdot 10^{-6}$ W/K

From the first measurement, after the first deposition of 8.4 ML of Ti, we obtain for the adsorption process:

$$H_r(SampleG2_{(1)}) = (22 \pm 11)\ \mu\text{J} \tag{6.2}$$

While, from the second measurement, after the second deposition of 16.5 ML of Ti, we obtain:

$$H_r(SampleG2_{(2)}) = (34 \pm 17)\ \mu\text{J} \tag{6.3}$$

The significant error is the consequence of the important noise we had during the calibration of the SampleG2, made with the first Wheatstone bridge setup.

Using the same procedure for the **SampleG3**, we have:

- $C_{sensor} = 14.99 \cdot 10^{-6}$ J/K [see eq. (2.15)]
- $\tau = (2.94 \pm 0.63)$ s [see Tab. 4.16]
- $\lambda_{G3} = C_{sensor}/\tau = (5.1 \pm 1.1) \cdot 10^{-6}$ W/K

From the first measurement, after the first deposition of 12.4 ML of Ti, we obtain the heat release:

$$H_r(SampleG3_{(1)}) = (23.4 \pm 4.7)\ \mu\text{J} \tag{6.4}$$

While, from the second measurement, after the second deposition of 16.6 ML of Ti, we obtain:

$$H_r(SampleG3_{(2)}) = (58 \pm 12)\ \mu\text{J} \tag{6.5}$$

The error on the final values of SampleG3 is lower in comparison with the SampleG2 results. The reason is the lower noise during the calibration of SampleG3, made with the new Wheatstone bridge setup.

For both SampleG2 and SampleG3, the heat release is bigger in case of higher Ti deposited on the sample. This proportionality is most probably an effect of the bulk contribution for the deuterium uptake. In fact, even if we expect that the major contribution comes from the surface adsorption, because of the high amount of Ti (around twice the quantity necessary for 100% coverage) we must consider also the bulk absorption.

6.2 TDS Analysis

The Thermal Desorption Spectroscopy allows us to complete the analysis, obtaining both the average binding energy per D_2 molecule and the amount of deuterium stored in the system. At the same time, studying the TDS spectra, we can calculate the total heat release, as a control value for the energy obtained before.

6.2.1 Average Binding Energy

From the measured desorption temperature T_p we can estimate the desorption energy barrier E_d, that corresponds to the average binding energy per molecule E_b. First of all we extract the desorption temperature from the TDS spectra, as shown in Fig. 6.2.

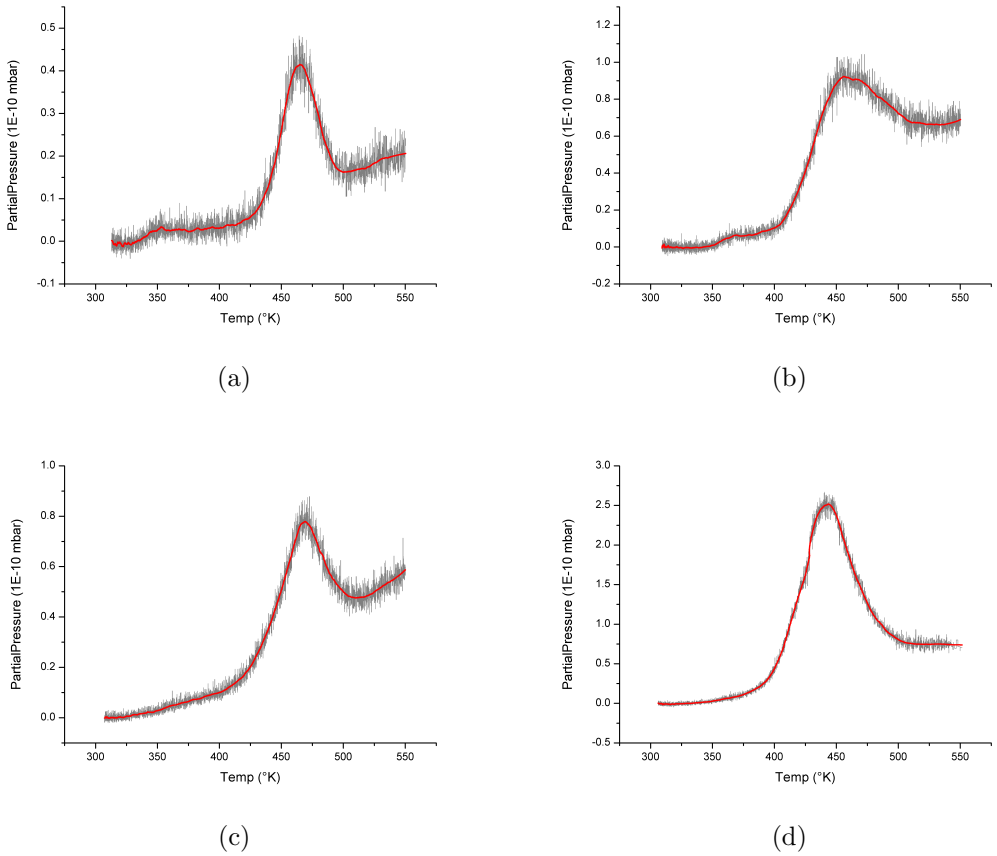

Figure 6.2: TDS spectra vs Temperature for: (a) SampleG2, first measurement, $T_p = 465\ K$; (b) SampleG2, second measurement, $T_p = 459\ K$; (c) SampleG3, first measurement, $T_p = 469\ K$; (d) SampleG23, second measurement, $T_p = 442\ K$. (Red line: smoothing)

Then, we calculate the time from the start of the desorption ramp to the moment at which the desorption peak T_p is reached, τ_m. Finally, using:

$$\frac{E_d}{K_B \cdot T_p} = A \cdot \tau_m \cdot \exp\left(-\frac{E_d}{K_B \cdot T_p}\right) \tag{6.6}$$

with $A = 10^{13}\ \mathrm{s}^{-1}$ and $K_B = 8.625 \cdot 10^{-5}\ \mathrm{eV} \cdot \mathrm{K}^{-1}$, we obtain the following desorption energy barriers:

Measurement	T_p (K)	τ_m (s)	$E_d/molecule$ (eV)
$SampleG2_{(1)}$	(465 ± 3)	(328 ± 1)	(1.29 ± 0.02)
$SampleG2_{(2)}$	(459 ± 5)	(569 ± 1)	(1.30 ± 0.06)
$SampleG3_{(1)}$	(469 ± 3)	(442 ± 1)	(1.32 ± 0.07)
$SampleG3_{(2)}$	(442 ± 3)	(412 ± 1)	(1.24 ± 0.09)

Table 6.1: Temperature of the desorption peak T_p, heating time τ_m, and average binding energy $E_d/molecule$, calculated from TDS measurements.

These energies, which correspond to the average binding energies for the adsorption of deuterium molecules on Ti atoms, are comparable with the ones obtained in previous experimental investigations on similar systems, in the range of $(1 - 1.5)$ eV [26, 33].

A slightly lower desorption temperature in the second measurements is expected. In fact, because of the higher volume of titanium deposited on the sample, the number of available bonds for binding deuterium is higher than in the first measurements. This leads to a lower average binding energy, and therefore to a lower temperature for the desorption peak.

6.2.2 Hydrogen uptake calculated from TDS

The amount of desorbed (and therefore previously stored) deuterium can be estimated from the TDS spectra in Fig. 6.3, showing the partial pressure of D_2 in function of the time.

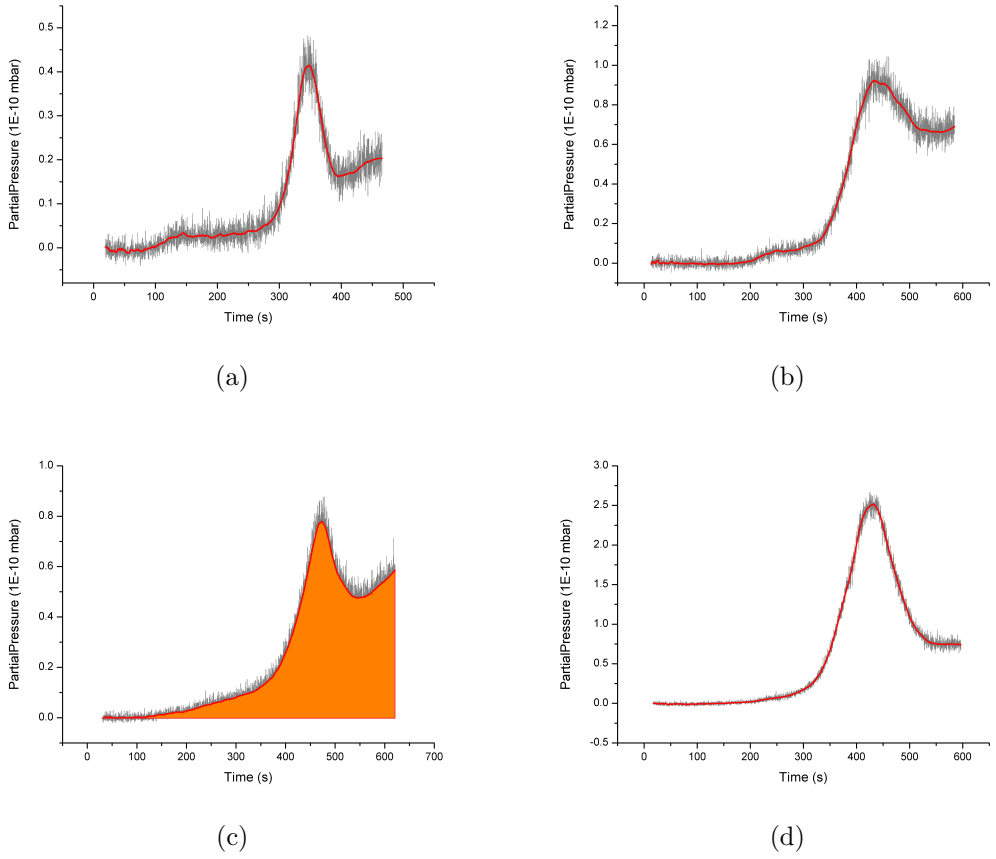

Figure 6.3: TDS spectra vs Time for SampleG2: first (a) and second (b) measurement. TDS spectra vs Time for SampleG3: first (c) and second (d) measurement.

At a given pressure, the amount of desorbed gas is equal to the pumping speed of the vacuum system. This parameter depends on the gas and on the base pressure. In our case we extract the effective pumping speed for hydrogen from the datasheet of our Diode Ion Pump (Fig. 6.4). With a D_2 base partial pressure in the range of $(0.2 - 0.6) \cdot 10^{-10}$ mbar, we have an effective pumping speed (S) varying from 90% to 110% of the nominal speed, which is 300 L/s. Therefore we use an average pumping speed of 300 L/s.

After the subtraction of the background, we perform an integration of the TDS

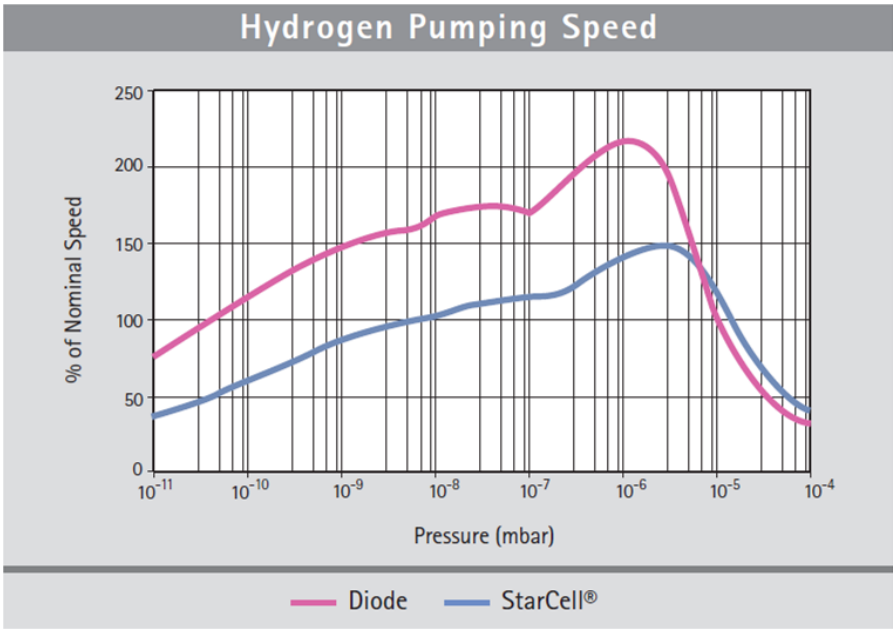

Figure 6.4: Effective pumping speed for hydrogen (Diode Ion Pump). Base pressure $\sim 2 \cdot 10^{-11}$ mbar.

spectra, obtaining the areas under the curves, F. Then, we can use eq. (2.26):

$$pV = FS = nRT \tag{6.7}$$

with $R = 8.314\ \mathrm{J \cdot K^{-1} \cdot mol^{-1}}$, the gas constant, in order to calculate n, the amount of desorbed D_2. In this equation we must use the room temperature ($T_{amb} \sim 300$ K), not the sample temperature (T_{sample} varies from 300 K to 700 K). That because the calibration of the RGA has been performed using as reference the total pressure of the chamber, read by the pressure gauge of the UHV chamber, which is thermalized at T_{amb}. The results are shown in Table 6.2.

Measurement	**F** (mbar s)	D_2 (mol)	D_2 (molecules)
$SampleG2_{(1)}$	$(44.4 \pm 0.5) \cdot 10^{-10}$	$5.43 \cdot 10^{-11}$	$3.27 \cdot 10^{13}$
$SampleG2_{(2)}$	$(174 \pm 2) \cdot 10^{-10}$	$2.12 \cdot 10^{-10}$	$1.27 \cdot 10^{14}$
$SampleG3_{(1)}$	$(140 \pm 1) \cdot 10^{-10}$	$1.71 \cdot 10^{-10}$	$1.03 \cdot 10^{14}$
$SampleG3_{(2)}$	$(367 \pm 3) \cdot 10^{-10}$	$4.50 \cdot 10^{-10}$	$2.71 \cdot 10^{14}$

Table 6.2: Amount of desorbed deuterium, in mol and number of molecules (1 mol = $6.022 \cdot 10^{23}$ molecules).

This quantities can be used to evaluate the gravimetric density (GD) of the system, defined as:

$$GD = \frac{M_H}{M_{Ti} + M_{Graphene} + M_H} \tag{6.8}$$

The mass of Ti can be calculated from the number of ML of Titanium deposited on the sensor, knowing that 1 ML on our sample area (22.48 mm^2) corresponds to $3.03 \cdot 10^{14}$ atoms, corresponding to a weight of $2.38 \cdot 10^{-11}$ kg. Graphene has a mass density of $7.6 \cdot 10^{-10}$ g/mm^2 (from [61]), whereas the mass of loaded hydrogen can be obtained knowing that $1.0 \cdot 10^{14}$ H_2 molecules have a mass of $3.24 \cdot 10^{-10}$ g.

Because an actual hydrogen storage system would not use a thick substrate as the one we have in our experiment, and moreover we can reduce the amount of Ti to a layer of the order of the ML (introducing defects for example, as seen in ref. [31]), we present an estimation of the GD of this ideal system. We consider only graphene + Ti (1 ML) + molecular hydrogen (instead of molecular deuterium), in the same uptake conditions of our experiment.

For SampleG2, in the first measurement, we have:

- $M_{Ti} = d\ A\ \rho_V = 0.2342 \cdot 10^{-7} \cdot 22.48 \cdot 10^{-2} \cdot 4.507 = 2.37 \cdot 10^{-8}$ g
- $M_{graph} = A\ \rho_A = 22.48 \cdot 7.6 \cdot 10^{-10} = 1.71 \cdot 10^{-8}$ g
- $M_{H_2} = n_{H_2}\ m_{H_2} = 1.06 \cdot 10^{-10}$ g

where d is the thickness of 1 ML of Ti, A is the graphene area covered by Ti, ρ_V is the volume density of Ti, ρ_A is the surface density of monolayer graphene, n_{H_2} is the number of H_2 molecules adsorbed and m_{H_2} the mass of a single molecule. Therefore, from eq. (6.8) we obtain:

$$GD = \frac{1.06 \cdot 10^{-10}}{2.37 \cdot 10^{-8} + 1.71 \cdot 10^{-8} + 1.06 \cdot 10^{-10}} = 0.26\ \text{wt.\%} \tag{6.9}$$

In similar way we calculate the GD for both SampleG2 and SampleG3. The resulting GD are listed in Table 6.3.

Measurement	**GD** (wt.%)
$SampleG2_{(1)}$	0.26
$SampleG2_{(2)}$	1.0
$SampleG3_{(1)}$	0.81
$SampleG3_{(2)}$	2.1

Table 6.3: GD of an ideal hydrogen storage system composed by graphene monolayer + 1 ML of Ti.

6.2.3 Heat release from TDS

Finally, we can estimate the heat release during the adsorption of molecular deuterium on Ti, as a control analysis. We simply multiply the average binding energy per molecule and the number of deuterium molecules desorbed. The results obtained for SampleG2 and SampleG3, both with calorimetric and TDS methods, are listed in Table 6.4.

Measurement	H_r **from calorimetry** (μJ)	H_r **from TDS** (μJ)
$SampleG2_{(1)}$	22 ± 11	6.75 ± 0.16
$SampleG2_{(2)}$	34 ± 17	26.4 ± 1.4
$SampleG3_{(1)}$	23.4 ± 4.7	21.8 ± 1.3
$SampleG3_{(2)}$	58 ± 12	53.8 ± 4.3

Table 6.4: Comparison between the heat release calculated via the calorimetric technique and the TDS analysis.

The heat release calculated through the TDS analysis is comparable to the values obtained with the calorimetric analysis. For SampleG3 the results are very similar, they actually correspond within the error range. In both cases, in the second measurement a major deuterium adsorption has been detected. This is a consequence of the higher amount of total titanium which had been deposited on the sensor. Therefore, a higher volume of Ti corresponds to a higher amount of stored deuterium.

In fact, because of the high amount of Ti deposited on graphene, the process is the combination of a surface adsorption, and a bulk absorption. Even if, in

perspective for an actual device, we are interested only in the contribution of surface adsorption, the only possibility for separate the two contributions is a calibration of the hydrogen uptake in function of Ti deposited, starting with low quantities of Ti, of the order of fractions of ML.

Knowing the heat release, we can calculate the energy efficiency of our hydrogen storage system, which can be estimated from the ratio between the energy (E_a) necessary for the desorption of hydrogen and the energy released (E_r) in its use as fuel:

$$\eta = 1 - \frac{E_a}{E_r} \tag{6.10}$$

In our case E_a is the energy needed for heating the sample up to the desorption temperature. From the well known reaction [62]:

$$2H_2 + O_2 \rightarrow 2H_2O + 572 \text{ kJ } (286 \text{ kJ/mol}) \tag{6.11}$$

we can calculate the energy released from the combustion of the quantity of hydrogen desorbed from the samples. While knowing the temperature increase (from room temperature to 550 K) for the hydrogen desorption, and the heat capacity of the sensor, we can estimate the energy needed for reaching the desorption temperature (we present a perspective situation in which we have only graphene + Ti (1 ML)). In Table 6.5 are listed the energies and the efficiencies for the four measurements, with SampleG2 and SampleG3.

Measurement	E_a (J)	E_r (J)	**Energy efficiency (η)**
$SampleG2_{(1)}$	$6.0 \cdot 10^{-6}$	$1.56 \cdot 10^{-5}$	61%
$SampleG2_{(2)}$	$6.1 \cdot 10^{-6}$	$6.07 \cdot 10^{-5}$	90%
$SampleG3_{(1)}$	$6.2 \cdot 10^{-6}$	$4.89 \cdot 10^{-5}$	87%
$SampleG3_{(2)}$	$6.2 \cdot 10^{-6}$	$1.27 \cdot 10^{-4}$	95%

Table 6.5: Energy necessary for the desorption of the stored hydrogen (E_a) and energy released from the use of hydrogen as fuel (E_r). Also the energy efficiencies η are listed.

In perspective, an actual similar hydrogen storage system would be done with a multilayer graphene without the thick Si substrate of our experiments, and where only a little part (of the bottom layer for example) of the graphene is laid down on a thermometer similar to our gold layer. This would allow the temperature measurement during the hydrogen adsorption, whereas it would not affect the heat capacity of the major part of the system. For that reason, for a future multilayer graphene device we can expect an energy efficiency up to 95%.

6.3 Conclusions and Outlook

The first important result of this thesis work is the implementation of an experimental setup which is able to directly detect the small heat release during the adsorption process. The final setup, with the Wheatstone bridge, low temperature coefficient resistances, and the high quality Pre-Amplifier allows to measure a temperature increase in the order of ~ 0.01 K.

Beside that, the good agreement between the values of the heat release calculated through our new calorimetric method and the TDS method, is the major result of this research work. Because of its non-destructive and direct characteristics, this method introduce a valuable, and reliable, measurement of the amount of hydrogen stored in the system.

Furthermore, the simple procedures for the sample preparation and its calibration, make this sensor suitable for the use in similar experiments. For example, graphene decoration with different metals can be investigated (e.g. lithium or calcium), or the sample can be exposed to atomic hydrogen, with the purpose of further studies on hydrogen storage.

Moreover, a simulation of the heat transfer through the sample could be performed using a simulation software (as *COMSOL*), in order to better understand the thermal exchange processes between the sensor's layers. This analysis would be useful for designing an optimized thermometer in order to improve the sensitivity. Also a further calibration with increasing coverages, starting from fractions of ML and therefore from coverages lower than 100%, will be useful in order to distinguish the bulk absorption contribution from the surface adsorption one. Furthermore, it will be interesting to substitute the thick silicon substrate with a different, thinner one. Suitable materials could be the SiN membranes, which have lower heat capacity and then would decrease the heat losses of the thermometer towards the substrate, allowing a better signal-to-noise ratio.

In addition, for improving the gravimetric density of the storage system, further experiments can be performed, in order to reduce the amount of Ti deposited on graphene. This would be possible by creating defects on the graphene surface (by doping with heteroatoms or by damaging the surface and therefore creating vacancies), which act as favorable pinning sites for Ti atoms, decreasing the dimensions of the Ti clusters, and therefore decreasing the volume of Ti necessary in order to obtain 100% coverage. Also the use of amorphous and curved graphene can be exploited, with the same purpose. These modifications of the graphene layer would prevent the Ti clustering, decreasing the amount of titanium required for achieving a surface coverage of 100%. Thus, the gravimetric density of the

storage system would increase.

Finally, a similar thermometer can be used in order to investigate the functionalization of graphene with organic molecules. This functionalization process would allow us to move from 2-dimensional model structures to practical 3-dimensional systems. The principal interest in the preparation and characterization of nanocomposite functionalized graphene system is aimed to achieving new sensors for selective interactions with target molecules, efficient and metal-free nano-catalyst materials, and graphene/molecule/graphene heterostructures towards spaced multilayer stacking and three dimensional graphene materials. The opportunity of performing calorimetric measurements on similar samples would be very valuable, in order to better understand and describe the reactions which take place between organic molecules and graphene sheets.

In conclusion, the principal purpose of this work was to present a new method for calorimetric detection in functionalized graphene systems, and its first implementation in actual experiments. The experimental results demonstrated the feasibility of this procedure, together with the reliability of the detection method. Further investigations and improvements are currently under study, in order to develop both enhanced sensors, similar to the one presented in this thesis, and improved samples for hydrogen storage.

Bibliography

[1] B.L. Cohen. *The nuclear energy option: an alternative for the 90s*. Plenum Press, 1990.

[2] US Department of Energy. Research and development goals. *http://energy.gov/eere/fuelcells/hydrogen-storage*, 2016.

[3] A. Züttel, P. Sudan, Ph. Mauron, T. Kiyobayashi, Ch. Emmenegger, and L. Schlapbach. Hydrogen storage in carbon nanostructures. *International Journal of Hydrogen Energy*, 27(2):203–212, 2002.

[4] R.S. Irani. Hydrogen Storage: High–Pressure Gas Containment. *MRS Bulletin*, 27(9):680–682, 2002.

[5] P. Silvestroni. *Fondamenti di chimica*. 1996.

[6] S.A. Sherif, N. Zeytinoglu, and T.N. Veziroğlu. Liquid hydrogen: Potential, problems, and a proposed research program. *International Journal of Hydrogen Energy*, 22(7):683 –688, 1997.

[7] G. Principi, F. Agresti, A. Maddalena, and S. Lo Russo. The problem of solid state hydrogen storage. *Energy*, 34(12):2087–2091, 2009.

[8] Valentina Tozzini and Vittorio Pellegrini. Prospects for hydrogen storage in graphene. *Physical Chemistry Chemical Physics*, 15(1):80–89, 2013.

[9] Changgu Lee, Xiaoding Wei, Jeffrey W. Kysar, and James Hone. Measurement of the elastic properties and intrinsic strength of monolayer graphene. *Science*, 321(5887):385–388, 2008.

[10] Wataru Norimatsu and Michiko Kusunoki. Epitaxial graphene on SiC {0001}: advances and perspectives. *Physical Chemistry Chemical Physics*, 16(8):3501–3511, 2014.

[11] Adriano Ambrosi, Chun Kiang Chua, Alessandra Bonanni, and Martin Pumera. Electrochemistry of Graphene and Related Materials. *Chemical Reviews*, 114(14):7150–7188, 2014.

[12] Valentina Tozzini and Vittorio Pellegrini. Reversible hydrogen storage by controlled buckling of graphene layers. *The Journal of Physical Chemistry C*, 115(51):25523–25528, 2011.

[13] Serguei Patchkovskii, S. Tse John, Sergei N. Yurchenko, Lyuben Zhechkov, Thomas Heine, and Gotthard Seifert. Graphene nanostructures as tunable storage media for molecular hydrogen. *Proceedings of the National Academy of Sciences of the United States of America*, 102(30):10439–10444, 2005.

[14] Y. Miura, H. Kasai, W. Dino, H. Nakanishi, and T. Sugimoto. First principles studies for the dissociative adsorption of H_2 on graphene. *Journal of applied physics*, 93:3395–3400, 2003.

[15] Sarah Goler, Camilla Coletti, Valentina Tozzini, Vincenzo Piazza, Torge Mashoff, Fabio Beltram, Vittorio Pellegrini, and Stefan Heun. Influence of graphene curvature on hydrogen adsorption: toward hydrogen storage devices. *The Journal of Physical Chemistry C*, 117(22):11506–11513, 2013.

[16] Simone Casolo, Ole Martin Lvvik, Rocco Martinazzo, and Gian Franco Tantardini. Understanding adsorption of hydrogen atoms on graphene. *The Journal of Chemical Physics*, 130(5):054704, 2009.

[17] Dragan Stojkovic, Peihong Zhang, Paul E. Lammert, and Vincent H. Crespi. Collective stabilization of hydrogen chemisorption on graphenic surfaces. *Physical Review B*, 68(19):195406, 2003.

[18] Yves Ferro, D. Teillet-Billy, N. Rougeau, V. Sidis, S. Morisset, and Alain Allouche. Stability and magnetism of hydrogen dimers on graphene. *Physical Review B*, 78(8):085417, 2008.

[19] Daniel C. Elias, Rahul Raveendran Nair, T.M.G. Mohiuddin, S.V. Morozov, P. Blake, M.P. Halsall, A.C. Ferrari, D.W. Boukhvalov, M.I. Katsnelson, A.K. Geim, et al. Control of graphene's properties by reversible hydrogenation: evidence for graphane. *Science*, 323(5914):610–613, 2009.

[20] Jacob W. Burress, Srinivas Gadipelli, Jamie Ford, Jason M. Simmons, Wei Zhou, and Taner Yildirim. Graphene oxide framework materials: theoretical predictions and experimental results. *Angewandte Chemie International Edition*, 49(47):8902–8904, 2010.

[21] Barbara Panella, Michael Hirscher, and Siegmar Roth. Hydrogen adsorption in different carbon nanostructures. *Carbon*, 43(10):2209–2214, 2005.

[22] G. Srinivas, Yanwu Zhu, Richard Piner, Neal Skipper, Mark Ellerby, and Rod Ruoff. Synthesis of graphene–like nanosheets and their hydrogen adsorption capacity. *Carbon*, 48(3):630–635, 2010.

[23] C. Ataca, E. Aktrk, S. Ciraci, and H. Ustunel. High–capacity hydrogen storage by metallized graphene. *Applied Physics Letters*, 93(4):043123, 2008.

[24] Gregory J. Kubas. Hydrogen activation on organometallic complexes and H_2 production, utilization, and storage for future energy. *Journal of Organometallic Chemistry*, 694(17):2648–2653, 2009.

[25] Vinayan Bhagavathi Parambhath, Rupali Nagar, K. Sethupathi, and S. Ramaprabhu. Investigation of spillover mechanism in palladium decorated hydrogen exfoliated functionalized graphene. *The Journal of Physical Chemistry C*, 115(31):15679–15685, 2011.

[26] Torge Mashoff, Makoto Takamura, Shinichi Tanabe, Hiroki Hibino, Fabio Beltram, and Stefan Heun. Hydrogen storage with titanium–functionalized graphene. *Applied Physics Letters*, 103(1):013903, 2013.

[27] Elham Beheshti, Alireza Nojeh, and Peyman Servati. A first–principles study of calcium–decorated, boron-doped graphene for high capacity hydrogen storage. *Carbon*, 49(5):1561–1567, 2011.

[28] Kevin T. Chan, J. B. Neaton, and Marvin L. Cohen. First–principles study of metal adatom adsorption on graphene. *Phys. Rev. B*, 77:235430, 2008.

[29] Engin Durgun, S. Ciraci, and Tanner Yildirim. Functionalization of carbon–based nanostructures with light transition–metal atoms for hydrogen storage. *Physical Review B*, 77(8):085405, 2008.

[30] Yali Liu, Ling Ren, Yao He, and Hai-Ping Cheng. Titanium–decorated graphene for high–capacity hydrogen storage studied by density functional simulations. *Journal of Physics: Condensed Matter*, 22(44):445301, 2010.

[31] T. Mashoff, D. Convertino, V. Miseikis, C. Coletti, V. Piazza, V. Tozzini, F. Beltram, and S. Heun. Increasing the active surface of titanium islands on graphene by nitrogen sputtering. *Applied Physics Letters*, 106(8):083901, 2015.

[32] F. Banhart, J. Kotakoski, and A. V. Krasheninnikov. Structural Defects in Graphene. *ACS Nano*, 5(1):26–41, 2011.

[33] Keisuke Takahashi, Shigehito Isobe, Kengo Omori, Torge Mashoff, Domenica Convertino, Vaidotas Miseikis, Camilla Coletti, Valentina Tozzini, and Stefan Heun. Revealing the Multi–Bonding State Between Hydrogen and Graphene–Supported Ti Clusters. *The Journal of Physical Chemistry C*, 120(24):12974–12979, 2016.

[34] Peter W. Atkins. *Physical Chemistry (4th ed.)*. Wiley, 2006.

[35] T. Hofelich, L. Wadsö, A. L. Smith, H. Shirazi, and S. R. Mulligan. The isothermal heat conduction calorimeter: a versatile instrument for studying processes in physics, chemistry, and biology. *J. Chem. Educ*, 78(8):1080, 2001.

[36] Peter G. Laye, S. B. Warrington, Thermal Methods Group, G. Roger Heal, Duncan M. Price, and Richard Wilson. *Principles of Thermal Analysis and Calorimetry*. The Royal Society of Chemistry, 2002.

[37] Micheal E. Brown. *Handbook of Thermal Analysis and Calorimetry (volume 1)*. Elsevier, 2003.

[38] Christoph Schick. Calorimetry. *Reference Module in Materials Science and Materials Engineering*.

[39] David Choi, Nirakar Poudel, Stephen B. Cronin, and Li Shi. Effects of basal–plane thermal conductivity and interface thermal conductance on the hot spot temperature in graphene electronic devices. *Applied Physics Letters*, 110(7):073104, 2017.

[40] Raymond Serway and John Jewett. *Principles of physics: a calculus–based text*. Nelson Education, 2012.

[41] Ji Won Suk, Karen Kirk, Yufeng Hao, Neal A. Hall, and Rodney S. Ruoff. Thermoacoustic sound generation from monolayer graphene for transparent and flexible sound sources. *Advanced Materials*, 24(47):6342–6347, 2012.

[42] David R. Lide. *CRC Handbook of Chemistry and Physics (84th Edition)*. CRC Press, 2007.

[43] A. Barbini, D. Bertolini, M. Cassettari, F. Papucci, A. Salvetti, G. Salvetti, and S. Veronesi. Differential microcalorimeter for liquid samples. *Review of scientific instruments*, 60(7):1308–1311, 1989.

[44] D. Bertolini, M. Cassettari, G. Salvetti, E. Tombari, and S. Veronesi. A differential calorimetric technique for heat capacity and thermal conductivity measurements of liquids. *Review of Scientific Instruments*, 61(9):2416–2419, 1990.

[45] M. Cassettari, F. Papucci, G. Salvetti, E. Tombari, S. Veronesi, and G.P. Johari. Simultaneous measurements of enthalpy and heat capacity of a thermosetting polymer during the curing process. *Review of scientific instruments*, 64(4):1076–1080, 1993.

[46] Gabor A. Somorjai and Yimin Li. *Introduction to Surface Chemistry and Catalysis (2nd Edition)*. Wiley, 2010.

[47] Richard I. Masel. *Principles of adsorption and reaction on solid surfaces*. Wiley, 1996.

[48] A.M. De Jong and J.W. Niemantsverdriet. Thermal desorption analysis: Comparative test of ten commonly applied procedures. *Surface Science*, 233(3):355–365, 1990.

[49] E.A. Denisov and T.N. Kompaniets. Kinetics of hydrogen release from graphite after hydrogen atom sorption. *Physica Scripta*, 2001(T94):128, 2001.

[50] P.A. Redhead. Thermal desorption of gases. *Vacuum*, 12(4):203–211, 1962.

[51] Kenjiro Oura, V.G. Lifshits, Alexander Saranin, A.V. Zotov, and M. Katayama. *Surface science: an introduction*. Springer Science & Business Media, 2013.

[52] L.M. Malard, M.A. Pimenta, G. Dresselhaus, and M.S. Dresselhaus. Raman spectroscopy in graphene. *Physics Reports*, 473(56):51–87, 2009.

[53] Andrea C. Ferrari, J.C. Meyer, V. Scardaci, C. Casiraghi, Michele Lazzeri, Francesco Mauri, S. Piscanec, Da. Jiang, K.S. Novoselov, S. Roth, et al. Raman spectrum of graphene and graphene layers. *Physical review letters*, 97(18):187401, 2006.

[54] V. Miseikis, D. Convertino, N. Mishra, M. Gemmi, T. Mashoff, S. Heun, N. Haghighian, F. Bisio, M. Canepa, V. Piazza, and C. Coletti. Rapid CVD growth of millimetre–sized single crystal graphene using a cold–wall reactor. *2D Materials*, 2(1):014006, 2015.

[55] Julian C. Chen. *Introduction to Scanning Tunneling Microscopy*. Oxford University Press, 1993.

[56] J. Bardeen. Tunnelling from a Many–Particle Point of View. *Phys. Rev. Lett.*, 6:57–59, 1961.

[57] A.N. Obraztsov, E.A. Obraztsova, A.V. Tyurnina, and A.A. Zolotukhin. Chemical vapor deposition of thin graphite films of nanometer thickness. *Carbon*, 45(10):2017–2021, 2007.

[58] Ke Xu, Peigen Cao, and James R. Heath. Scanning Tunneling Microscopy Characterization of the Electrical Properties of Wrinkles in Exfoliated Graphene Monolayers. *Nano Letters*, 9(12):4446–4451, 2009.

[59] Yanfeng Zhang, Teng Gao, Yabo Gao, Shubao Xie, Qingqing Ji, Kai Yan, Hailin Peng, and Zhongfan Liu. Defect-like Structures of Graphene on Copper Foils for Strain Relief Investigated by High–Resolution Scanning Tunneling Microscopy. *ACS Nano*, 5(5):4014–4022, 2011.

[60] Hans Lüth. *Surfaces and Interfaces of Ssolid Materials*. Springer–Verlag Berlin Heidelberg, 1995.

[61] Jian-Hao Chen, Chaun Jang, Shudong Xiao, Masa Ishigami, and Michael S. Fuhrer. Intrinsic and extrinsic performance limits of graphene devices on SiO_2. *Nature nanotechnology*, 3(4):206–209, 2008.

[62] Alternatives, Strategies for Future Hydrogen Production, and National Academy of Engineering Use, National Research Council. *The Hydrogen Economy: Opportunities, Costs, Barriers, and R&D N]eeds*. National Academies Press, 2004.